Steady and metastable cavitation in a converging-diverging nozzle

by

Benjamin Gallman

B.S., Colorado School of Mines, 2016

A THESIS

submitted in partial fulfillment of the requirements for the degree

MASTER OF SCIENCE

Department of Mechanical and Nuclear Engineering
College of Engineering

KANSAS STATE UNIVERSITY
Manhattan, Kansas

2019

Approved by:

Co-Major Professor
Dr. M. H. Hosni

Approved by:

Co-Major Professor
Dr. B. Terry Beck

Copyright

Abstract

While cavitation is usually avoided, it has useful engineering applications. Specifically, it can be used as to create cooling potential in a novel non-vapor compression refrigeration process. Cavitation occurs when the pressure of the working fluid (compressed liquid) drops below the saturation pressure. Since the cavitation (flash) results in an abrupt reduction in temperature, the working fluid can take in energy as heat from the surroundings during cavitation, which results in a cooling potential (refrigeration). In a converging-diverging nozzle, as the fluid passes through the throat the pressure decreases. If the pressure drops below the saturation pressure cavitation can occur. The current research focuses on measuring the pressure at the cavitation front, and the associated pressure distribution within the two-phase region in a converging diverging nozzle. A blow-down flow system was used to conduct measurements with water as the working fluid. The flow rate was measured with a rotameter and a Coriolis flow meter. The nozzle is a transparent 3D printed nozzle with an inlet diameter of 9.3 mm, throat diameter of 1.71 mm, and an outlet diameter of 9.3 mm. The upstream reservoir was kept at atmospheric pressure and was elevated above the level of the nozzle inlet. The downstream reservoir was evacuated to create a pressure difference that would drive fluid through the nozzle. The pressure distribution within the nozzle was measured with eight pressure transducers connected to the nozzle with 0.006” taps, and a high-speed camera was used to capture flow visualization. The pressure distribution was measured for steady cavitating flow at several back pressures, and during an increasing flow rate to capture pressure changes during cavitation initiation. These results give direct pressure measurements during cavitating flow, along with the accompanying flow visualization. They should prove useful for furthering understanding of the

metastable fluid mechanics behavior of cavitating flows, and thereby contribute to the ability to maximize the cooling potential of the cavitation phenomena.

Table of Contents

List of Figures

List of Tables

Acknowledgements

I would like to thank Dr. Beck who guided me in the technical aspects of this thesis and for his constant support. Also, thank you to Dr. Hosni for encouragement, guidance, and support when I needed it. I would also like to thank Eric Wagner in the MNE shop for helping me to construct and fabricate the various nozzles used in this thesis work. I would like to acknowledge Zayed Ahmed for teaching me how to use the high-speed camera equipment. Lastly, I would like to thank Mackenzie Penny for her constant support through the whole process.

Chapter 1 - Introduction

Cavitation is the phase change process where a fluid changes from liquid to vapor due to a decrease in pressure. The phase change occurs when the absolute pressure of the fluid drops below the saturation pressure, which is a function of fluid temperature. This process can occur at constant temperature with a decrease in absolute pressure, unlike boiling which involves the increase of temperature to elicit vaporization at a constant pressure. A comparison of the two types of vaporization can be seen in figure 1.1 where A_2 to A is boiling and A_1 to A is cavitation.

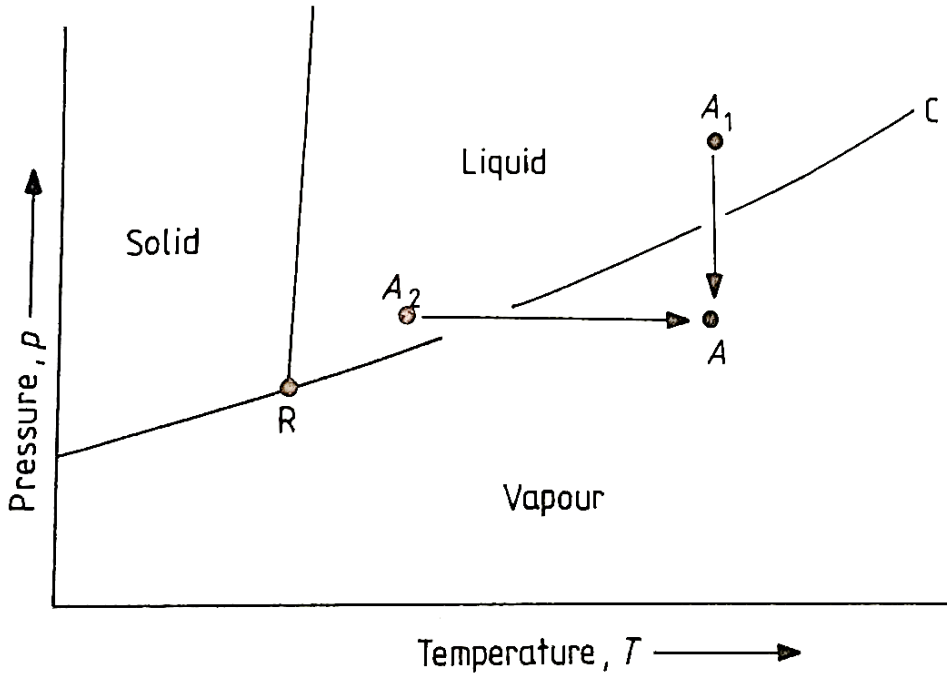

Figure 1.1: Phase diagram of a substance

Cavitation is normally a phenomenon to be avoided in engineering applications. In the marine industry, cavitation can occur around propellers limiting performance and often causing damage. When the local pressure along a propeller blade drops below the saturation pressure bubbles form due to cavitation. When the bubbles collapse they release energy and the propeller can be damaged in a process called pitting. In expansion and control valves the occurrence of

cavitation results in choked flow and limits the flow rates through the valves and thus the corresponding flow systems.

However, there are applications that can take advantage of cavitation. One such application is to use the energy intensive process of cavitation in a refrigeration system to absorb energy from the cooled space. Previous research done at Kansas State University by Alkatomi (2014, 2015) showed the possibility of altering the traditional refrigeration system to utilize the cooling potential of cavitation. In a traditional refrigeration system, the working fluid is compressed into a high-temperature and high-pressure state before passing into a condenser. In the condenser heat is passed into the surroundings, which are at a lower temperature. The working fluid then passes through an expansion valve to decrease the pressure and temperature. Next, in the evaporator the working fluid takes in heat from the refrigerated space to return to a higher temperature. Finally, the fluid passes into the compressor to repeat the cycle. This type of cycle uses refrigerants that often have a significant ozone level depletion potential (ODP) and global warming potential (GWP). The new application replaces the evaporator with a converging-diverging nozzle, which will create cavitation in the flow and take heat in from the surroundings. Since, the fluid will condense after the nozzle a compressor is not needed to pump the fluid through the system and can be replaced by a reciprocation piston or traditional pump. Thus, the new technology is referred to as a non-vapor compression refrigeration cycle.

Though water has shown little to no cooling potential within the new non-vapor compression cycle, it is still a useful fluid to study cavitation in a converging-diverging nozzle. The work presented in this thesis will build on work done by Ahmed (2017) to further analyze the cavitation phenomenon. The objective is to understand how the pressure in the nozzle relates

to cavitation initiation and the length of the two-phase region in the nozzle. This understanding will be useful in nozzle optimization to improve the cooling efficiency of the new technology.

Literature Review

The vapor compression refrigeration cycle is the most commonly used method of refrigeration because it is scalable, reliable, uses electricity and nontoxic and nonflammable refrigerants, and has a compact size (Goeztler et. Al, 2014). A schematic of this cycle is shown in figure 1.2. At state 7, a two-phase liquid vapor mixture enters the evaporator where heat is transferred from the cool space to the mixture causing state 8 to be a low-pressure vapor. This low-pressure vapor enters the compressor to become a high-pressure vapor with a high temperature. In the condenser the refrigerant conveys heat to a warm environment and condenses to a high-pressure liquid. It is then converted back to a low-pressure mixture in the expansion valve.

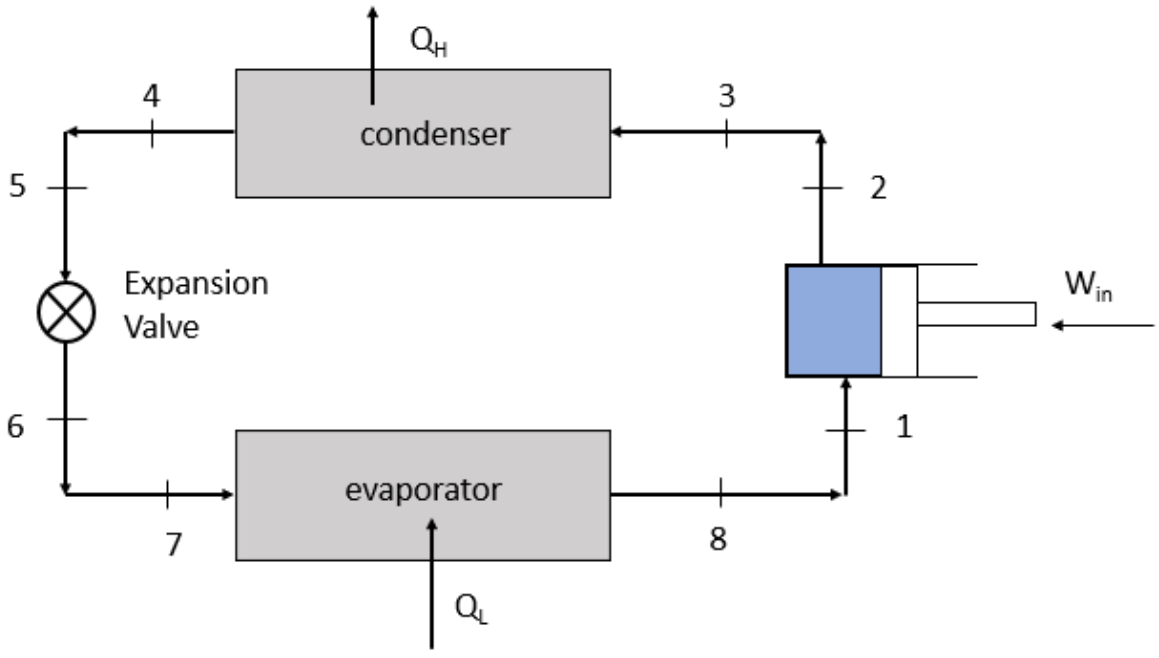

Figure 1.2: Vapor compression cycle schematic diagram (Cengel and Boles, 2002)

Charamko developed a cooling system that uses phase change in a converging-diverging nozzle to decrease the working fluid's temperature. A heat exchanger is paired with the nozzle to remove heat from a refrigerated space. Figure 1.3 shows a schematic of this type of cooling system. A pump drives subcooled liquid into the nozzle. At the throat of the nozzle cavitation occurs so that a temperature drop occurs in the fluid and heat enters from the surroundings or heat exchanger. The fluid then condenses in the converging section of the nozzle and enters the radiator as a saturated liquid. Heat is then transferred to a warm environment.

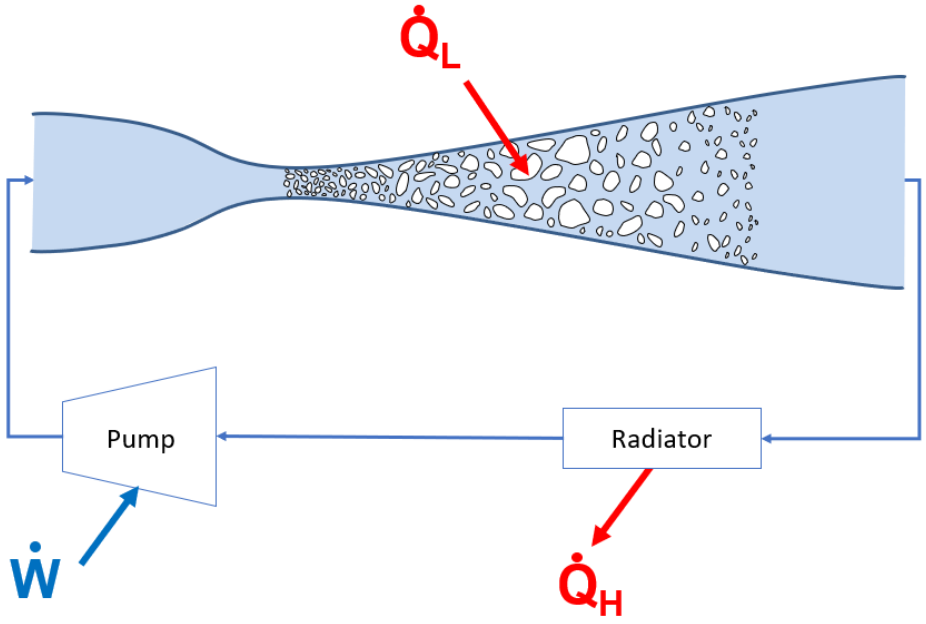

Figure 1.3: Non-vapor compression refrigeration cycle (Beck et. al, 2014)

The cavitation number is used as a measure of how close a liquid is to cavitation and is defined as follows (Brennen, 2013):

$$\boldsymbol{\sigma = \frac{P_\infty - P_v(T_\infty)}{\frac{1}{2}\rho_L U_\infty^2}} \qquad \textbf{(1.1)}$$

Where σ is the cavitation number, P_∞ is the pressure of the fluid, T_∞ is the temperature of the fluid, P_v is the saturation pressure of fluid, ρ_L is the liquid density of the fluid, and U_∞^2 is the

average velocity of the fluid squared. At large values of cavitation number, single phase liquid flow is developed, and at small cavitation numbers, cavitation and nucleation will initiate. Cavitating structures in nozzles have been categorized into attached wall cavitation, shear cavitation, swirl cavitation, and travelling bubble cavitation. Attached wall cavitation featured vapor attached to the walls of the nozzle. Shear cavitation existed in nozzles with rapid expansion and was a liquid jet surrounded by vapor. Swirl cavitation was like shear cavitation where the flow exited an orifice as a liquid jet surrounded by a large vapor region. Travelling bubble cavitation existed when trapped gasses separated from the liquid at pressures lower than the vapor pressure (Wilms, 2016).

Alkotami et al (2015) performed a study on the cooling effects of cavitation for water, R134a, R123a, and R22 and produced coexistence and spinodal curves using the van der Walls and Peng-Robinson Equations of State (Figure 1.4 and 1.5). P/P_c is the pressure normalized by the critical pressure and is called the reduced pressure, T/T_c is the temperature normalized by the critical temperature and is called the reduced temperature, and V/V_c is the specific volume normalized by the critical specific volume and is called the reduced specific volumes. These curves show when cavitation phase change is likely to occur and where the vapor dome is based on reduced pressure, specific volume, and temperature. The spinodal curve separates the stable and the metastable region in the vapor dome. It represents the limit of theoretical metastability, where a metastable liquid is a liquid in tension (Trevena, 1987). The spinodal curve can be used to predict when cavitation will occur during a constant temperature process where pressure is being reduced. The coexistence curves represent the beginning of the metastable region and the saturation vapor dome.

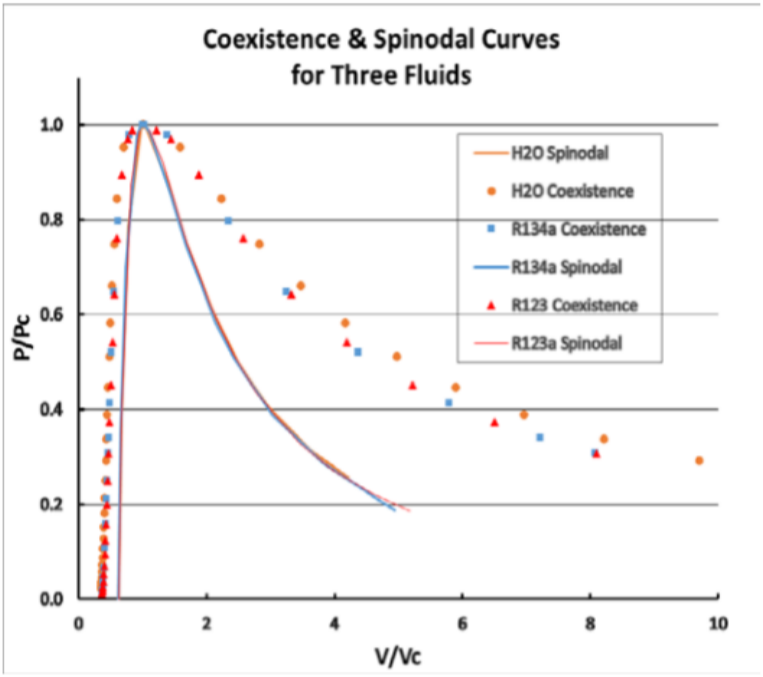

Figure 1.4: Coexistence and Spinodal Curves (reduced pressure vs reduced specific volume) (Alkotami et al, 2015,) (used by permission)

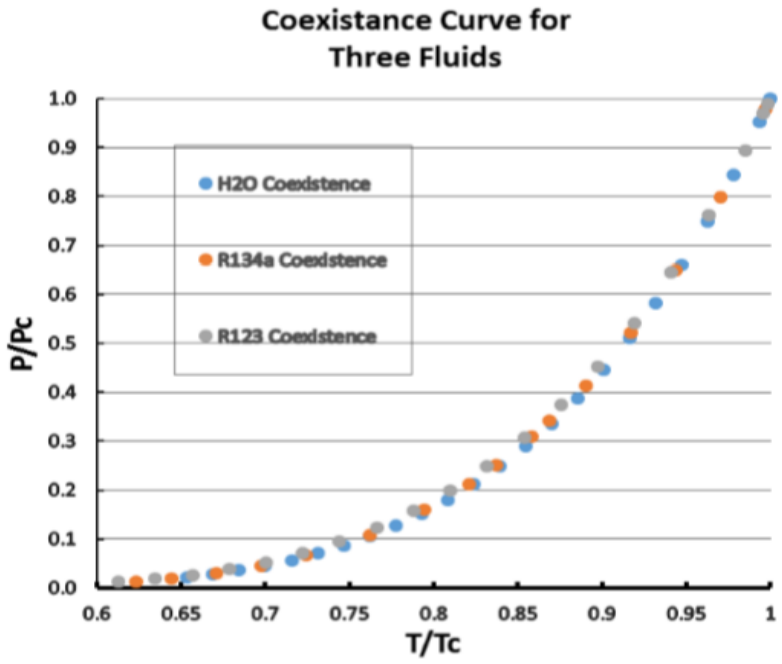

Figure 1.5: Coexistence curves (reduced pressure vs reduced temperature) (Alkotami et al, 2015) (used by permission)

Latent heat of vaporization and temperature were also examined, and the results are displayed in figures 1.6 and 1.7. λ is the latent heat of vaporization normalized by the corresponding latent

heat of vaporization at the triple point. The latent heat of vaporization is the energy required for phase change and the temperature drop is the estimated temperature drop in the working fluid during cavitation. These plots show that a cooling process with cavitation is feasible because of the theoretical temperature drop in the working fluids. A heat exchanger surrounding this temperature drop could cool or refrigerate a space.

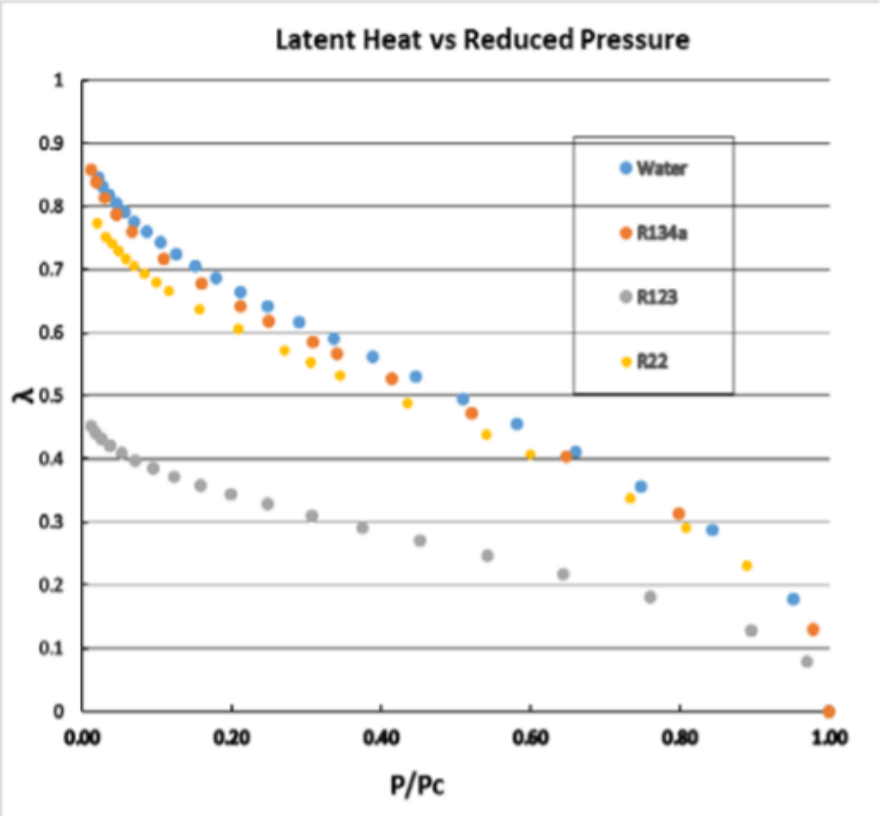

Figure 1.6: Latent heat of vaporization (λ) vs reduced pressure (Alkotami et al, 2015) (used by permission)

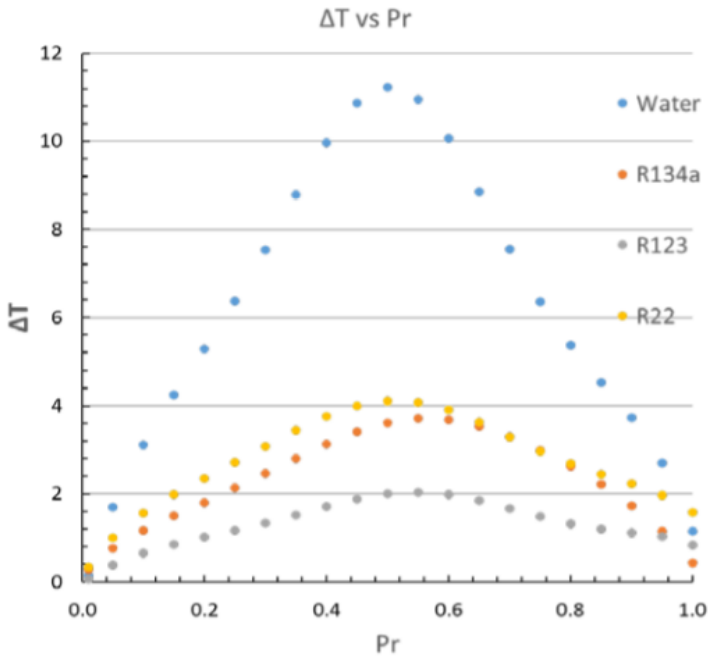

Figure 1.7: Temperature drop vs reduced pressure (Alkotami et al, 2015) (used by permission)

Simões-Moreira and Bullard, 2003, used one-dimensional jump equations to do a numerical simulation of the flow properties at the cavitation evaporative flash in a nozzle exit section. Pressure, quality, specific volume, temperature, velocity, metastability (Π) and mass flux were examined for R-22, R-134a, and R-600a. The pressure before the cavitation flash decreased as metastability increased for each fluid. The pressure after the cavitation flash also decreased but the change in pressure across the flash decreased with metastability as well. The quality after the cavitation flash increased with increased metastability along with the specific volume.

The results of the simulation show a decrease in downstream fluid temperature with an increase in pre-flash metastability. This increase in pre-flash metastability is an increase in fluid tension and a decrease in pressure before cavitation. By delaying cavitation and increasing metastability the process moves farther down the spinodal curve and becomes a more efficient cooling process.

Nozzle optimization is a possible solution for delaying cavitation. Cavitation occurs at nucleation sites where a bubble is forming, or a surface defect exists. Separation in the diverging section leads to flow circulation along the wall of the nozzle. Schmidt (2016) investigated this using a glass nozzle, high speed camera and particle image velocimetry to analyze cavitation and velocity fields. The cavitation occurred just beyond the throat and correlated with the point of separation. After, the flow separated from the wall of the nozzle recirculation occurred along the wall. This was shown with PIV and CFD analysis. Nozzle optimization is often done using the pressure recovery factor Ct, which is defined in the following equation:

$$Ct = \frac{P_2 - P_1}{\frac{1}{2}\rho_m V_1^2}, \quad \textbf{(1.2)}$$

where ρ_m and V_1 are the density and velocity at the entry to the diffuser, P_2-P_1 is the difference in pressure from the entry of the diffuser to the outlet (Abdul-Ghani and Amini, 1992). Abdul-Ghani and Amini (1992) analyzed diffuser angles with homogenized two-phase flow to find the optimal diffuser angle. Using an experimental setup where pressure was measured along the diffuser section, the pressure recovery factor was analyzed for a 5°, 7°, 9°, and 11° diffuser angle. The 7° angle diffuser produced the optimal pressure recovery. Optimal pressure recovery occurs when flow separation is limited and thus optimizing pressure recovery factor would lead to an optimized nozzle for cavitation.

The temperature effects of cavitation have been experimentally studied as well. Petkovšek and Dular (2013) used a blow down system and a converging-diverging nozzle to generate cavitation in hot water. The cavitation was visualized using a high-speed camera and the temperature variation in the nozzle was measured using a high-speed IR camera. At cavitation numbers of 1.3, 1.8, and 2.3, the temperature dropped around one Kelvin. This temperature drop occurred near the throat of the Venturi nozzle where cavitation would initiate.

Mann and Eckels (2016) used R-134a in a converging-diverging nozzle and measured temperature drop normalized with the characteristic temperature drop and the Nusselt number for a variety of cavitating flows. A temperature drop as high as 16.3 °C and a heat transfer coefficient as high as 285 kW m^{-2} K^{-1} were observed.

Ahmed (2017) used a blowdown system with a vacuum back pressure chamber to study cavitation in a converging-diverging nozzle. Ahmed examined cavitation initiation as well as steady state cavitation. Cavitation initiation exhibited metastable behavior where the flowrate in the system reaches a maximum before cavitation and exhibiting a choked-flow condition (Figure 1.8). This illustrates the pressure dipping below the saturation pressure before cavitation occurs.

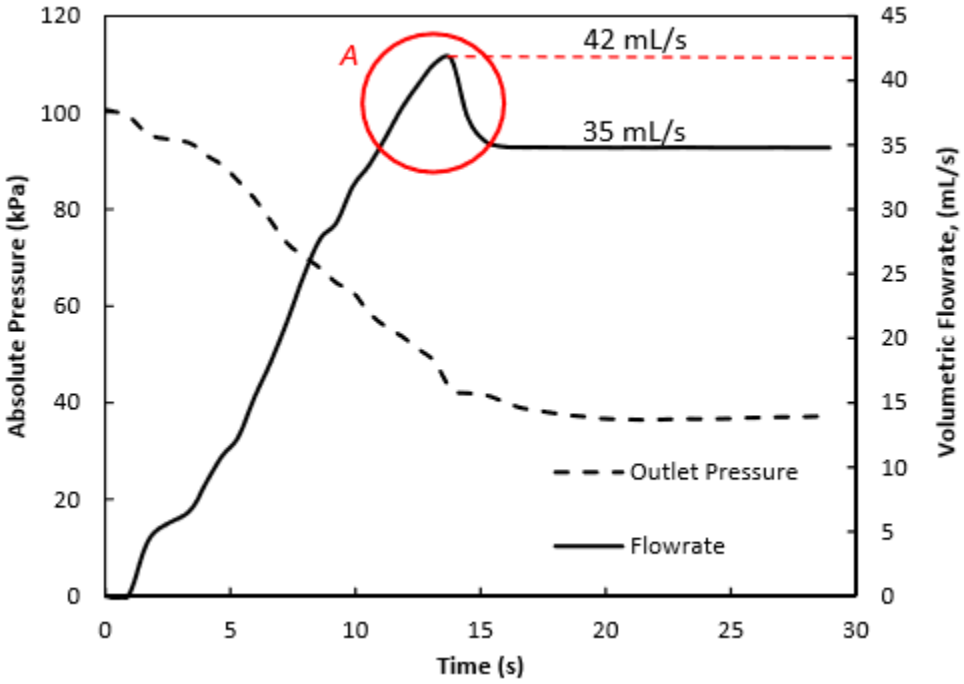

Figure 1.8: Flow rate behavior with decreasing outlet pressure (Ahmed, 2017) (used by permission)

Based on the flow rates and nozzle dimensions the throat pressure was calculated to be -23.2 kPa absolute pressure. This means the liquid was likely in tension before cavitation. Pressure distributions have been measured in a converging-diverging nozzle during choked flow behavior

at steady state. As backpressure is increased the position of the shock, or flash, that produces choked flow moves closer to the throat (Davis, 2008). The shock position corresponds to the cavitation front, as two-phase sonic velocities are smaller than single-phase sonic velocities. The flow is reaching sonic conditions when it cavitates.

Negative absolute pressures are often found in metastable liquids and have been produced experimentally up to -150 MPa with water in static measurements (Imre et al, 1998). The methods to produce these extreme negative pressures involve sealing water under vacuum in a Berthelot tube where water is then heated to a temperature where the liquid is at vapor pressure. Then the liquid is cooled until negative absolute pressures are reached. The pressures are measured by measuring the deflection in the tube walls. Another method to measure tension in water is known as the centrifugal method and was used by Briggs (1950) to achieve negative or tension pressures of 27.7 MPa at 10°C. This method rotates a capillary tube with one end open to atmosphere. The angular velocity is increased until cavitation occurs. The pressure at the moment of cavitation is known as the breaking tension and is the value Briggs measured in his experiment. These experiments produce repeatable results of liquids in tension (Trevena, 1987). In dynamic flows negative pressures can be measured using a strain gauge and calculating negative pressures from its electric signal. Modern pressure transducers use strain gauge systems to measure positive pressure and can be adapted to negative pressure applications (Imre et al, 1998). A pressure transducer has been used in conjunction with a Berthelot tube made of steel and negative absolute pressures of 3 MPa were measured. The smaller values of liquid tension in this method can be ascribed to degassing methods used with the steel Berthelot tubes (Trevena, 1987).

Pressure measurement system response to dynamic pressure changes has been studied and modelled in literature. Doebelin (1990) described a first-order system that could be used to describe a pressure transducer response in a heavily damped, slow-acting, liquid filled system in his book *Measurement Systems: Application and Design.* The pressure measurement system included a pressure transducer and capillary tube connected to the site of pressure measurement. The derivation of the first order model sets the pressure difference across the capillary tube equal to the viscous forces in the connecting tube and uses a mass balance to relate the change in volume in the system to the velocity of the liquid in the connecting tube. Doebelin (1990) used the compliance of the pressure transducer to relate the change in volume to the change in pressure in the transducer chamber. His model assumed that no gas pockets exist in the pressure measurement system. The resulting time constant is shown in Equation 1.3, where C_{vp} is the compliance of the pressure transducer with units m^3/Pa, μ is the dynamic viscosity, L is the length of the capillary tube, and d is the diameter of the tube.

$$\boldsymbol{\tau = \frac{128\mu L C_{vp}}{\pi d^4}} \qquad \textbf{(1.3)}$$

The compliance of a pressure transducer is related to the geometry and material properties of the transducer diaphragm and thus is a constant.

A linear second order model was described by Fowler (1963) that included the inertial effects of the liquid in a pressure measurement system. The pressure measurement system was considered analogous to a mass-spring damper system. An equivalent mass was derived from the kinetic energy of the fluid and added to the mass of the transducer bellows or diaphragm. An equivalent damping factor was derived from the viscous effects in the tube. The spring constant was related to the compliance of the pressure transducer. These values were used to find the natural frequency and damping ratio and define a second order differential equation of pressure.

Research Goals/Objectives

Directly Measure Pressure

Previous experimental work done by Ahmed (2017) and Schmidt (2016) used glass nozzles and a high-speed camera to successfully visualize the cavitating flows in the nozzle. The pressure distribution in the nozzle was then calculated from measured flow rates and nozzle geometry. The current work will measure the pressure in the nozzle directly. This will give a more in depth understanding of the flow parameters and the pressure just before cavitation. These pressure measurements were made during steady state cavitation and during cavitation initiation. During steady state cavitation the pressure measurements will give insights into flow parameters in the nozzle and the exact pressure at the cavitation front. The metastable region occurs just before cavitation initiation and the pressure measurements during the transient metastable behavior shows where on the spinodal curve the fluid state lies.

Capture Flow Visualization with High-speed Camera

Flow visualization is critical to understand the length of the two-phase region and the location of the cavitation front. These parameters are critical to cooling potential and this work will used a high-speed camera to characterize them. This will allow for a direct comparison to the pressure measurements to give a complete picture of the cavitating flow parameters especially near the throat of the nozzle.

Chapter 2 - Experimental System

A blow down system was used to gather the pressure measurements and flow visualization of cavitation in a converging-diverging nozzle. This section details the blow down system and the instrumentation used to gather data

Blow Down System

The blow down system consisted of an upstream reservoir filled to consistent height at atmospheric pressure (Figure 2.1). A ball valve was placed at the exit of the reservoir to control when water is let into the system. A Coriolis flowmeter and rotameter gave two independent measurements of flowrate in the system and are placed just before the nozzle. At the entrance and exit of the nozzle are two thermocouples that measure the temperature of the water. Along the nozzle are eight pressure transducers that measure the pressure distribution in the nozzle. A high-speed camera was used to capture flow visualization footage of the cavitation in the nozzle. At the entrance to the downstream reservoir is another ball valve that is used to control the flow through the system. The pressure of the downstream reservoir was controlled using a vacuum pump and pressure gage that displays vacuum pressures. A schematic of this system is shown in Figure 2.1. Pictures of the system are shown in Figures 2.2 and 2.3.

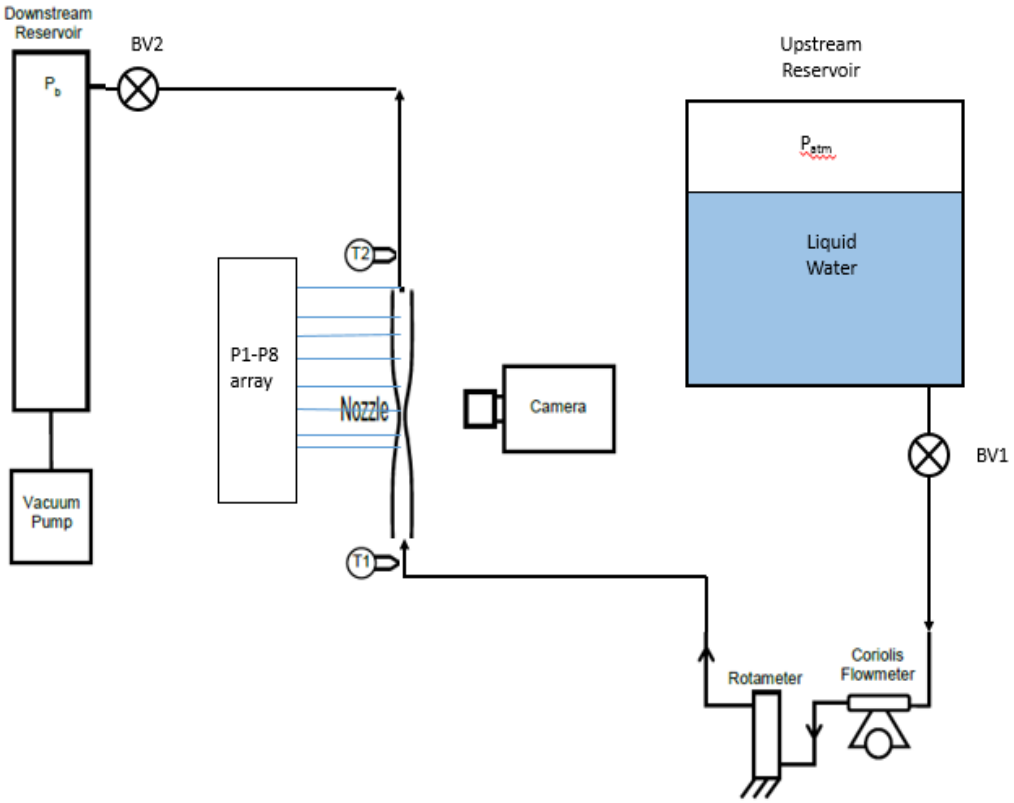

Figure 2.1: Blow down system schematic

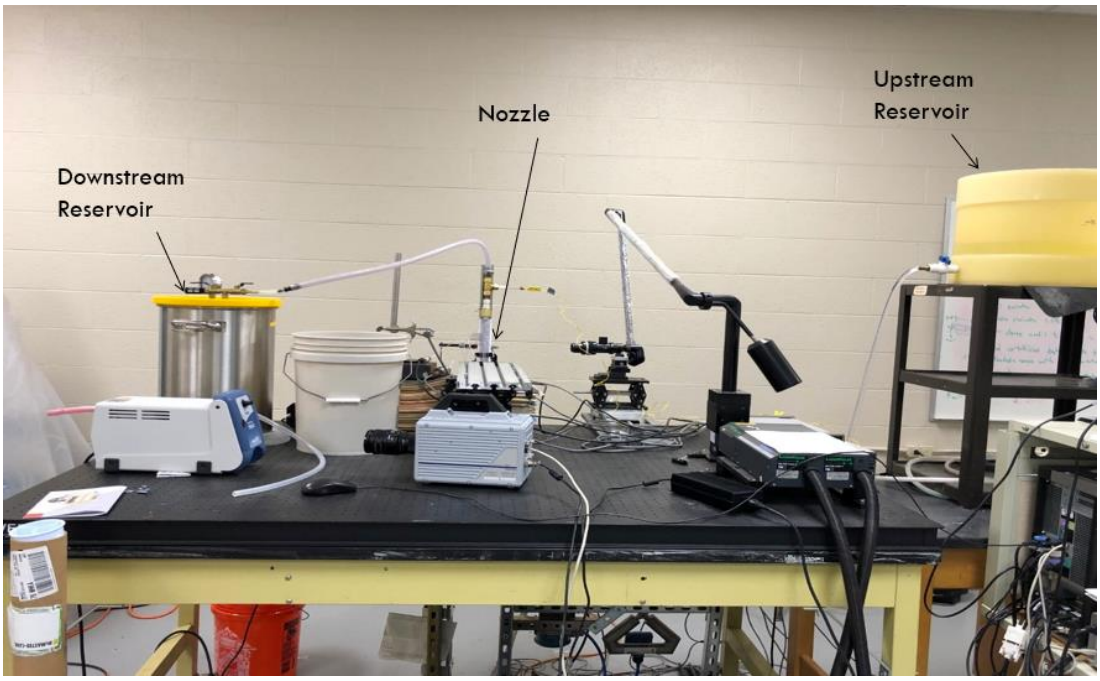

Figure 2.2: Blow-down system set up view from the front

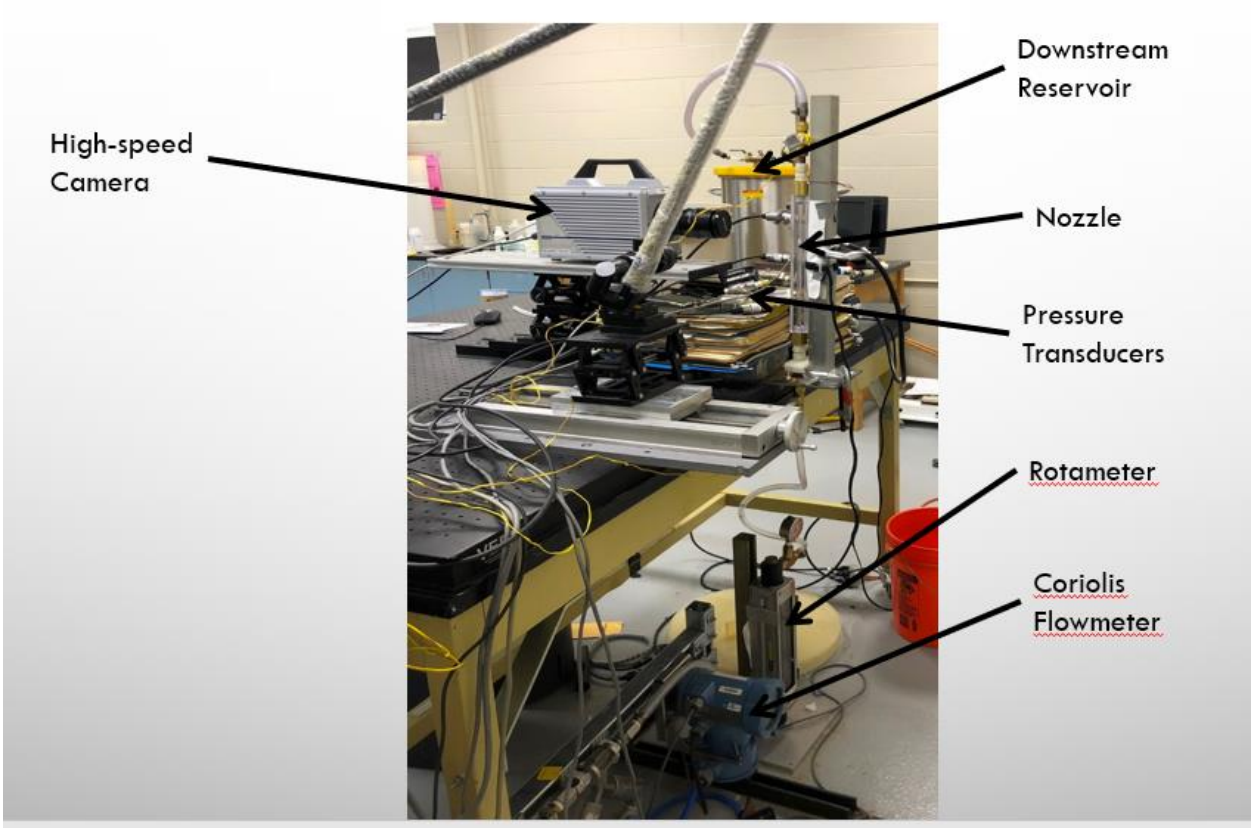

Figure 2.3: Blow-down system set up view from the back

Downstream Reservoir

The downstream reservoir was an 8.4 gallon vacuum tank that can hold a vacuum up to -30 inHg gage pressure. Due to the larger volume size the vacuum pressure remains steady for up to 5 minutes of experimental operation. This allows for longer steady state tests and better investigation of the transient behavior. The tank is fitted with quarter inch tube fittings and a brass ball valve labelled as BV2 in Figure 2.1. The tubing from the nozzle is half inch OD tubing and thus a reducer is required. A picture of the downstream reservoir is shown in Figure 2.4.

Figure 2.4: Downstream Reservoir

Nozzles

Three types of nozzles were used in the system. The glass nozzles acted as a link between the current work and previous work and to ensure there were no issues in the system. An opaque nozzle was used to gather preliminary pressure measurements and to test nozzle creation with 3D printing. The final nozzle was a clear 3D printed nozzle with pressure taps.

Glass Nozzles

The glass nozzles were hand blown nozzles made by the Kansas State University glass blower and all previous work has been done with the glass nozzles. They have a very smooth surface which leads to a smaller number of cavitation nucleation sites, less frictional losses and higher flow rates. The higher flow rates grant more metastability when compared to the plastic

nozzles. The geometry glass nozzle used by Ahmed (2017) was used as a model for the plastic nozzles, so the data could be compared.

Opaque Plastic Nozzle

The first 3D printed nozzle used was made of solid black opaque material. Also, the nozzle has a shorter entry length, converging section, and diverging section (Figure 2.5). This was due to the limitations of the University 3D printer. This nozzle had a much rougher surface compared to the glass nozzle because no post printing surface finishing was done. This led to greater friction factors and slower flowrates. The nozzle had 7 pressure taps 10 mm apart that connected to the flow through holes with a diameter of 0.75mm. Concentric to these holes were 1/8-inch NPT connections so that tubing could be attached to the nozzle and connect to pressure transducers. Figure 2.3 shows the dimensions of the nozzle and the pressure tap locations. At the inlet and exit of the nozzle are ¾ inch diameter holes with ¾”-16 straight thread. The hole also has a 37° bottom to match a flared fitting that screws into the hole making a seal. The fittings at the inlet and outlet have a 37° flare and matching threads and connect to ½ inch OD tubing.

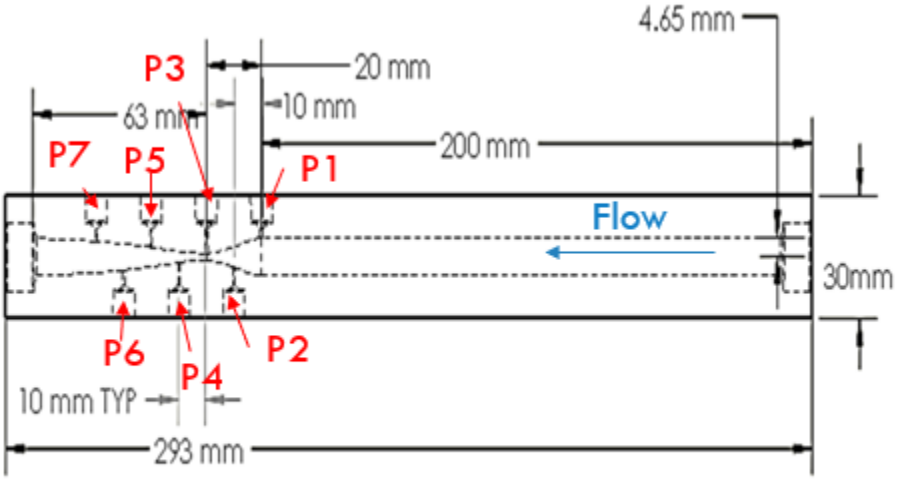

Figure 2.5: Dimensions of opaque nozzle

Clear 3D Printed Nozzle

The transparent 3D printed nozzle was modelled to match the geometry of the glass nozzle used by Ahmed (2017). This was done by creating a fifth-degree polynomial fit to the geometry of the glass nozzle and using that polynomial fit to generate the inner nozzle geometry of the new 3D printed nozzle. The nozzle was printed with a transparent resin and then with post processing the surfaces of the nozzle were smooth and became perfectly transparent. Manufacturing of the clear plastic nozzle was done by womp.xyz, a rapid prototyping company in New York. The smooth finish better approaches the smooth surface of the glass nozzles. Figure 2.6 and 2.7 show the geometry of the nozzle and an image of the finished nozzle. There are eight total pressure taps in the clear plastic nozzle, which are placed based on theoretical pressure predictions to get the most representative pressure distribution. These taps were made by drilling a 1/16th inch diameter hole close to the inner surface. Then using a 0.006" drill bit, small holes were drilled connecting the 1/16th inch diameter holes to the inside of the nozzle. These small holes limit the effect the tap has on the flow and are less likely to be nucleation sites for cavitation. A close-up image of these holes can be seen in figure 2.7. Figure 2.7 also shows the placement of the pressure transducers and the type of pressure transducers used with the nozzle. The inlet and outlet of the clear printed nozzle was the same as the opaque nozzle with a ¾"-16 straight thread and a 37° flare.

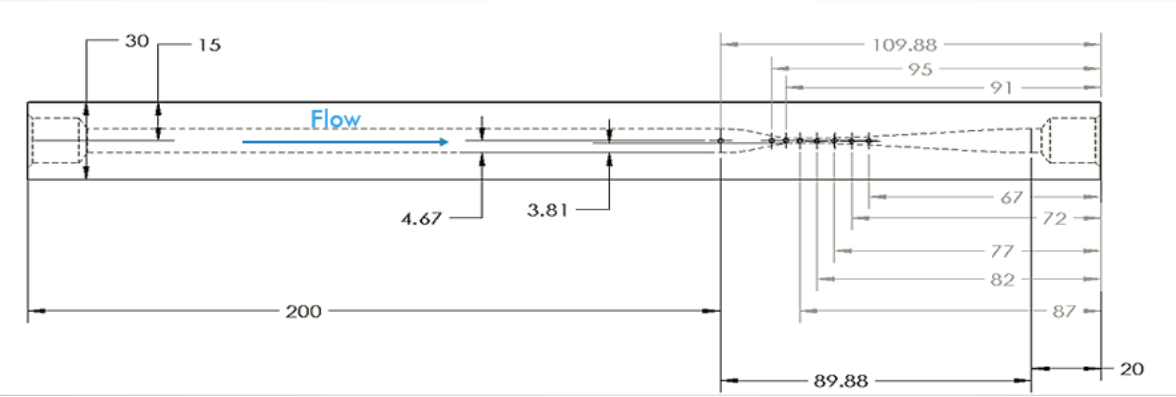

Figure 2.6: Clear 3D printed nozzle geometry and tap placement with all dimensions in millimeters

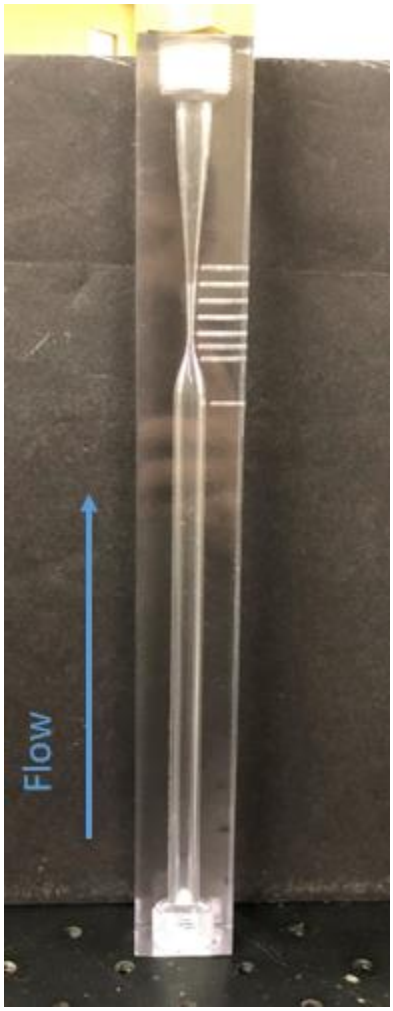

Figure 2.7: Picture of clear 3D printed nozzle

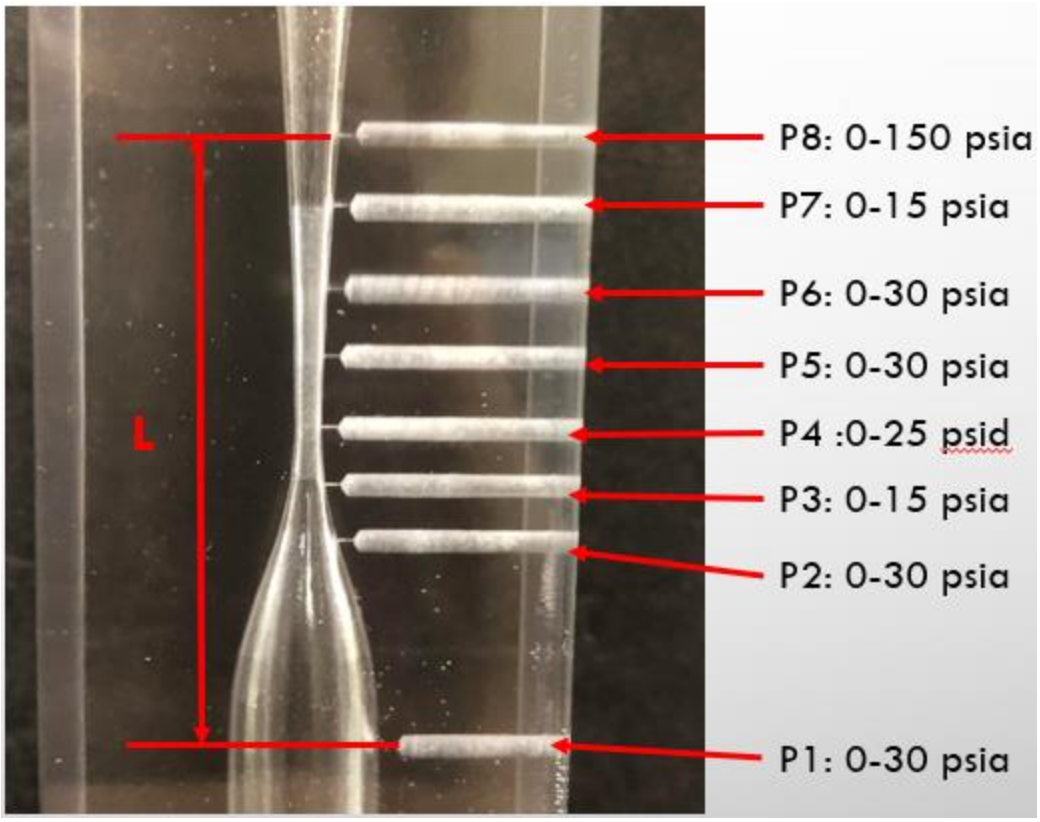

Figure 2.8: Close-up image of pressure taps and throat section with pressure transducer locations

Steel tubing with an outer diameter of 1/16th inch and an 0.006" inner diameter was epoxied in the 1/16th inch diameter holes in the nozzle. This tubing then connected to the pressure transducers. In order to provide strain relief on the nozzle a support structure was designed to support the steel tubing and can be seen in Figure 2.9. The support system was not always used as it became to constraining on the tubing and made it difficult to adjust the system.

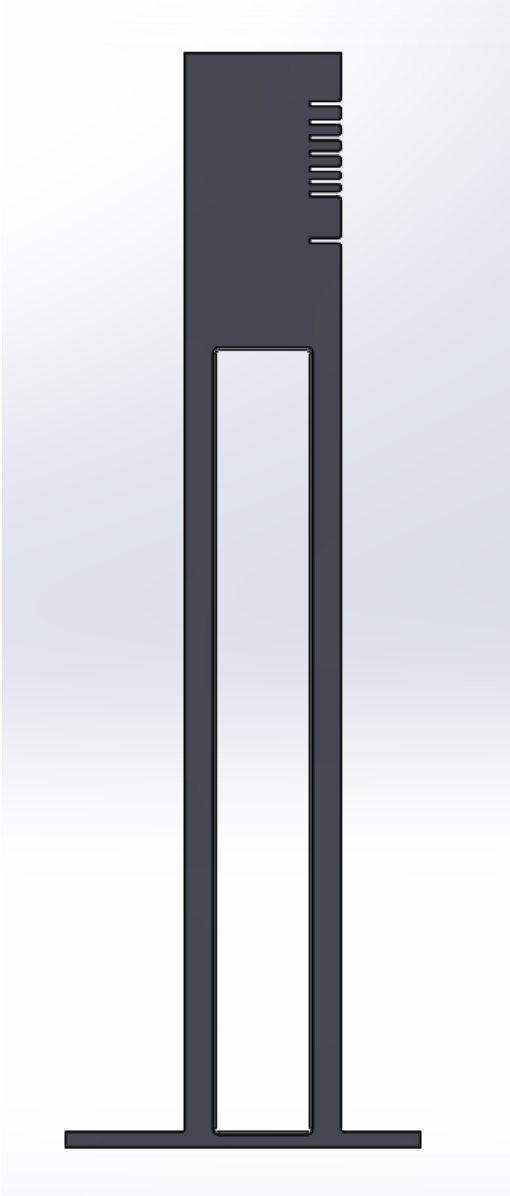

Figure 2.9: Steel tubing support structure

Data Acquisition System

The pressure measurements on the opaque nozzle were made using 0-30 psia pressure transducers on the converging section and the tap just after the throat. The remaining three taps were connecting to 0-150 psia pressure transducers. On the clear nozzle the pressure transducers used can be seen in Figure 2.8. In each experiment the flowrate was recorded using a rotameter

that measured the percent of the max flowrate which was 51 mL/s and a Coriolis flowmeter that had an output of frequency. Two K type thermocouples measured the temperature of the water in degrees Celsius. The outputs of the pressure transducers, thermocouples, and Coriolis flowmeter were collected with an HP 34970A data acquisition unit and then recorded on the lab computer. The equipment and sensors are detailed in Appendix A.

Flow Visualization

A high-speed camera was required to capture the cavitation phenomena due to the higher flow velocities in the throat. Standard video cameras record at thirty frames per second which is too slow and incapable of adequately capturing the flow through the throat of the nozzle. For high-speed imaging a proper camera, lens, and lighting were required.

High-Speed Camera

A Photron SA5 High Speed Camera was used to record the various flow conditions. The camera had a maximum resolution of 1,024 by 1,024 pixels with a frame rate of 7,000 frames per second at that maximum resolution. The fastest recording frame rate the camera was capable of was 775,000 frames per second with a resolution of 128 by 24 pixels. The camera was connected to a computer via Ethernet cable. The Photron Fastcam Viewer software was the accompanying software with the camera and gave flexibility in controlling resolution and framerate as well as analysis of recorded videos. An AF Nikkor 60 mm f/2.8D lens was used for recording.

Lighting

The high-speed camera requires more light than regular video cameras especially as the frame rate is increased. Since, higher frame rates are needed to capture cavitation, proper illumination of the nozzle is critical. To achieve this illumination two fiber optic halogen light sources were used. The light was sent through a sheet of printer paper into the back of the nozzle

to give a high intensity diffuse light source for the camera. Figure 2.10 shows one of these halogen light sources.

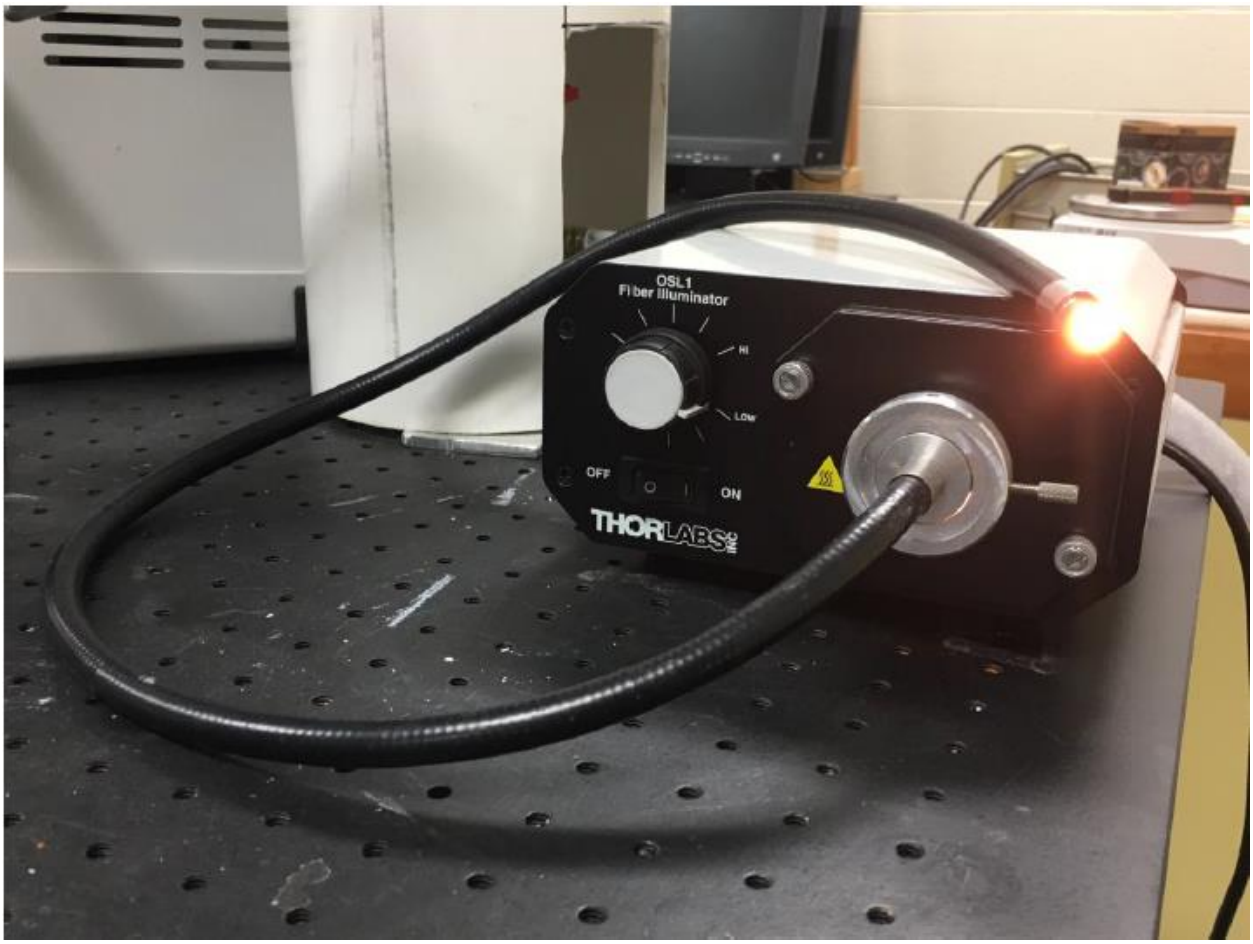

Figure 2.10: Fiber optic, halogen light source

Chapter 3 - Experimental Procedures

This section details the procedure used to run the blowdown system and collect data. The procedure outlined will include set up and calibration and the differing procedures for steady state measurements and transient measurements. Water was used in all experiments and was left at room temperature.

Set-up and Calibration

Before each test the upstream tank was filled to the same level to keep a constant inlet pressure between each experiment. The height of this fill level was measured to ensure a consistent nozzle inlet pressure. Also, the atmospheric pressure was measured using a mercury barometer. This measurement was then used to calibrate the pressure transducers to atmospheric pressure. The voltage reading was compared to the barometer reading to calibrate the bias in each transducer (Appendix A). Next, the downstream reservoir was pulled to a lower back pressure with a vacuum pump. This back pressure varied between experiments and depended on what data was needed. Then BV1 was opened to let water into the system and BV2 was opened slightly to fill the nozzle and pressurize the system. Once the system was filled, and small air bubbles were purged, BV2 was closed and a no flow pressure reading was taken. This gives another reference point for calibration because the pressure transducers are at fixed heights and the voltage can be compared to the known height of a water column. Once this calibration was complete the system was reading to be used for tests. The high-speed camera was mounted on a scissor jack platform, so the vertical height could be adjusted to properly view the nozzle. The Photron Fast Viewcam software was then used to adjust the framerate and resolution of the camera to get the best view of the nozzle.

Steady-State Measurements

The goal of the steady state measurements is to capture the pressure distribution in the nozzle during cavitation and compare that pressure distribution to the length of the two-phase region and the cavitation front. After completing the set up and calibration, BV2 is opened to start the flow through the blow-down system (Figure 2.1). Once flow is achieved data collection is started on the computer to gather pressure, flow, and temperature measurements. Next the high-speed camera was used to film the cavitation in the nozzle. The system is left to run until the memory in the camera is full. Once filming ended the data collection was turned off and BV2 stopped flow in the system. The data and video files are then saved to the respective computers and backed up for further analysis.

Transient Measurements

The goal of the transient measurements is to measure and characterize the metastable behavior that happens just before cavitation occurs. After performing the set up and calibration of the pressure transducers, the data collection was started. Then the high-speed camera was set to begin filming. While collecting data and film, BV2 was slowly opened to gradually increase the flow rate in the system until the valve was at full open. The valve was left at full open for a short period of time to let the system reach steady state. Finally, the valve was slowly closed to observe the transient behavior as the flow rate through the system lessens. Once the valve was closed the data collection and filming was stopped and the files saved. This method allowed for the comparison to the behavior just before cavitation and the behavior as cavitation stops.

Chapter 4 - Results and Discussion

This section includes a discussion of the results from the different experiments. The results from the glass nozzle were used as a diagnostic for the blow down system and a comparison of nozzle geometries. Because the glass nozzles were made by hand, each nozzle had a slightly different geometry, which affected flow parameters. This was characterized by measuring the steady state flow rate through each glass nozzle at the same back pressure. These findings gave insight on the creation of the geometry of the plastic nozzles. The opaque plastic nozzle was used to gather preliminary data on cavitation and flow through a non-smooth plastic nozzle. Pressure and flow rate measurements were gathered for steady state and transient behaviors. This allowed for study of metastable behavior and pressures during cavitation. The clear plastic nozzle allowed for the visualization of cavitation while getting direct pressure measurements. Pressure measurements were compared to the cavitation front and the length of the two-phase region in steady state tests. The observed metastable behavior in the flow rate and pressure measurements was compared to the visualized cavitation initiation.

Glass Nozzles

Several glass nozzles were made to analyze the effect of varying geometry on flowrate through a converging-diverging nozzle. Each of the glass nozzles were made by hand by the on-campus glass blower Jim Hodgson giving slight variation in geometry, but since there were all made with the same material and method the surface finish was the same and smooth for each nozzle. With the upstream and downstream pressures controlled the geometry is isolated as the only variable affecting the flow rate. Three separate nozzles were tested with nozzle 2 being the nozzle used by Ahmed (2017) (Figure 4.1). The flow rate varied from 14.3 mL/s to 32 mL/s at a back pressure of 16.15 kPa showing the geometry has a significant effect on flow rate through

the nozzle and thus other flow parameters as well. A higher flow rate will lead to lower pressures at the throat of the nozzle and thus lower cavitation numbers. With a greater chance of cavitation, the nozzles that give a higher flow rate are more useful for this study and the cooling-process for which the nozzle will be used.

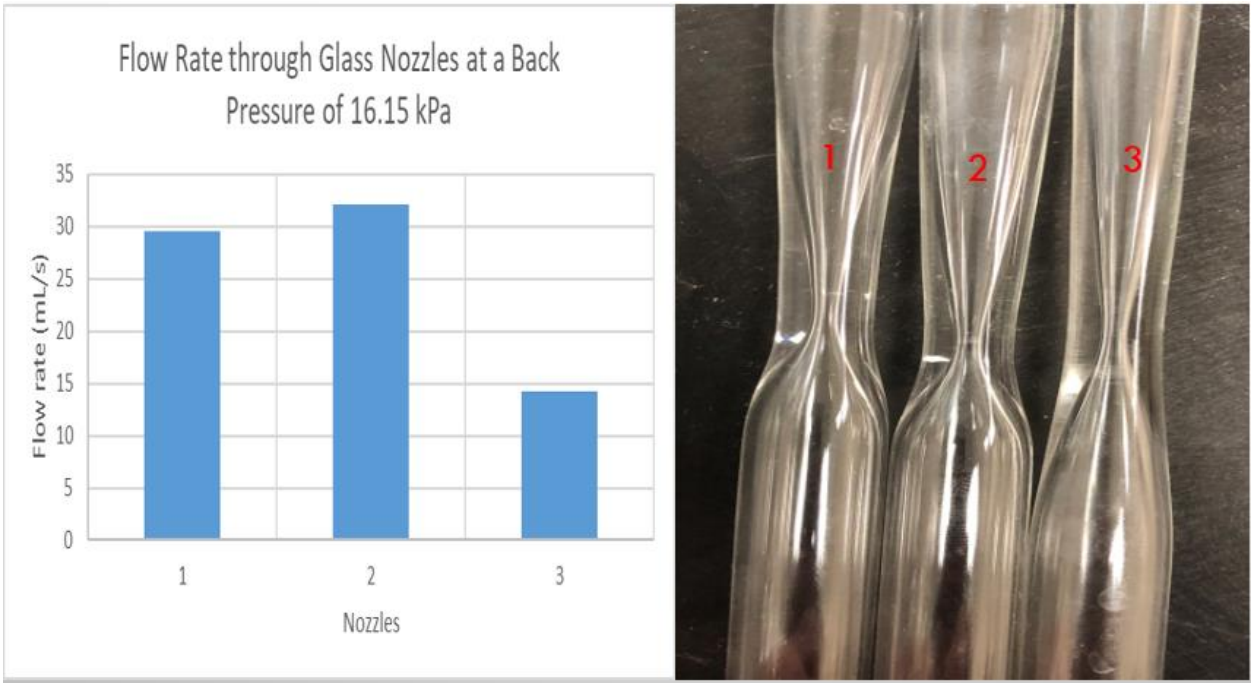

Figure 4.1: Steady State flow rate through each glass nozzle with nozzle 2 being the nozzle used by Ahmed, 2017

Nozzle 2 generated the highest flow rates and since Ahmed (2017) used this nozzle to generate past data, the geometry of this nozzle was used as a basis for the 3D printed nozzles. A fifth order polynomial was fitted to the nozzle to give diameter in terms of position along the nozzle (Ahmed, 2017). This polynomial was used to generate models in SolidWorks and then these models were used for 3D printing.

Metastable Behavior in Glass Nozzle

Metastable behavior was observed in the glass nozzle by slowly opening BV2, the ball valve at the entrance to the vacuum chamber. During this slow open process, the flow rate and

outlet pressure was recorded (figure 4.2). The flow reached a maximum value of 38 mL/s before cavitation occurred. Then after cavitation the flow rate dropped to 31 mL/s, while the outlet pressure was still decreasing. When closing the valve, the cavitating region in the nozzle slowly shrinks until the flow is single phase again. However, when closing the valve, the flow rate does not return to the maximum of 38 mL/s. This indicates that before cavitation the liquid is in the metastable state.

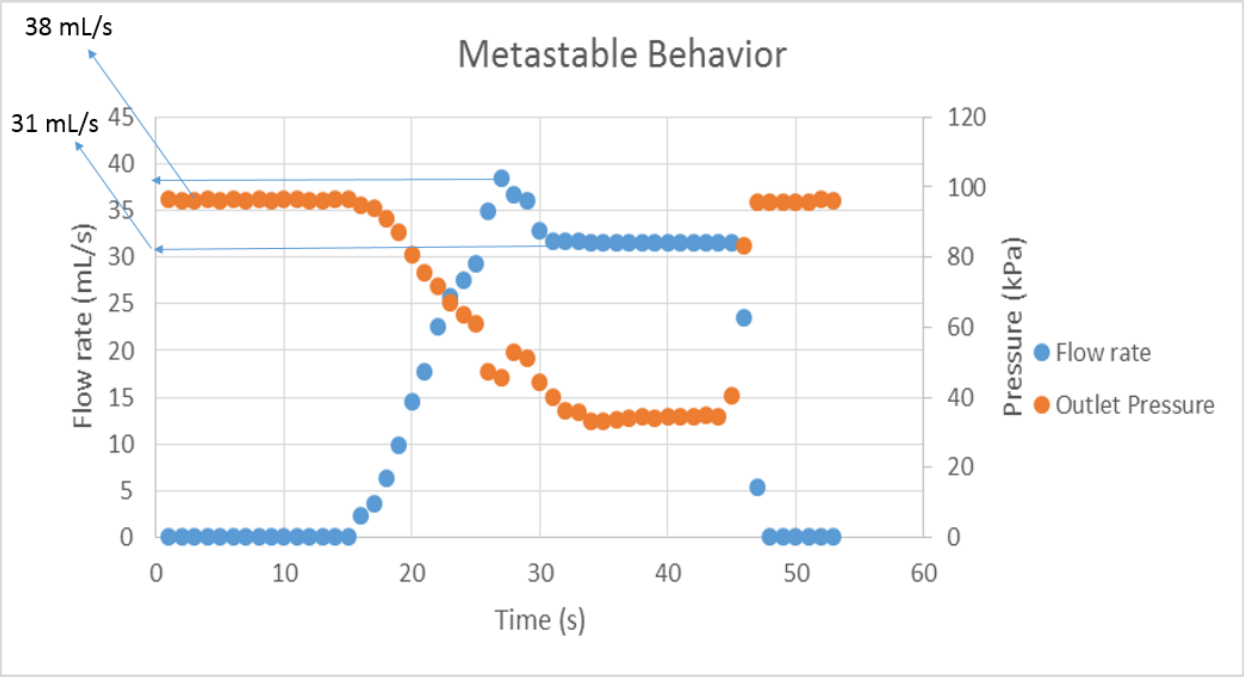

Figure 4.2: Flow rate through the glass nozzle indicating metastable behavior

Opaque Plastic Nozzle

The opaque black nozzle was the first iteration of the 3D printed nozzles and was made by Eric Wagner in the MNE shop. This nozzle allowed for the measurement of pressure at lower flowrates. The pressure was measured at seven locations along the nozzle including the throat. This was done at steady state and during a transient test to observe metastable behavior as well. The cavitation number and velocity were calculated at the throat for varying back pressures

during the steady state measurements. Flow rates, cavitation number at the throat, and velocity at the throat are calculated for the transient tests to see how the flow changes in the nozzle with time. Due to lower flow rates negative absolute pressure are not expected nor measured. The results are compared to pressure distribution calculations.

Steady-State Results

The steady state tests were performed according to the procedure outlined in section 3.2 and the tests were done at various back pressures. The flow rate through the nozzle was monitored to find the maximum possible flow rate (17.34 mL/s). This flow rate occurred during cavitating flow and is a result of a choked-flow condition. Because the nozzle is opaque and there is no visualization of the flow, it is impossible to know at which flowrate cavitation first occurs. Choked-flow occurs when the flow reaches the sonic condition and lowering the back-pressure of the system does not result in higher mass flow rates. This occurs in the cavitating flow due to the lower speed of sound in two-phase flows.

Figure 4.3 shows the volumetric flow rate variation through the opaque plastic nozzle as a function of absolute back pressure. The choked flow condition occurs at a back pressure of 47.5 kPa at the maximum flow rate of 17.34 mL/s. The presence of choked flow confirms that cavitation is present in the nozzle and producing two phase flow. The maximum flow rate is still much lower than the maximum flow rates present in the glass nozzles. This is likely due to the higher surface roughness in the nozzle and shorter diverging section, which contribute to larger frictional losses in the nozzle. These frictional losses were quantified using the pressure distribution in the nozzle.

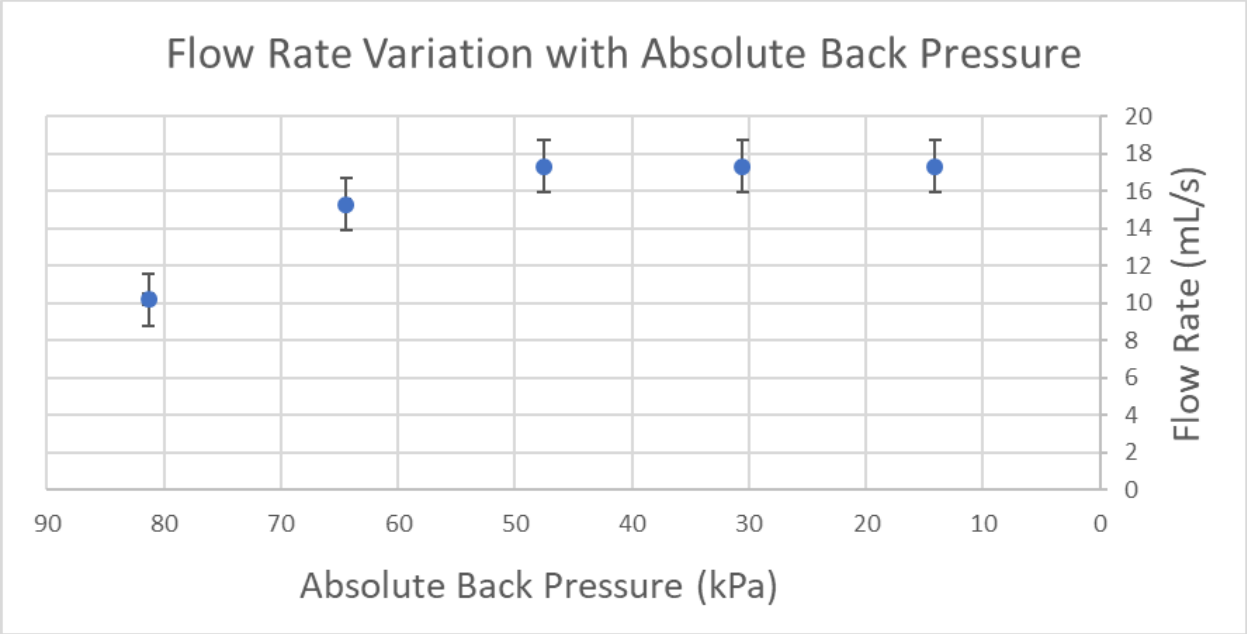

Figure 4.3: Flow rate variation in the opaque nozzle at different absolute back pressures

The pressure distribution in the nozzle was measured using seven absolute pressure transducers. The back pressure and flow rates for each test matched the data points displayed in figure 4.3, where the absolute back pressures are 81.3 kPa, 64.4 kPa, 47.5 kPa, 30.5 kPa, and 14.1 kPa. These back pressures corresponded to a normalized back pressure of P_b/P_{inlet} = 0.8, 0.63, 0.47, 0.30, 0.15 respectively. The pressure was normalized with the inlet pressure, and the position was nondimensionalized with the length of the nozzle. The throat of the nozzle is located at x/L = 0.333 and is the third data point shown in figure 4.4, which shows the pressure distribution in the nozzle. The throat pressure was the same for P_b/P_{inlet} =0.47, 0.30, and 0.15 due to the choked flow condition. The velocity of the flow through the throat was the same for the lowest three back pressures. Table 4.1 shows the throat pressure, throat velocity and the cavitation number at the throat for each back pressure.

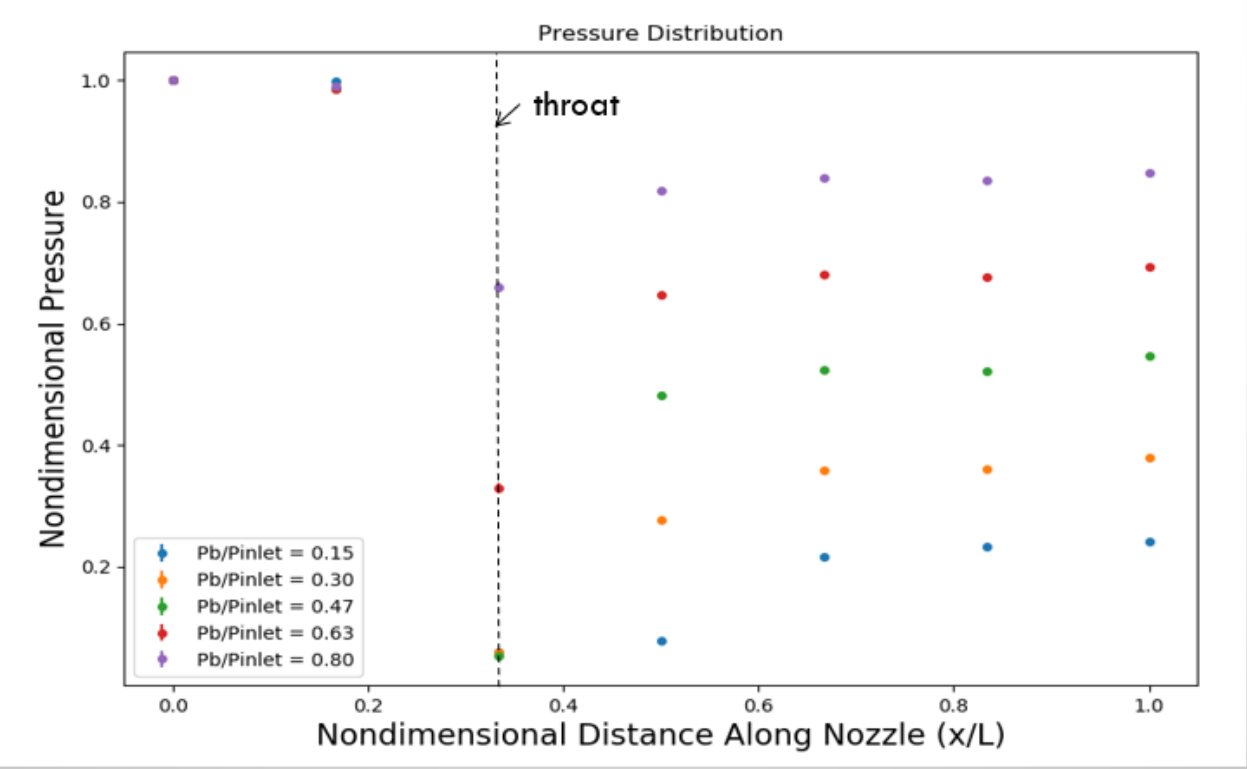

Figure 4.4: Pressure Distribution in the opaque nozzle at different back pressures

Table 4.1: Flow parameters at each back pressure

Back Pressure (kPa)	Pb/Pinlet	Throat Pressure (kPa)	Throat Velocity (m/s)	Cavitation Number
81.3	0.80	68.3 ±0.8	5.77	3.97 ±0.017
64.4	0.63	34.5 ±0.8	8.66	0.858 ±0.017
47.5	0.47	6.30 ±0.8	9.81	0.0825 ±0.017
30.9	0.30	6.90 ±0.8	9.81	0.0950 ±0.017
14.1	0.15	6.00 ±0.8	9.81	0.0762 ±0.017

At lower back pressures the cavitation number, σ, is much smaller than one suggesting that cavitation is likely to occur. The water in the nozzle at 20 °C with a saturation pressure 2.339 kPa, which is lower than the throat pressure of 6.00 ±0.8. Due to the low cavitation number and

the choked-flow condition, it is known that cavitation is occurring. This means that cavitation can initiate in a fluid at an average pressure above the saturation pressure, due to pressure dips in turbulent eddies in the flow, or that the pressure dipped below saturation pressure between the throat and the next pressure measurement. The high throat velocities and presence of nucleation sites in the nozzle increase the chances of cavitation. Rough surfaces and surface defects, such as a pressure tap, act a nucleation sites for cavitation. In the opaque nozzle a pressure tap of diameter 0.75 mm is present at the throat, where the lowest measured pressure occurred. Also, the plastic has an inherent surface roughness that is greater than the smooth surfaces of the glass nozzle. These factors act as nucleation sites that increase the likelihood for cavitation.

Surface defects and surface roughness also increase the frictional losses through the plastic nozzle. When the flow is turbulent, as is the case with lower back pressures, the frictional losses depend on the surface roughness. These frictional losses contribute to the lower flow rates through the plastic nozzle when compared to the glass nozzles. When cavitation occurs, the flow becomes two-phase, which also increases the frictional losses as described in the following equation:

$$\frac{dP}{dz}\Big)_f = \frac{dP}{dz}\Big)_{f,lo} * \phi_{lo}^2 \quad \textbf{(4.1)}$$

Where $\frac{dP}{dz}\Big)_f$ is the pressure drop due to friction, $\frac{dP}{dz}\Big)_{f,lo}$ is the liquid single-phase pressure drop due to friction, and ϕ_{lo}^2 is the two-phase multiplier. The two-phase multiplier is calculated using empirical correlations and is one when the flow is single-phase liquid and greater than one when the flow is two-phase (Collier and Thome, 1994). Due to cavitation and thus two-phase flow being present in the opaque plastic nozzle at lower flow rates, the frictional losses in the nozzle are higher. Also, the diverging section is shorter in length. This slight geometry change leads a greater chance of separation in the diverging section and larger frictional losses. The low

flow rates in the opaque plastic nozzle are due to the increased friction from surface defects and roughness, two-phase flow at lower velocities, and separation in the diverging section.

Transient Results

The transient tests were done to observe the pressure response during the metastable behavior seen previously in the glass nozzles (Figure 4.2). As the flow rate increased to a maximum prior to cavitation the pressure decreased to a minimum. Once cavitation occurred and choked flow initiated the flow dropped and the pressure increased. This metastable behavior is observed in the glass nozzle with a maximum flow rate of 38 mL/s and a choked-flow rate of 31 mL/s. This represents a significant change in flow through the nozzle at the onset of cavitation. In the opaque nozzle no significant change in flow rate was observed. The transient tests were done at nearly the same back pressures used in the steady state tests, excluding 81.29 kPa. The pressure distribution was measured as a function of time and the location of each pressure transducer in reference to the nondimensional distance (x/L), where L is the length of the region of pressure measurement, is given in Table 4.2. Figure 4.5 and 4.6 shows the results from the transient tests.

Table 4.2: Pressure transducer location in the opaque nozzle

Location (x/L)	Pressure Transducer
0.0	P1
0.167	P2
0.333 (throat)	P3
0.5	P4
0.667	P5
0.833	P6
1.0	P7

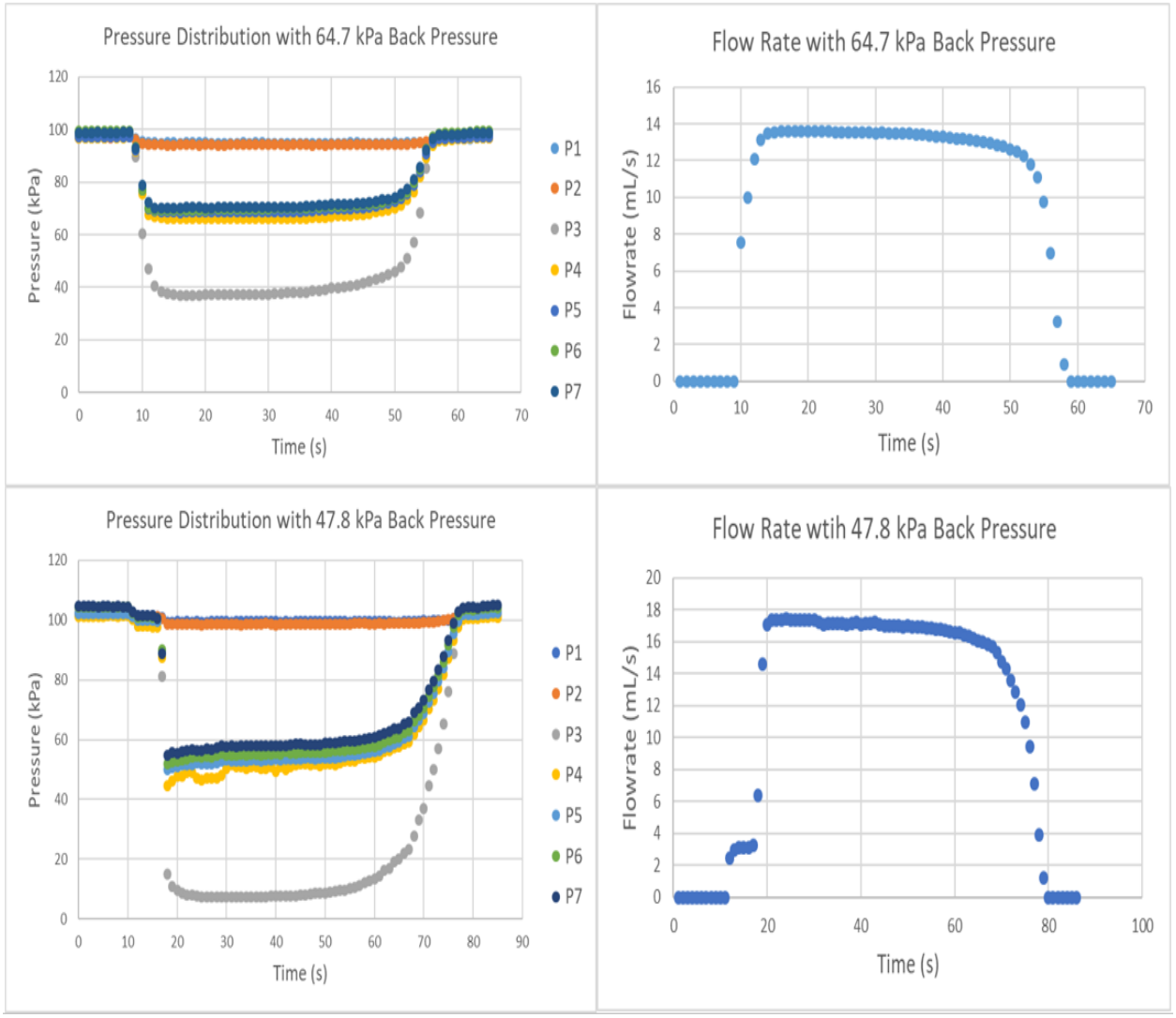

Figure 4.5:Opaque nozzle transient test pressure and flow results at high back pressures

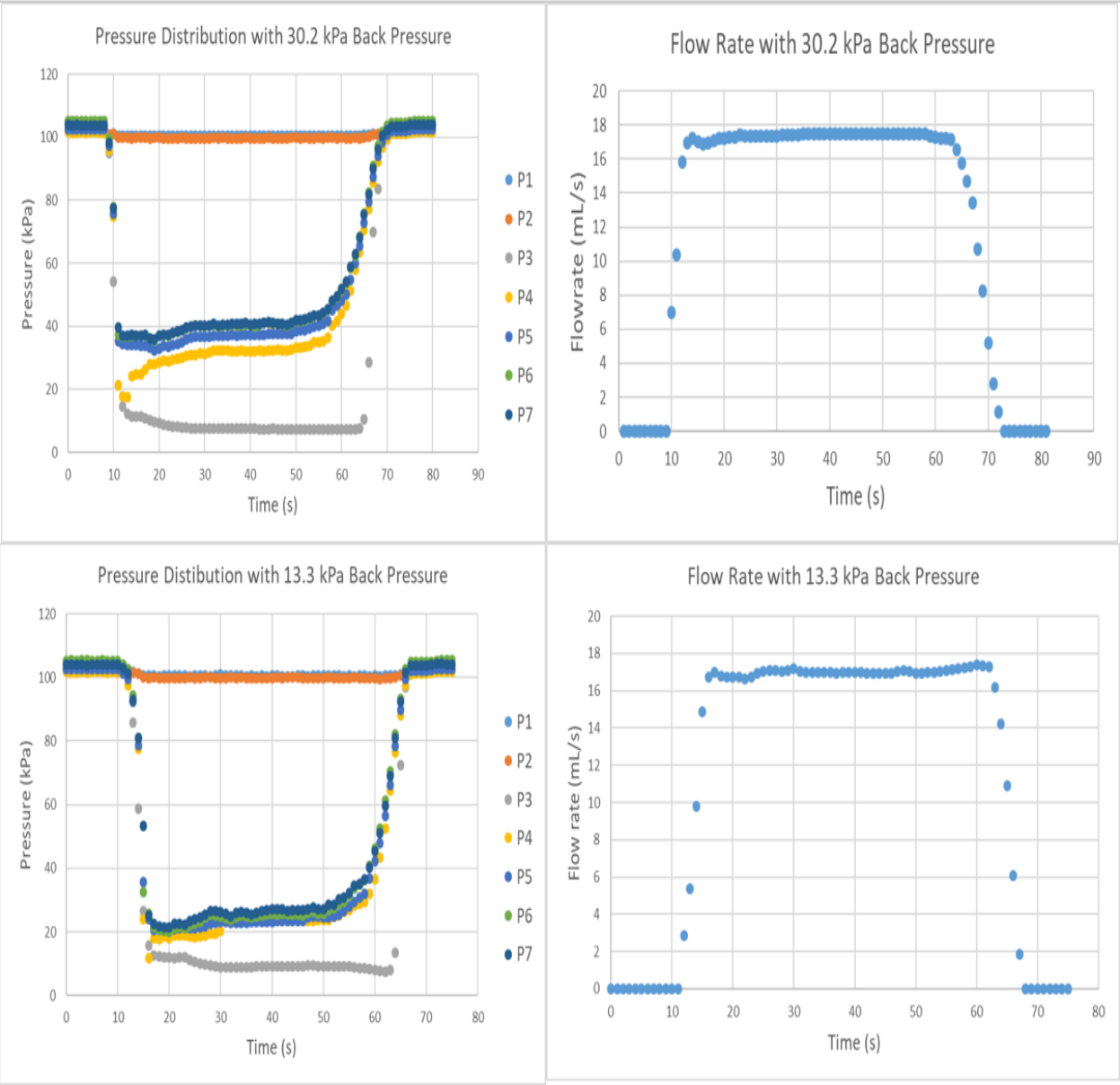

Figure 4.6: Opaque nozzle transient test pressure and flow results at low back pressures

The pressure and flow responded with pressure inversely related to flow rate. At a back pressure of 64.7 kPa the throat pressure minimum was not low enough to achieve cavitation, which was also shown in the steady state tests. With no cavitation, the 64.7 kPa back pressure test exhibited no metastability. At lower back pressures the throat reached a minimum pressure

of 7.40 ±0.8 kPa, which corresponds to a cavitation number of 0.105 ±0.017. The pressure response at the throat shows no indication of metastability due to its smooth decrease to the minimum value. However, the response just downstream of the throat at P4 does indicate metastability. In the 30.2 kPa back pressure test, just before reaching the choked-flow state, the pressure response dips to a minimum of 17.6 kPa that is lower than the steady state pressure, 32.3 kPa, for the cavitating flow. Ahmed, 2017, showed that the cavitation front occurred downstream of the throat in the glass nozzles. This dip in pressure at P4 could be a result of cavitation initiation occurring downstream of the throat during metastability.

However, the flow rate during the transient test did not exhibit a high degree of metastable behavior. In the 30.2 kPa back pressure test, the flow reached a peak of 17.25 mL/s before dipping to 16.90 mL/s at 13 seconds. The difference of 0.35 mL/s is much smaller than the difference of 7.0 mL/s seen in the glass nozzle during metastable behavior. The small difference in the opaque nozzle is above the uncertainty of ±0.022 mL/s. The opaque nozzle does exhibit metastable behavior but due to surface defects cavitation occurs sooner when compared to the glass nozzle. This results in less metastability.

Opaque Plastic Nozzle Conclusions

The opaque nozzle allowed for pressure and flow measurements in a cavitating flow. The steady state results showed choked-flow conditions at lower back pressures, meaning cavitation occurred within the nozzle. The measurements showed low cavitation numbers even though the measured pressure was above saturation pressure. The transient tests resulted in less metastability compared to the glass nozzle and the pressure response only displayed metastable behavior downstream of the throat. This could be from the cavitation front being downstream of the throat but without visualization this could not be confirmed. Lack of flow visualization and

lower flow rates through the opaque nozzle made comparisons to data from Ahmed, 2017, difficult.

Clear Plastic Nozzle Results

The clear 3D printed nozzle allowed for direct pressure measurements, flow rate measurements, and flow visualization. The clear 3D printed nozzle was made by womp.xyz, a rapid prototype manufacturer in New York. Steady state pressure and flow data was gathered for a variety of back pressures and for single and two-phase flows. High-speed camera footage was gathered for each two-phase flow condition in order to visualize the cavitation front, and the two-phase flow behavior. This allowed for a correlation between pressure measurement and the location of two-phase flow in the nozzle. Transient tests showed the degree of metastability within the clear 3D printed nozzle and the development of cavitation in the nozzle. These tests resulted in direct pressure and flow measurements and flow visualization during the unsteady development of cavitation in the nozzle.

Steady-State Results

The flow rate in the clear plastic nozzle was measured at varying back pressures to find the maximum flow rate and to check for the choked-flow condition (Figure 4.7). The maximum flow rate was 24.48 mL/s, which is less than the maximum flow rate of 38 mL/s in the glass nozzle. The clear plastic nozzle was made with a fifth order polynomial fit to the geometry of the glass nozzle, so that the clear plastic nozzle and glass nozzle 2 have the same geometry. Choked-flow was due to the presence of cavitation in the nozzle and the only difference between the clear plastic nozzle and the glass nozzle was the surface defects.[A1] Choked-flow occurs when sonic conditions are present in the nozzle and as the back pressure decreases the flow rate stays the same. The speed of sound in two-phase flow is lower when compared to single phase flow, and

when cavitation occurs the speed of sound drops in the nozzle, which allowed for sonic condition and choked-flow. The pressure taps and surface roughness features acted as nucleation sites, leading to an earlier occurrence of cavitation and lower flow rates. The maximum single-phase flow rate was 20.92 mL/s at a back pressure of 78.6 kPa and is indicated with a red circle in Figure 4.7. Flow rates above 20.92 mL/s but below 24.48 mL/s were two-phase but not yet in the choked-flow condition.

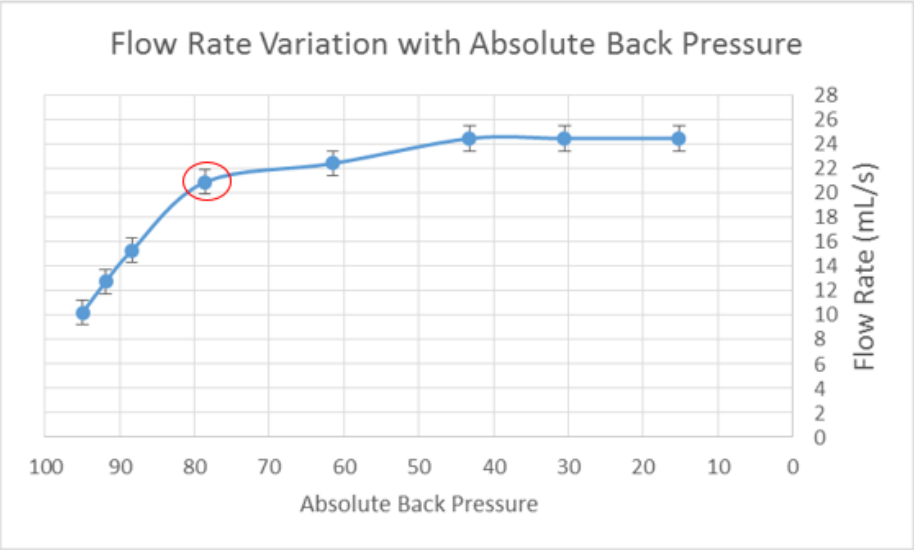

Figure 4.7: Flow rate in the clear plastic nozzle as a function of absolute back pressure

Time Delay in the Pressure Measurements

The pressure results had to account for a settling time in the response of the pressure transducer output. Initial results inaccurately showed higher pressures at the throat of the nozzle (x/L = 0.534), and in the diverging section at locations x/L = 0.767 and x/L = 0.833. These initial results also had large uncertainties when not accounting for the transducer settling time. Figure 4.8 shows results from a steady state experiment with a back pressure of 43.2 kPa that do not account for the transducer response. At the throat and in the diverging section the pressure result is large and has significant uncertainty.

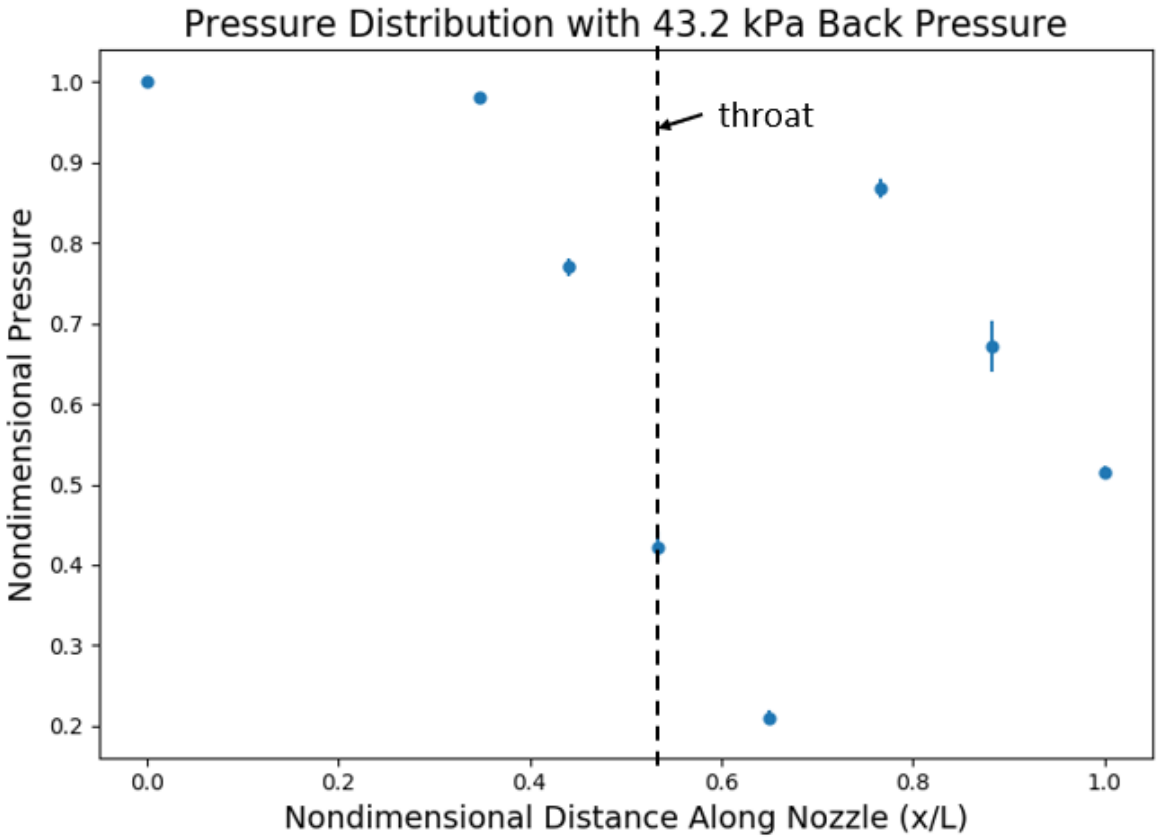

Figure 4.8: Pressure distribution with 43.2 kPa back pressure

In order to ensure the errors in the pressure measurements were due to a time delay in the transducer response, a three-minute-long steady state test was performed. The flow rate through the nozzle was kept constant and data collection was started at the initiation of flow through the blow-down system. The transducer time delay shown in Figure 4.9 was the delay for the sixth pressure transducer (P6), which is at location x/L = 0.767. P6 was a 0-30 psia transducer with a 0-5 volt dc output. The transducer output reached a final voltage after approximately 100 seconds and reached 60% of the final voltage after approximately 30 seconds. Since the transducers were connected to the nozzle through capillary tubed with an inner diameter of 0.006 inches, it was important to check if the time delay response was from the electronic in the pressure transducer or a physical phenomenon in the capillary tubes. This was done by filling the

entire blow down system with water so that it was pressurized above atmospheric pressure. Then after letting the pressure stabilize in the transducers, each transducer was individually disconnected from the blowdown system. This presented a step change in pressure from the filled blow down system to atmospheric and the results for P6 are shown in Figure 4.10. The disconnect process involved unscrewing a Swagelok fitting that had been tightened to create a seal and was done by hand. It took approximately ten seconds to fully disconnect each transducer. The vertical red lines in Figure 4.10 indicate when the disconnect process began and ended.

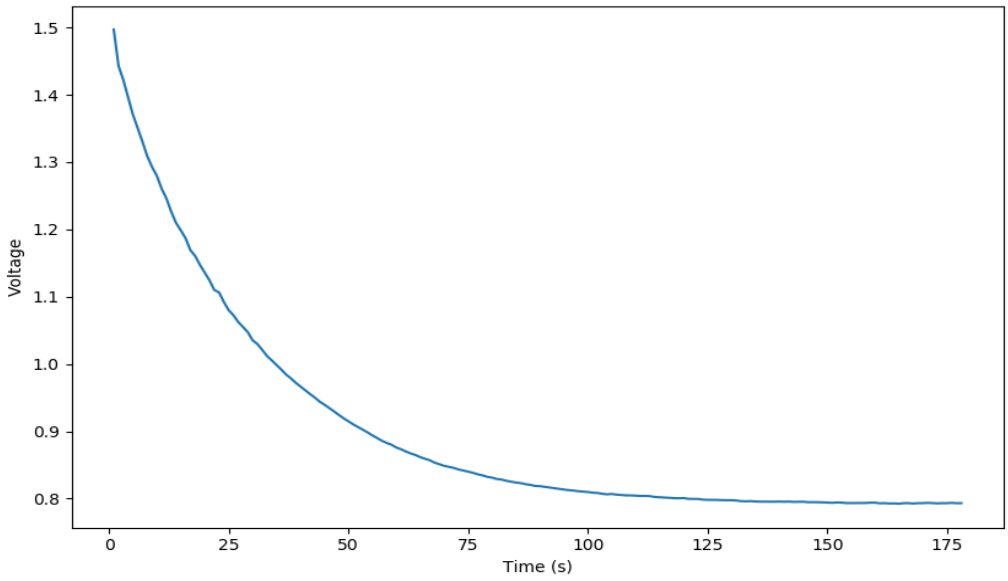

Figure 4.9: Voltage response for pressure transducer 6 during a steady state test

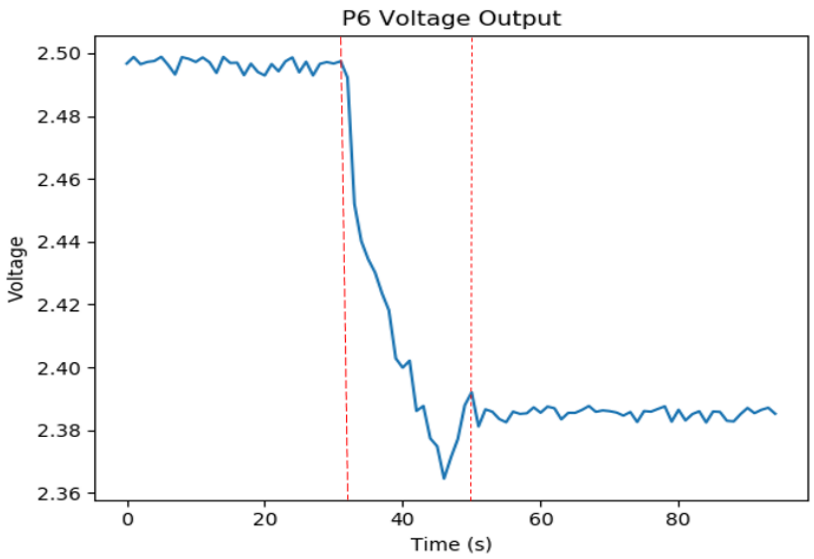

Figure 4.10: Voltage response to a step change for pressure transducer 6

The steady state experiment transducer response exhibited a time delay unassociated with pressure changes in the nozzle. In the disconnect test, the voltage output of the pressure transducers decreased at the same rate that they were disconnected. This meant that the slow transducer response was not due to the electronics of the transducer but instead was from a physical phenomenon in the capillary tubes. To account for this measurement time delay, the steady state experiments were conducted for 30 seconds or more before the start of data collection.

Single-Phase Measurements in the Clear Plastic Nozzle

The single-phase flow data, shown in table 4.3 and figure 4.11, displayed the expected trends for flow in converging-diverging nozzle. The pressure reached a minimum at the throat for each flow rate and as the flow rate increased the throat pressure decreased. Frictional losses in a converging-diverging nozzle depend on the flow velocity. As the flow rate through the nozzle increased the final outlet pressure decreased due to higher frictional losses. The data follows expected physical trends. Table 4.2 also shows the numerical mean, the first number listed, of three tests done at each flow rate. The pressure measurements for each test are listed

below the mean for each location and flow rate. Figure 4.9 shows a plot of the pressure nondimensionalized with the inlet pressure, P/P_{inlet}, as a function of nondimensional length in the nozzle, x/L with L being the total length of the region of pressure measurement in the nozzle, 42.88 mm. The small uncertainty bars shown in the plot represent the precision error in the nondimensional pressure measurements. The single-phase measurements show that the pressure transducers and flow measurements produced accurate results.

Table 4.3: Single-phase flow pressure data

Location	**10.7 mL/s Pressure in kPa**	**12.8 mL/s Pressure in kPa**	**15.3 mL/s Pressure in kPa**	**20.9 mL/s Pressure in kPa**
0	101.2 (mean) 101.1, 101.2, 101.2	101.0 (mean) 101.1, 101.0, 101.0	100.9 (mean) 100.8, 100.8, 100.9	100.9 (mean) 101.4, 100.6, 100.7
0.347	100.6 (mean) 100.6, 100.6, 100.6	100.3 (mean) 100.2, 100.3, 100.3	99.9 (mean) 99.9, 99.8, 100.1	97.3 (mean) 97.2, 97.3, 97.3
0.440	95.6 (mean) 95.2, 95.8, 95.7	93.2 (mean) 93.0, 93.2, 93.3	89.8 (mean) 89.7, 89.3, 90.3	85.4 (mean) 85.8, 85.5, 84.8
0.534	82.3 (mean) 81.3, 83.1, 82.5	74.2 (mean) 74.8, 74.2, 74.8	62.8 (mean) 62.1, 61.9, 64.4	48.6 (mean) 39.8, 49.0, 48.2
0.650	88.0 (mean) 87.9, 88.3, 87.8	82.1 (mean) 81.3, 82.1, 82.3	74.2 (mean) 73.4, 74.0, 75.1	50.3 (mean) 52.0, 49.4, 49.5
0.767	90.9 (mean) 90.5, 91.3, 91.0	86.7 (mean) 86.2, 86.7, 86.8	82.7 (mean) 80.4, 80.1, 81.5	65.2 (mean) 63.5, 66.4, 65.7
0.883	94.2 (mean) 93.8, 94.5, 94.3	91.3 (mean) 90.9, 91.3, 91.3	87.4 (mean) 87.1, 87.5, 87.7	78.3 (mean) 79.6, 78.2, 77.0
1	94.7 (mean) 94.6, 94.9, 94.7	91.9 (mean) 91.6, 91.9, 92.1	88.0 (mean) 87.6, 87.8, 88.5	75.3 (mean) 76.2, 74.7, 75.0

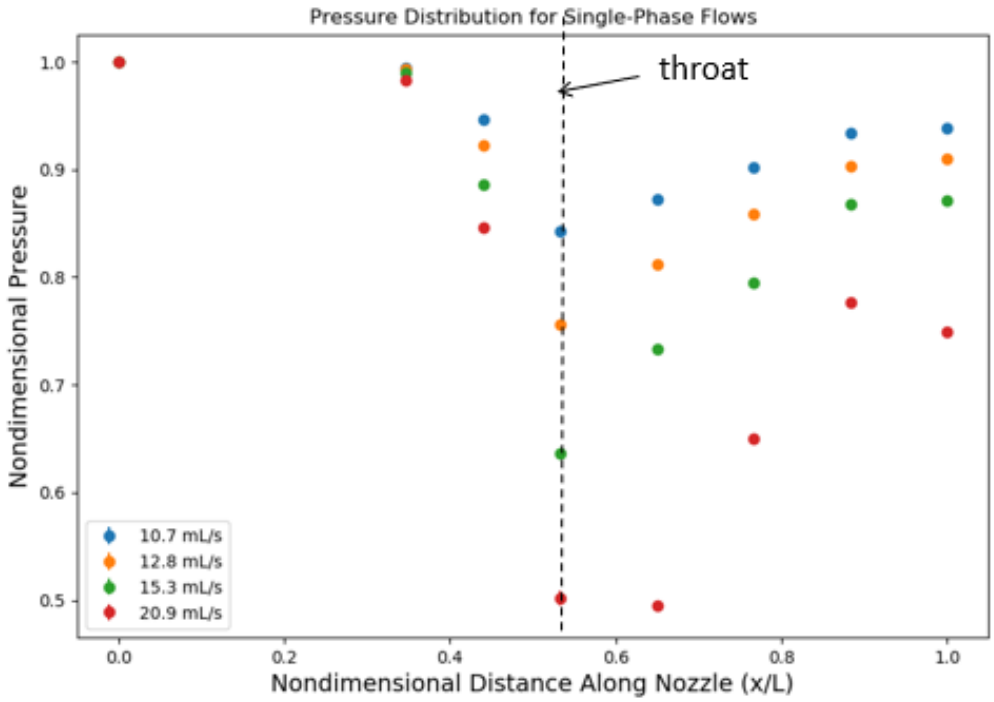

Figure 4.11: Single-phase pressure distribution for various flows in clear plastic nozzle

The friction in the nozzle can be quantified with a relative roughness value for single-phase flow. This value was fit to the nozzle by an iterative process of calculating the throat pressure at each of the single-phase flow rates using Bernoulli's principle with friction included. The 1D pressure distribution was estimated with the following equation:

$$\mathbf{P_z = P_i - \frac{1}{2}\rho * \left(\frac{Q^2}{\pi R_t^2} - \frac{Q^2}{\pi R_z^2}\right) - \rho g z - \Delta P_f} \qquad \mathbf{(4.2)}$$

Equation 4.2 was an approximate mechanical energy balance between the inlet of the nozzle denoted by *i* and any location z. Q was the measured flow rate and R was the radius of the nozzle at the denoted location. The third term represents the energy lost due to gravity as the flow moves a distance *z* up the nozzle. The fourth term represents the pressure loss due to friction, which was estimated by integrating the pressure gradient from Equation 4.3.

$$\mathbf{\frac{dP}{dz} = \frac{1}{2}\rho v_z^2 \frac{f}{D_z}} \qquad \mathbf{(4.3)}$$

For laminar flows, which includes the measured flow rates of 10.7 mL/s, 12.8 mL/s, and 15.3mL/s, the friction factor *f* does not depend on the surface roughness and is calculated by 64/Re. The friction factor for turbulent flow was found using an equation developed by Haaland in 1983. This is shown as Equation 4.4 and gives the friction factor as a function of the relative roughness (ε/D) and Reynolds number.

$$\frac{1}{\sqrt{f_z}} = -1.8\log\left[\left(\frac{\varepsilon/D_z}{3.7}\right)^{1.11} + \frac{6.9}{Re_z}\right] \quad (4.4)$$

The parameter ε was varied to find the correct friction factor so that Equation 4.2 properly predicted the pressure distribution for single phase flow (Hibbeler, 2015). Figure 4.12 shows the comparison of the measured data and the calculated pressure distribution using a roughness factor of ε = 0.10 mm. The calculated distribution has good agreement with the measured pressure and has the best fit at the throat of the nozzle. The fit in diverging section is not as accurate because it does not account for any separation or Vena-contracta effects. The fit shows that the surface roughness can be characterized by the roughness parameter ε=0.10 mm, which is used in the relative roughness. The roughness parameter is on the same order of size as the pressure tape bore holes which are 0.006 inches or 0.1524 mm.

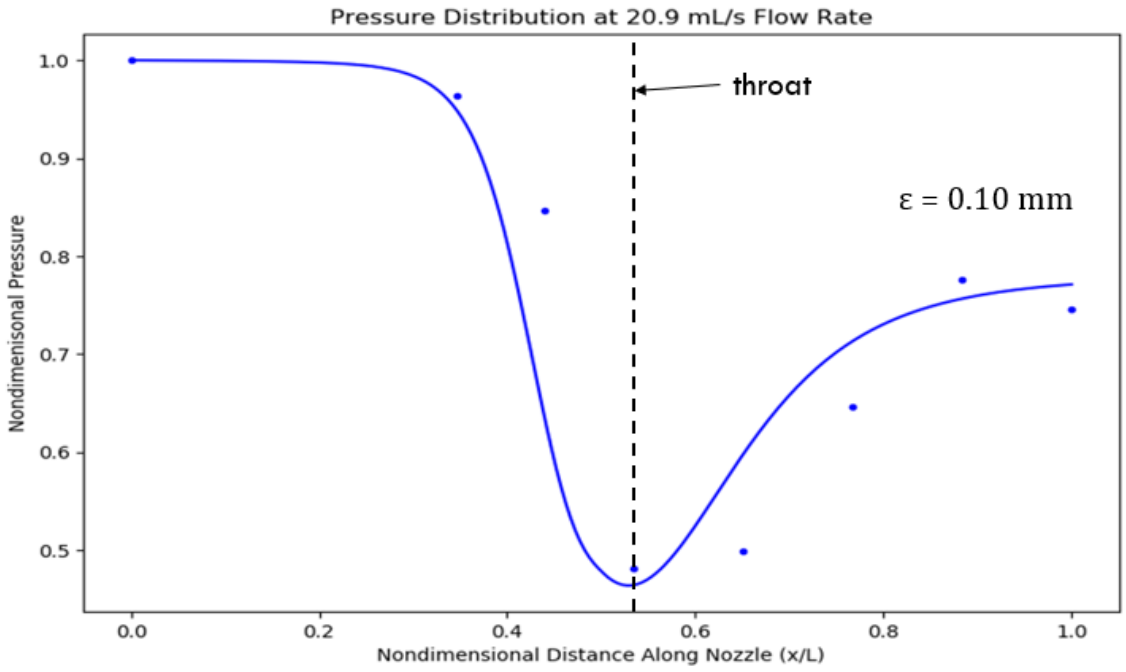

Figure 4.12: Pressure measurement and theory calculation comparison for single-phase turbulent flow

Pressure Measurements and Flow Visualization of Steady-State Two-Phase Flows

The pressure distribution during two-phase flows was examined to see how cavitation affected the pressure in the nozzle. Pressure and flow measurements were taken at back pressures of 43.2 kPa, 30.5 kPa, and 15.17 kPa absolute pressure. These measurements were used to calculate the cavitation number at the throat for each back pressure. The high-speed camera was used to capture images of the two-phase flow during the steady state cavitation. The images were used to study flow parameters and measure the length of the two-phase region in the diverging section of the nozzle. Figure 4.13 shows the pressure distribution in the nozzle for the 43.2 kPa back pressure test. The lowest pressure occurred downstream of the throat for this test indicating the Vena-contracta effect occurred in the nozzle. The pressure in the diverging section for this

test is less than half of the inlet pressure indicating significant frictional losses in the two-phase region.

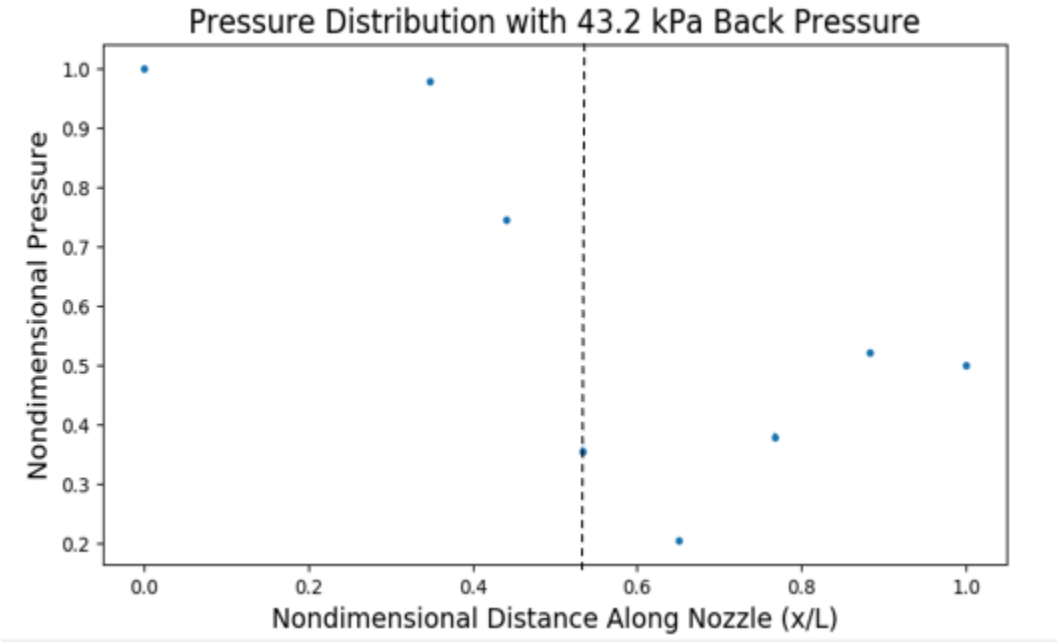

Figure 4.13: Nondimensional pressure distribution in nozzle for test with 43.2 kPa absolute back pressure

Figure 4.14 shows the cavitation initiated at the throat along the side of the nozzle with the pressure taps. This indicates that the pressure bore hole at the throat acts as a nucleation site for cavitation. The two-phase region then stayed on the side of the nozzle with the pressure taps and does not separate from the wall of the nozzle. The white dashed lines in the image indicate the bounds on the two-phase region in the nozzle.

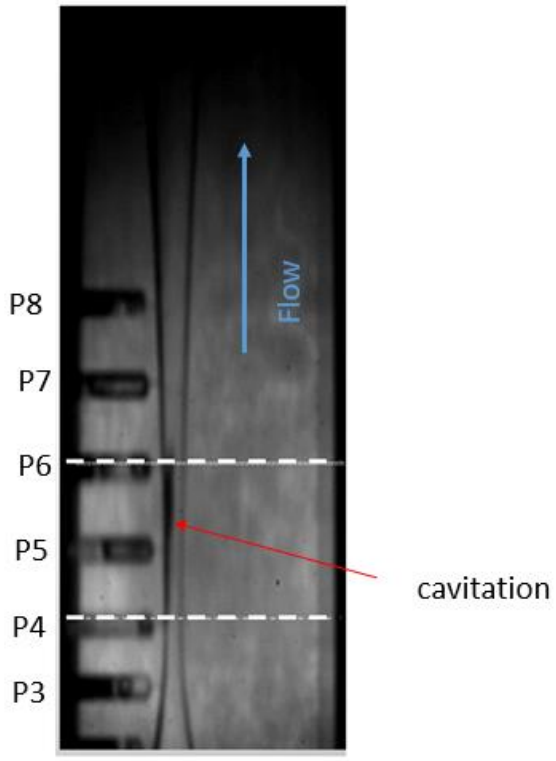

Figure 4.14: Image of two-phase flow in transparent nozzle during 43.2 kPa absolute back pressure test

The 30.5 kPa absolute back pressure test also exhibited the Vena-contracta effect. The smallest pressure was recorded downstream of the throat. In the diverging section the pressure quickly reaches the back pressure and then stabilizes. This means there is very little pressure recovery in the diverging section likely due to separation effects. Figure 4.15 shows the pressure distribution in the nozzle at this back pressure. The separation effects can be seen in Figure 4.16 along the side of the nozzle with the pressure transducers as clear space near the wall. The separation increase as the flow moves through the nozzle until the condensation point where it is no longer visible due to the flow returning to single-phase. The white lines indicate the cavitation front and where condensation occurs.

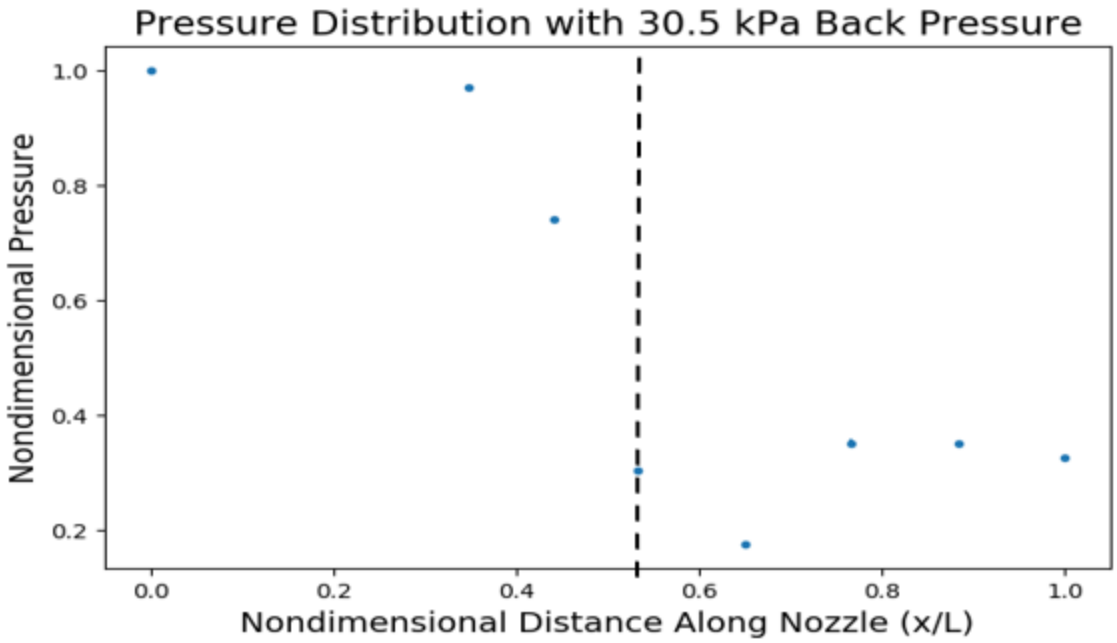

Figure 4.15: Nondimensional pressure distribution for test with 30.5 kPa absolute back pressure

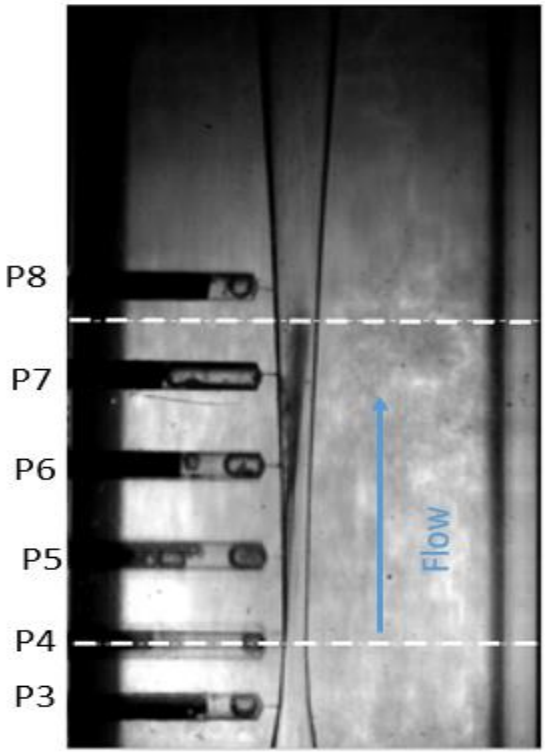

Figure 4.16: Image of two-phase flow in transparent nozzle during 30.5 kPa absolute back pressure test

The 15.17 kPa absolute back pressure test exhibited a minimum pressure just downstream of the throat and a decrease in pressure in the diverging section of the nozzle. The minimum pressure occurring downstream of the throat can be explained by the Vena-contracta effect, which was seen in the 43.2 kPa and 30.5 kPa absolute back pressure tests as well. The pressure decrease in the diverging section was due to separation effects as the flow approached the downstream reservoir. The back pressure in the reservoir is lower than the final measured pressure in the diverging section, which was 21.2 kPa. The increase in separation and resulting decrease in pressure in the diverging section were a result of the lower back pressure. The separation effect is shown in figure 4.17 as clear space along the side of the nozzle with the pressure taps. The tests with higher back pressures showed the flow staying attached to the wall of the nozzle with the pressure taps. This attached flow existed mostly in the two-phase region in the 43.2 kPa and 30.5 kPa back pressure results. However, the two-phase flow detaches from the wall of the nozzle much earlier in the 15.17 kPa back pressure tests and results in a pressure decrease in the diverging section. The pressure measurement results for each back pressure are displayed in table 4.3. The results were taken from the mean of three repeated tests at each back pressure. Table 4.3 shows the mean results and the results from each repeated test.

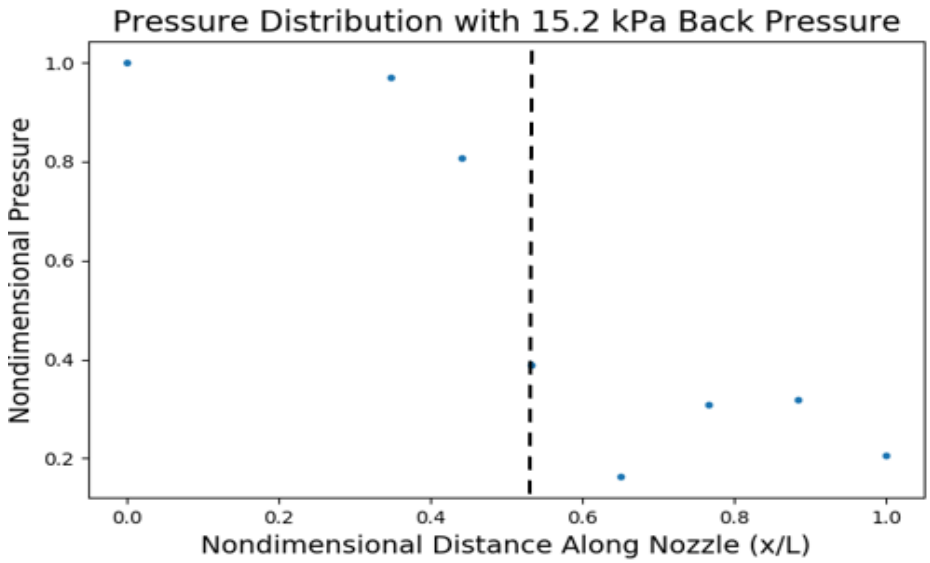

Figure 4.17: Nondimensional pressure distribution from 15.17 kPa absolute back pressure test

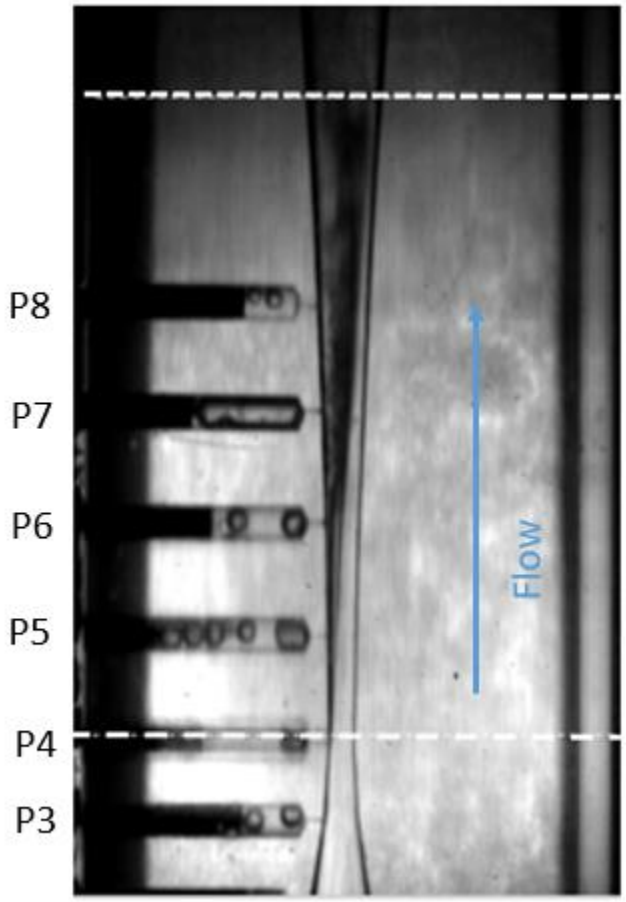

Figure 4.18: Image of two-phase flow in transparent nozzle during 15.17 kPa absolute back pressure test

Table 4.4: Two-phase flow pressure data for each steady-state test in the clear plastic nozzle

Location	43.2 kPa Back Pressure	30.5 kPa Back Pressure	15.17 kPa Back Pressure
0	99.4 (mean)	102.7 (mean)	103.4 (mean)
	99.3, 99.4, 99.5	102.0, 103.0, 103.0	103.4, 103.4, 103.3
0.347	97.5 (mean)	100.0 (mean)	100.1 (mean)
	97.6, 97.3, 97.6	100.0, 100.0, 100.0	100.1, 100.2, 100.1
0.440	74.3 (mean)	76.2 (mean)	81.9 (mean)
	74.4, 74.1, 74.4	76.0, 76.2, 76.5	79.0, 83.4, 83.3
0.534	33.2 (mean)	31.3 (mean)	39.9 (mean)
	34.8, 33.2, 31.6	32.8, 30.6, 30.9	38.4, 41.4, 39.9
0.650	20.4 (mean)	18.9 (mean)	17.1 (mean)
	19.3, 20.5, 21.4	21.1, 17.5, 18.2	17.2, 16.9, 17.2
0.767	39.2 (mean)	35.5 (mean)	30.9 (mean)
	41.9, 38.1, 37.7	35.5, 34.9, 36.3	29.8, 32.0, 31.0
0.883	51.9 (mean)	35.1 (mean)	34.3 (mean)
	52.3, 52.5, 50.8	34.9, 34.1, 36.2	37.3, 33.1, 32.4
1	50.1 (mean)	33.6 (mean)	21.2 (mean)
	50.7, 49.8, 49.7	34.8, 32.4, 33.7	21.3, 21.2, 21.1

The velocity and cavitation number at the throat and just downstream of the throat, x/L = 0.650, were calculated and are shown in Table 4.4. The velocity was found by dividing the measured volumetric flow rate by the cross-sectional area of the nozzle at the location of interest. This method does not account for the Vena-contracta effect because the actual cross-sectional area of the flow is difficult to predict. The cavitation number was calculated using Equation 1.1, which depends on velocity. Downstream of the throat the calculated velocity was smaller than the velocity associated with the Vena-contracta effect, resulting in a larger calculated cavitation number. Despite this, the calculated cavitation number at x/L = 0.650 was smaller than the

cavitation number at the throat for cavitating flows. This corresponds to the larger cross-sectional area of two-phase flow downstream of the throat as shown in Figures 4.13, 4.15, and 4.17. The data from the 75.3 kPa absolute back pressure test corresponds to the maximum single-phase flow-rate through the nozzle. This means that cavitation occurs at cavitation numbers below 1.043, which is the throat cavitation number for the maximum single-phase flow. The downstream cavitation number decreased with decreasing back pressure because of decreasing pressures in the nozzle. This contributes to the longer two-phase regions seen in the lower back pressure tests.

Table 4.5: Throat and Downstream (x/L = 0.650) flow parameters in the clear plastic nozzle

Back Pressure (kPa)	Throat Velocity (m/s)	Throat Cavitation Number	Downstream Velocity (m/s)	Downstream Cavitation Number
75.3	9.429	1.043	7.860	1.55
43.2	11.044	0.509	8.919	0.458
30.5	11.044	0.477	8.919	0.420
15.17	11.044	0.619	8.919	0.374

Length of the two-phase region

The length of the two-phase region was measured using the high-speed camera flow visualization (frame rate of 1000 fps). The pressure taps bore holes downstream of the throat are evenly spaced at 5 mm apart (Figure 2.4) and were then used as a scale on the image to measure the length of the two-phase region. The beginning of the region was defined as the nucleation point, labelled position 1, which occurs at the pressure tap at the throat of the nozzle for each back pressure. The two-phase region ends at the condensation shock, labelled position 2, in the diverging section of the nozzle. This location is not as easily defined, and uncertainty bounds

were placed around the shock position and are labelled position 3 and 4. Figure 4.18 displays the measurement process with the measurements included for the 15.17 kPa back pressure test.

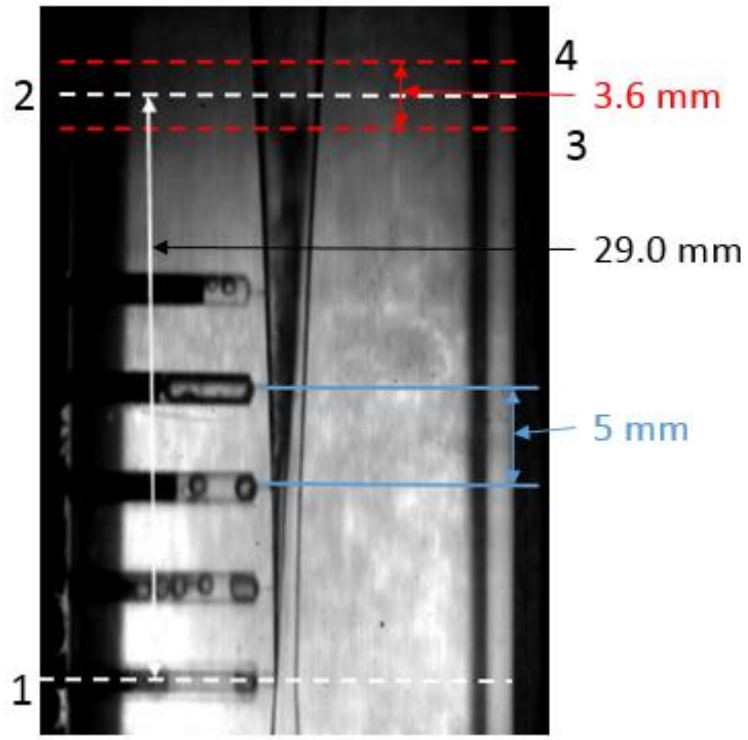

Figure 4.19: Measurement of the length of the two-phase region in the 15.17 kPa back pressure test

The length of the two-phase region is related to the cooling potential of the cavitation and is a function of back pressure. Lower back pressures resulted in longer two-phase regions, even though the flow rate through the nozzle did not increase. Lower back pressures resulted in lower pressures and cavitation numbers in the diverging section of the nozzle (Table 4.3 and Table 4.4), thus delaying condensation in the diverging section. Figure 4.19 shows the length of the two-phase region as a function of back pressure, where the uncertainty bars arise from the uncertainty in the condensation shock location.

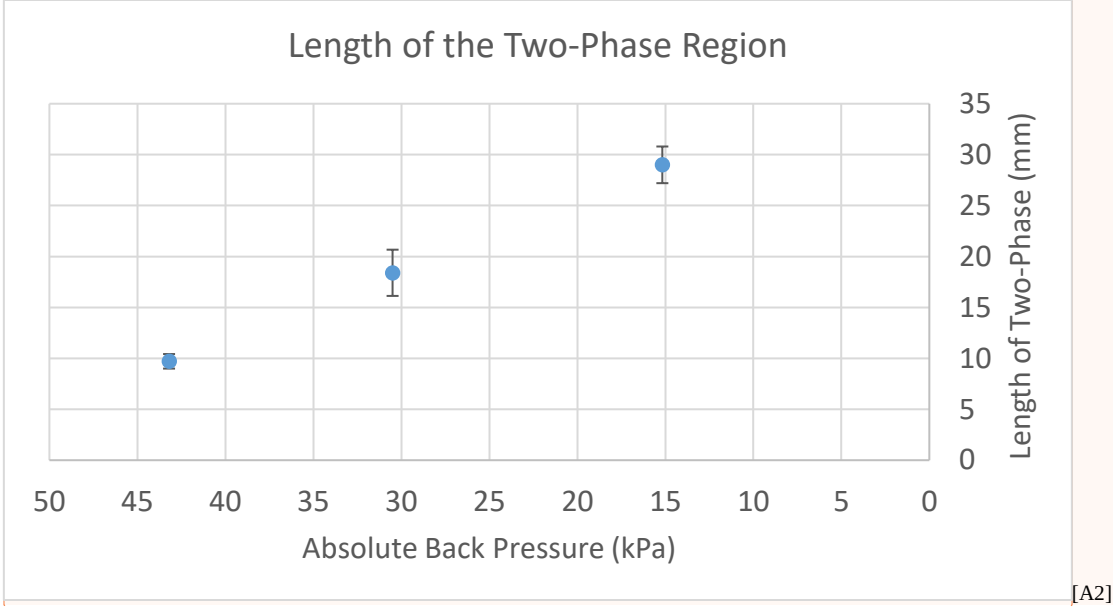

[A2]

Figure 4.20: Length of the two-phase region as a function of absolute back pressure

Steady-state tests conclusion

The steady-state flow results included pressure and flow measurements for single and two-phase flows through the nozzle. The pressure response was found to have a settling time that could be accounted for by waiting 30 to 60 seconds to start data collection in each experiment. A roughness parameter of ε=0.10 mm was fitted to the nozzle using the turbulent single-phase flow data. This parameter characterizes the surface defects and roughness in the nozzle that contribute to frictional losses and can act as nucleation sites for cavitation. The maximum single-phase flow rate through the clear plastic nozzle was found to be 20.9 mL/s and above this flow rate cavitation initiated at throat of the nozzle. Cavitation initiation consistently occurred at the bore hole for the throat pressure tap, which suggested that the bore hole acted as a nucleation site. The minimum measured pressure occurred at pressure tap just downstream of the throat for all the two-phase flows. The calculated cavitation number was also smaller at the point of minimum pressure. This indicated the possibility of the Vena-contracta effect occurring the nozzle for two-

phase flows. Also, lower back pressures resulted in greater flow separation in the diverging section of nozzle. Initially the cavitation flow attached to the wall of the nozzle but then separated in the diverging section. At the lowest back pressure tested this separation can be seen in the pressure measurements where the final pressure tap showed a decrease in pressure at the exit of the diverging section. Lastly, the length of the two-phase region was measure for each back pressure and increased with decreasing back pressure.

Transient Test Results

The transient tests were done to analyze the metastable behavior in the 3D printed nozzle. As seen in the glass nozzle, the metastable behavior occurred when the flow rate through the nozzle reached a peak and then dropped back down to the choked-flow condition (Figure 4.2). The goal of the transient test was to monitor the pressure response in the nozzle during the metastable behavior. As discussed in the Steady State Results section, the pressure measurements featured a time delay and this time delay response was fitted with an exponential fit. The exponential fit was used in an algorithm to correct the pressure transducer output so that the pressure measurements more accurately displayed the changing pressure in the nozzle during a transient test. High-speed camera footage was used to visualize the flow during the transient test. This flow visualization was used to characterize nucleation sites and the growth of the two-phase region. The choked flow rate through the clear 3D printed nozzle was 6.5 mL/s less than the flow rate through the glass nozzle at the same conditions, which appeared to result in less metastability. The results were used to analyze the metastability and understand cavitation initiation.

The response of each pressure transducer was fitted with an exponential curve with the form of Equation 4.5, where P_i was the initial pressure transducer output in kPa, P_f was the final

pressure transducer output in kPa, P_o was the transient pressure transducer output in kPa, τ was the time constant in seconds, and t was time in seconds.

$$\mathbf{P_o = P_f - (P_f - P_i) * e^{-t/\tau}} \quad \textbf{(4.5)}$$

The exponential fit was created by plotting the ln(θ) v time, where θ is described in Equation 4.6.

$$\boldsymbol{\theta = \frac{P_f - P_o}{P_f - P_i}} \quad \textbf{(4.6)}$$

The data plotted was generated using a steady state test with a back pressure of 31.7 kPa. This test was done three times according to the procedure outlined in the Transient Measurements section of Chapter 3, and data was collected for a total of three minutes so that the settled pressure output was captured. The settled pressure was assumed to be that actual pressure in the nozzle. The data from the three tests was averaged and the exponential fit was applied to the mean data. A linear regression was then fitted to the data in which the slope of that regression was $-1/\tau$. This was done for each transducer to solve for the time constant τ during two-phase flow in the nozzle. Figure 4.21-4.28 shows the ln(θ) v time plots for each pressure transducer with the linear regression and time constant on the plot. Table 4.6 gives the location of each pressure transducer in the nozzle.

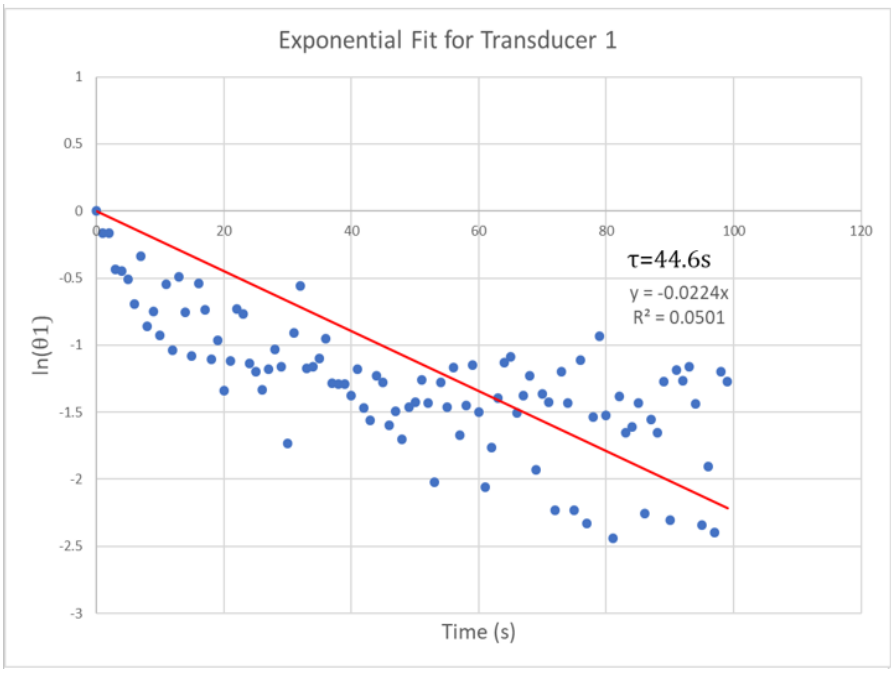

Figure 4.21: Exponential fit plot for transducer 1 (P1)

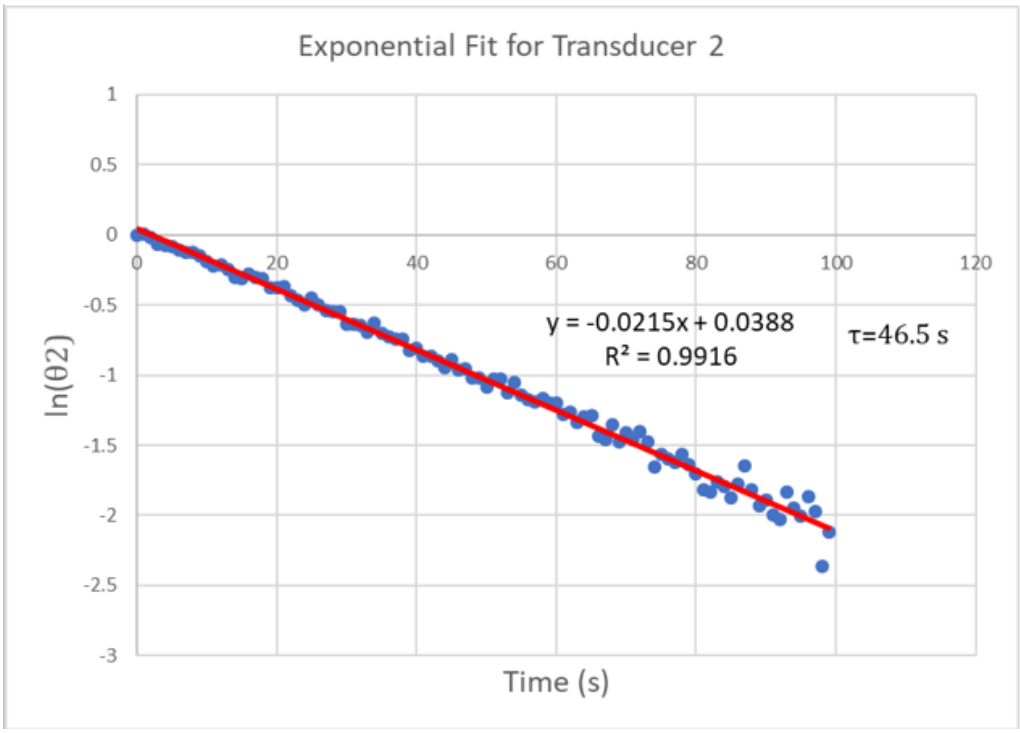

Figure 4.22: Exponential fit plot for transducer 2 (P2)

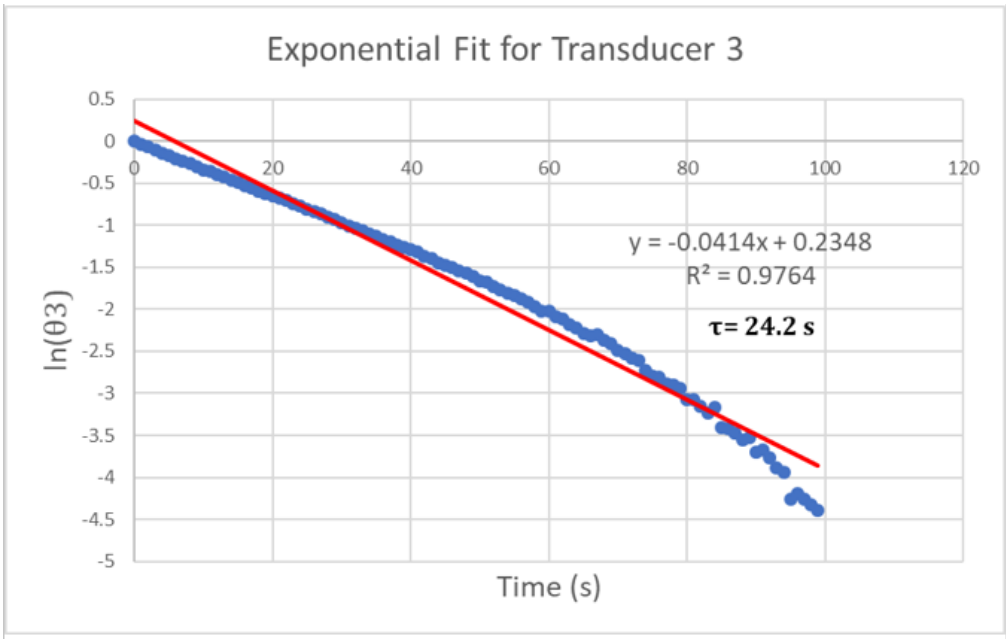

Figure 4.23: Exponential fit plot for transducer 3 (P3)

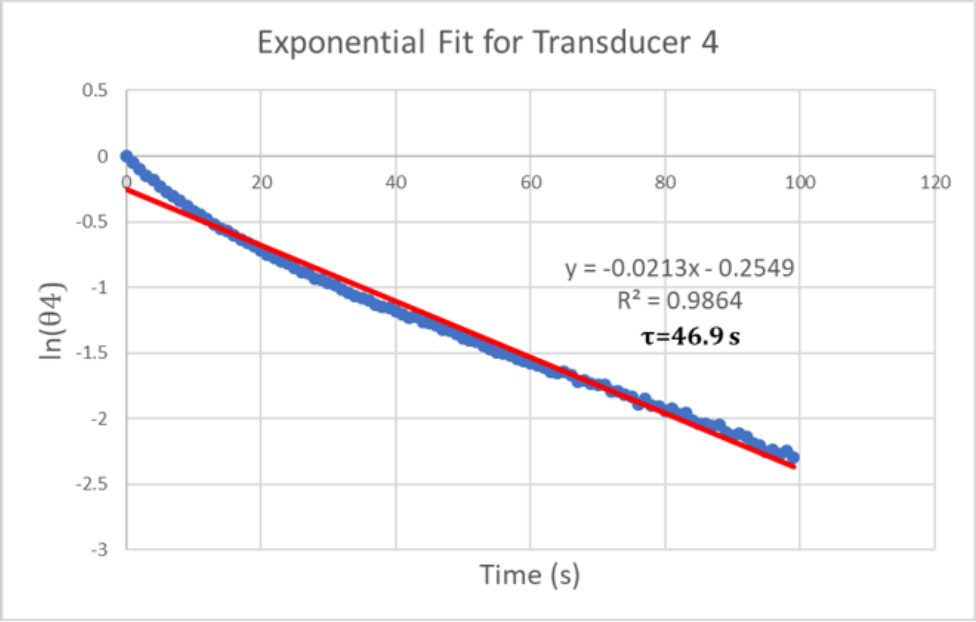

Figure 4.24: Exponential fit plot for transducer 4 (P4)

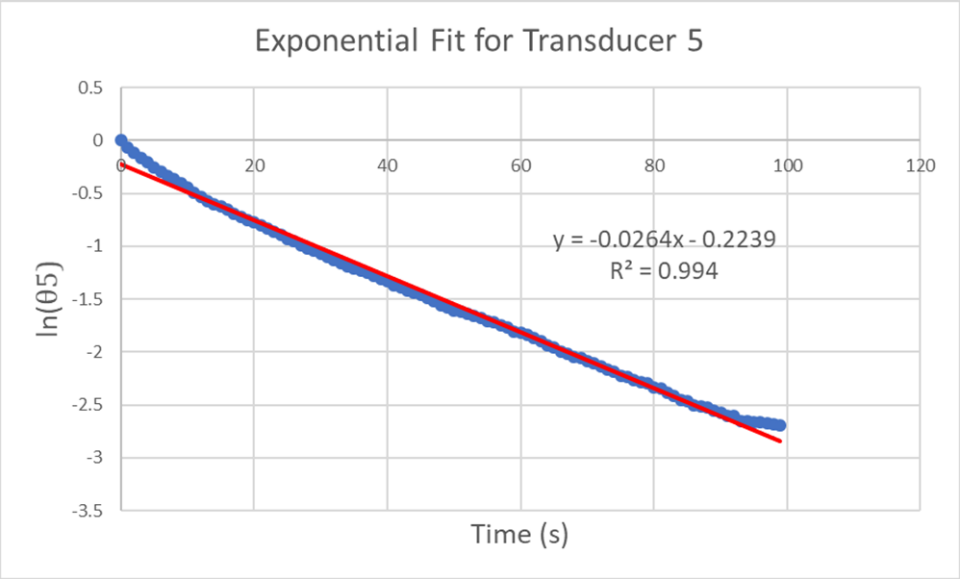

Figure 4.25: Exponential fit plot for transducer 5 (P5)

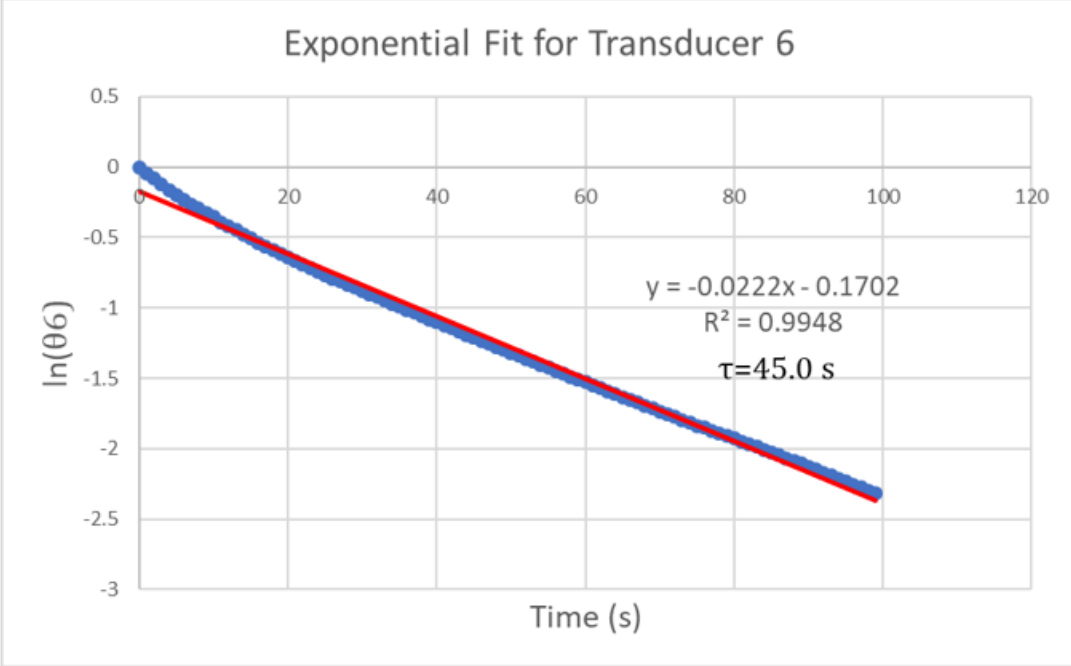

Figure 4.26: Exponential fit plot for transducer 6 (P6)

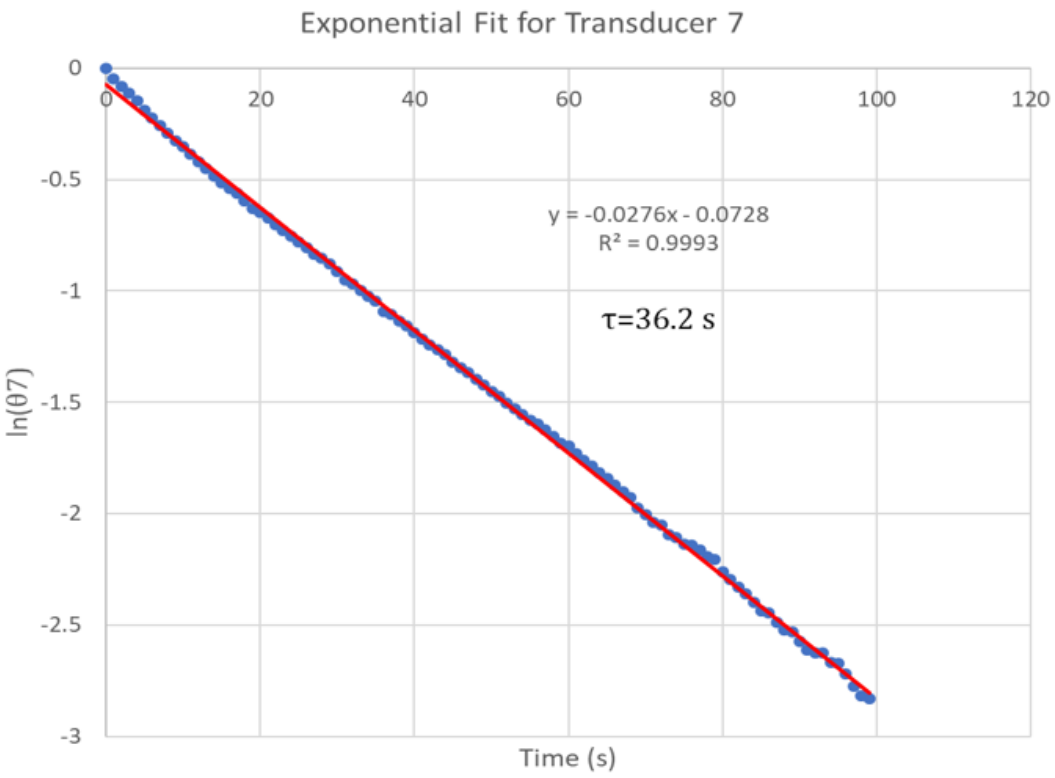

Figure 4.27: Exponential fit plot for transducer 7 (P7)

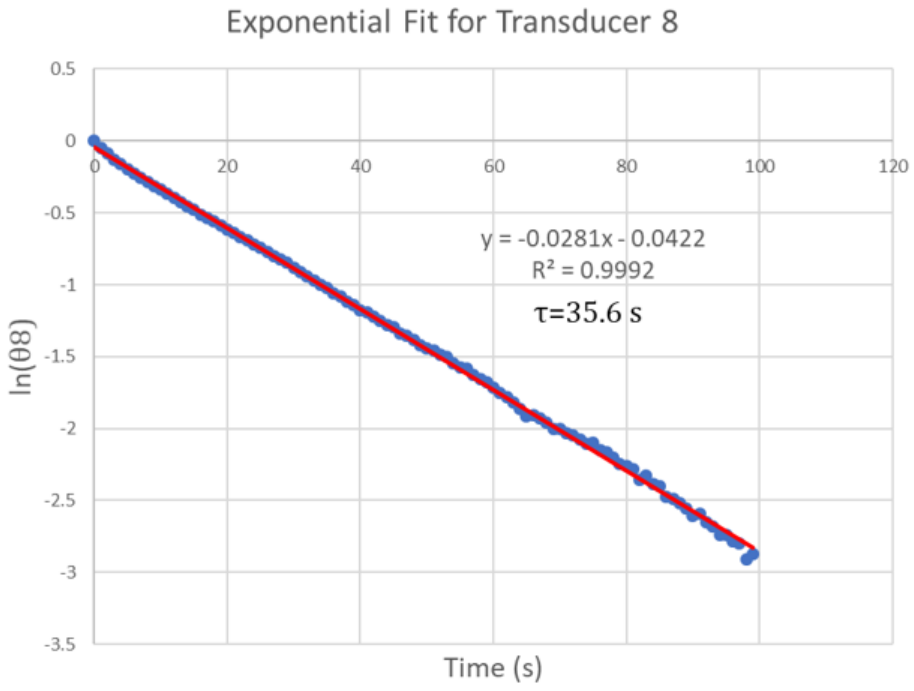

Figure 4.28: Exponential fit plot for transducer 8 (P8)

Table 4.6: Pressure transducer location

Relative Location (x/L)	Pressure Transducer
0.0	P1
0.347	P2
0.440	P3
0.534	P4
0.650	P5
0.767	P6
0.833	P7
1.0	P8

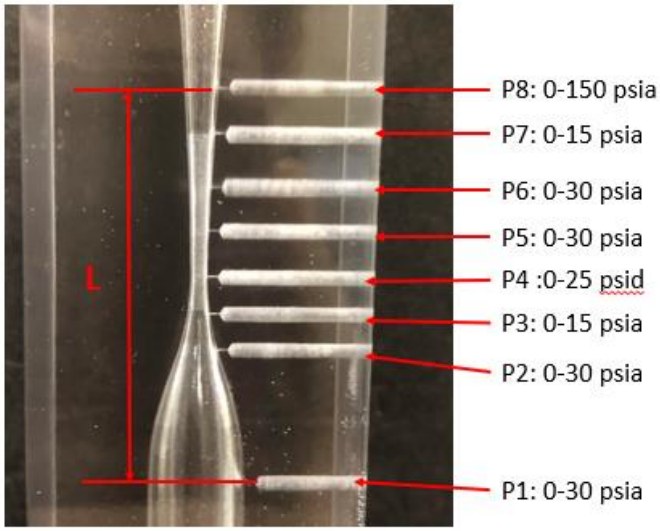

The time constant found from the exponential fit was used in a first order algorithm to correct for the delayed pressure transducer output in the transient tests. The derivation of the first order algorithm in shown in Appendix A. Equation 4.7 shows the algorithm with P_c as the corrected pressure, P_o as the pressure transducer output, and τ as the time constant calculated from the exponential fit. $\frac{dP_o}{dt}$ is the slope of the output pressure data at a point of interest. This slope was found with a polynomial or exponential curve fit to the data. The curve fit used depended on the accuracy of the fit and how well the fit predicted the slope at the point of interest. Separate curve fits were often used in a single set of data to achieve the most accurate prediction of the slope.

$$\mathbf{P_c = P_o + \tau * \frac{dP_o}{dt}} \qquad \mathbf{(4.7)}$$

The accuracy of this algorithm was tested by applying a theoretical pressure to the exponential fit of the pressure transducers' outputs. This theoretical pressure was matched to the settled pressure from the three-minute-long steady state experiment so that the exponential fit could be compared to the data concurrently. The theoretical pressure output was then put into the algorithm as P_o

and the algorithm then generated the correct pressure that matched the final settled pressure for each pressure transducer. This algorithm test is plotted for transducer 8 in Figure 4.28, where the orange points labelled P8 fit are the theoretical pressure output from the exponential fit and the grey points labelled P8 actual are the corrected pressure data[A3]. The actual pressure input was a step change with the pressure at $t = 0^+$ being equal to the final settled pressure. The corrected pressure matched the actual pressure.

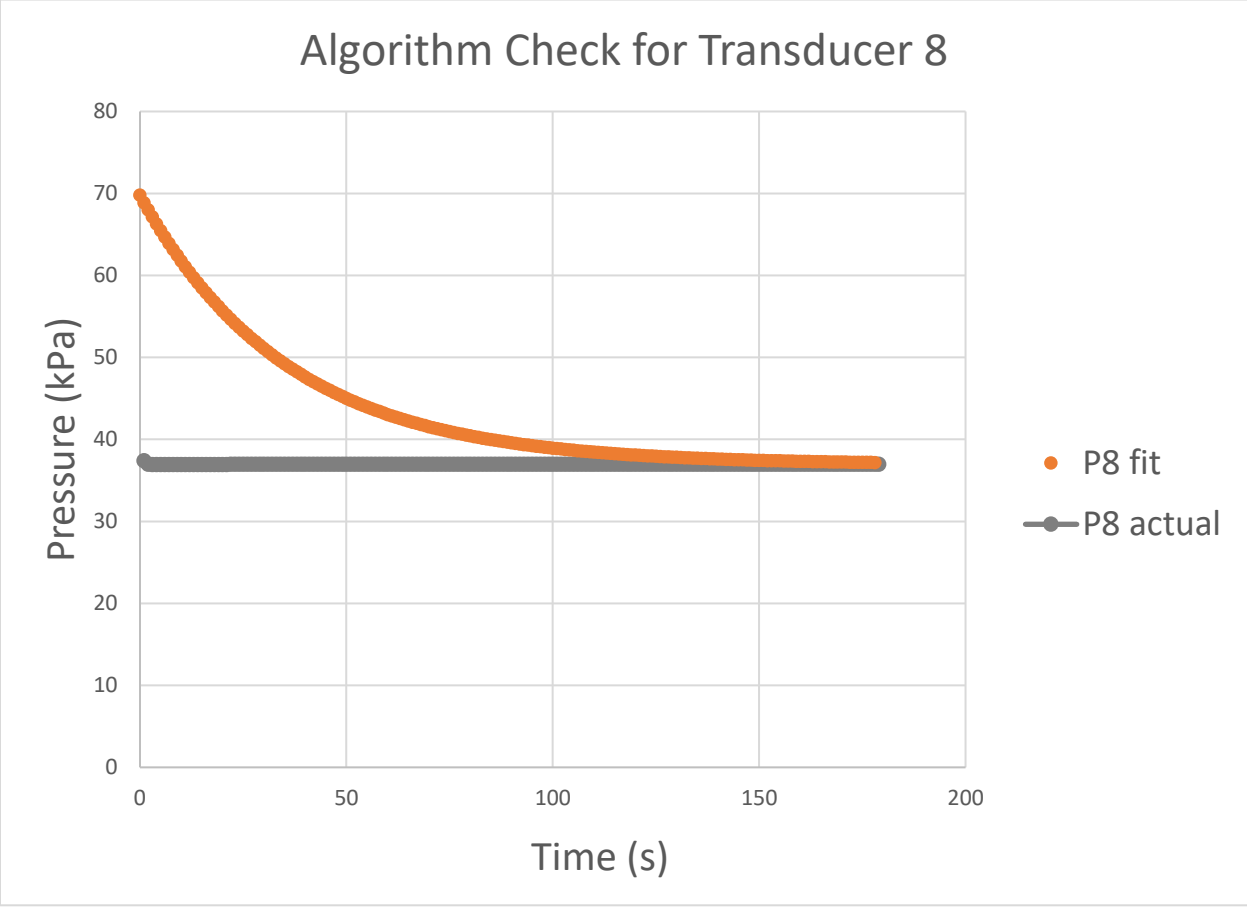

Figure 4.29: Algorithm results for transducer 8

The time constant, τ, depended on the phase of the fluid in the nozzle and in the connecting tubes. The same exponential fit used to find the time constant during two-phase flow was applied to data collected for 3-minute-long single-phase steady state tests. Single-phase time constants were found to be significantly less in the diverging-section of the nozzle. The single-phase time constants for transducers 2 and 3 were similar to the two-phase time constants because the flow is always single phase in the converging section of the nozzle. The measured change in pressure during a 3-minute long steady-state test by transducer P1 was only approximately 2.0 kPa and thus the scatter in the data was large in comparison to the change in pressure experienced by transducer P1. This lead to inaccuracies in the time constant calculations for transducer P1 and may have been the reason for the large difference in time-constants for transducer P1 during single- and two- phase flow in the clear nozzle. Table 4.7 shows the time constants for single and two-phase flows.

Table 4.7: Time constants for single and two-phase flows

Pressure Transducer	Time Constant for Two-phase Flow (s)	Time Constant for Single-Phase Flow(s)
P1	45±31	8±4
P2	47±18	34±7
P3	24±10	19±6
P4	47±13	7±2
P5	38±6	5±7
P6	45±6	11±3
P7	38±2	7±1
P8	36±3	8±6

During the transient tests single-phase liquid flow existed in the nozzle until the time at which cavitation initiated. This was important to consider when correcting the pressure output

for the time delay as before cavitation the pressure output responded according the single-phase time constant and after cavitation initiation the pressure output responded according to the two-phase time constant. The flow visualization captured during the transient tests was used to determine when and where cavitation existed in the nozzle. When the flow was single-phase the singe-phase time constant was used in Equation 4.7 to correct the pressure data and likewise the two-phase time constant was used in Equation 4.7 to correct the pressure data when the flow was two-phase. The slope of each pressure transducer output, dP_O/dt, was calculated using polynomial and exponential curve fits. This slope was then used in Equation 4.7 to correct the pressure transducer output. Also, the data correction included the use of the single-phase time constant when the flow at the pressure transducer of interest was single-phase.

Three types of transient tests were performed, a fast valve open rate, a slow valve open rate, and an increase upstream pressure test. Each test was done with an absolute back pressure of 31.9 kPa, at a temperature of 20 °C, and according to the procedure outline in chapter 3. The fast-open and slow-open tests were done to compare how the transient pressure responded to the rate of flow rate increase. The increased upstream pressure tests were done to increase the flow rate through the nozzle by increasing the height of the upstream reservoir and thus increase the nozzle inlet pressure and flow rate through the system. The fast-open test exhibited a max flow rate of 24.70 mL/s and a steady-state flow rate of 24.65 mL/s. Little to no indication of metastable behavior was seen in this flow response. The flow rate during the fast-open transient test is shown in Figure 4.30. The high-speed camera footage, 2000 frames per second, of the fast-open test showed that cavitation initiated at the throat, location of P4, and that initiation occurred 1.8920 seconds into the test. The two-phase region reached full length 2.4090 seconds into the test. This meant that the single-phase time constant was used until two seconds into the test and

then the two-phase time constant was used to correct the data after two seconds. Figure 4.31 shows the flow visualization during the fast-open test.

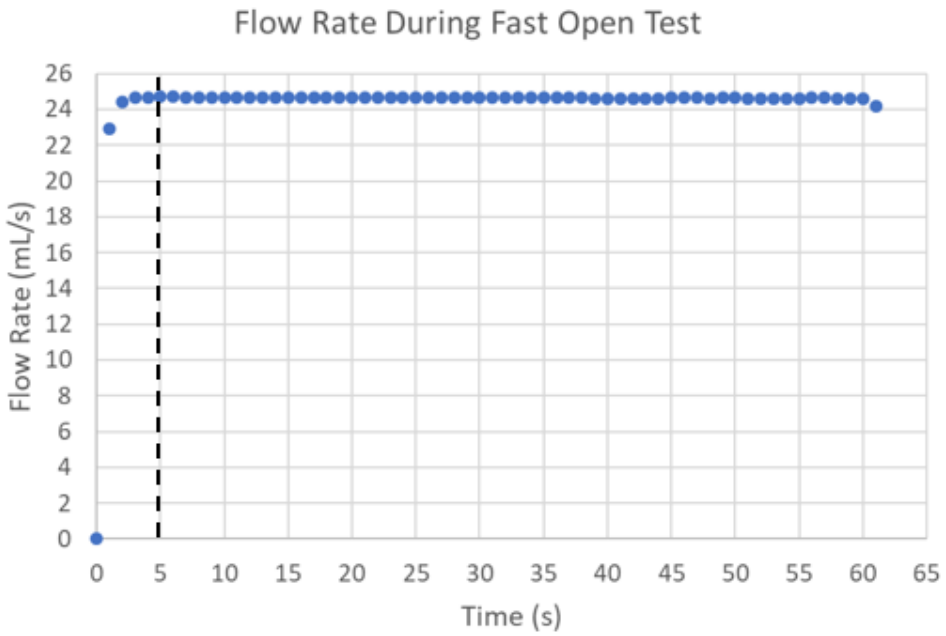

s

Figure 4.30: Flow rate during fast-open transient test

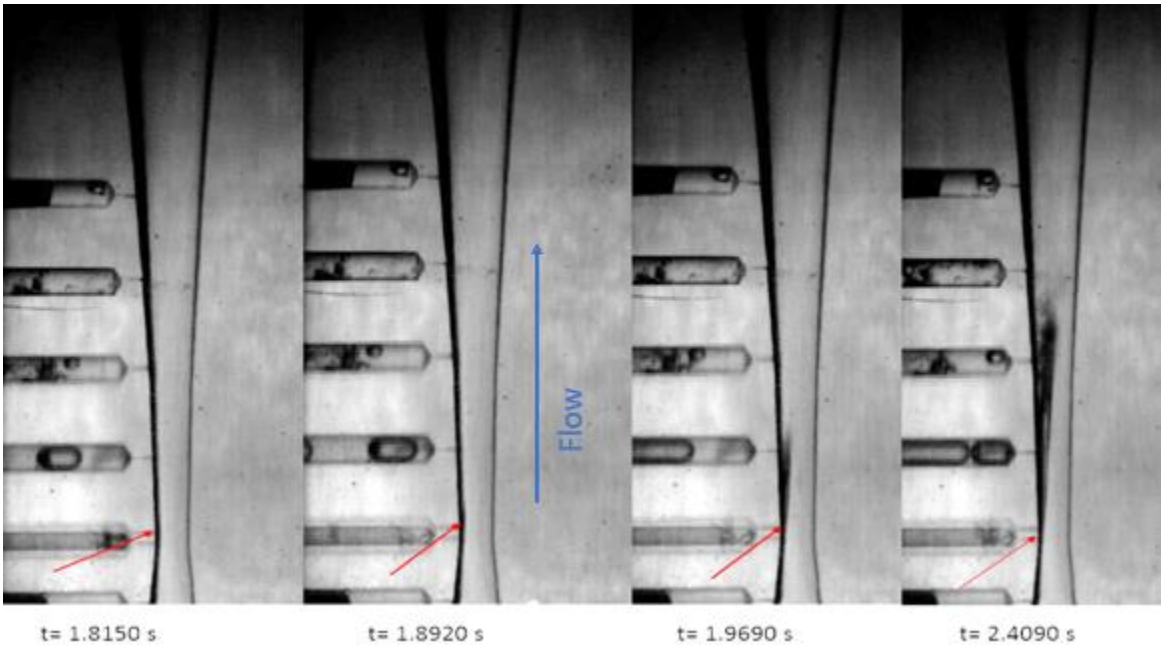

Figure 4.29: Flow visualization during fast-open test with a frame rate of 2000 frames per second

The pressure data from the fast-open test is presented in its raw form (Figure 4.32) and corrected form (Figure 4.33). The vertical black line in each figure represents the time when the flow reached steady state. In Figure 4.32, the pressure response is still settling after the flow has reached steady state. The goal of the algorithm is correct for this settling response. The model produced negative absolute pressures in the transient portion of the test and the pressure data then reached the same settled pressure as seen in the raw data. The corrective model appeared to work best after the flow reached steady-state.

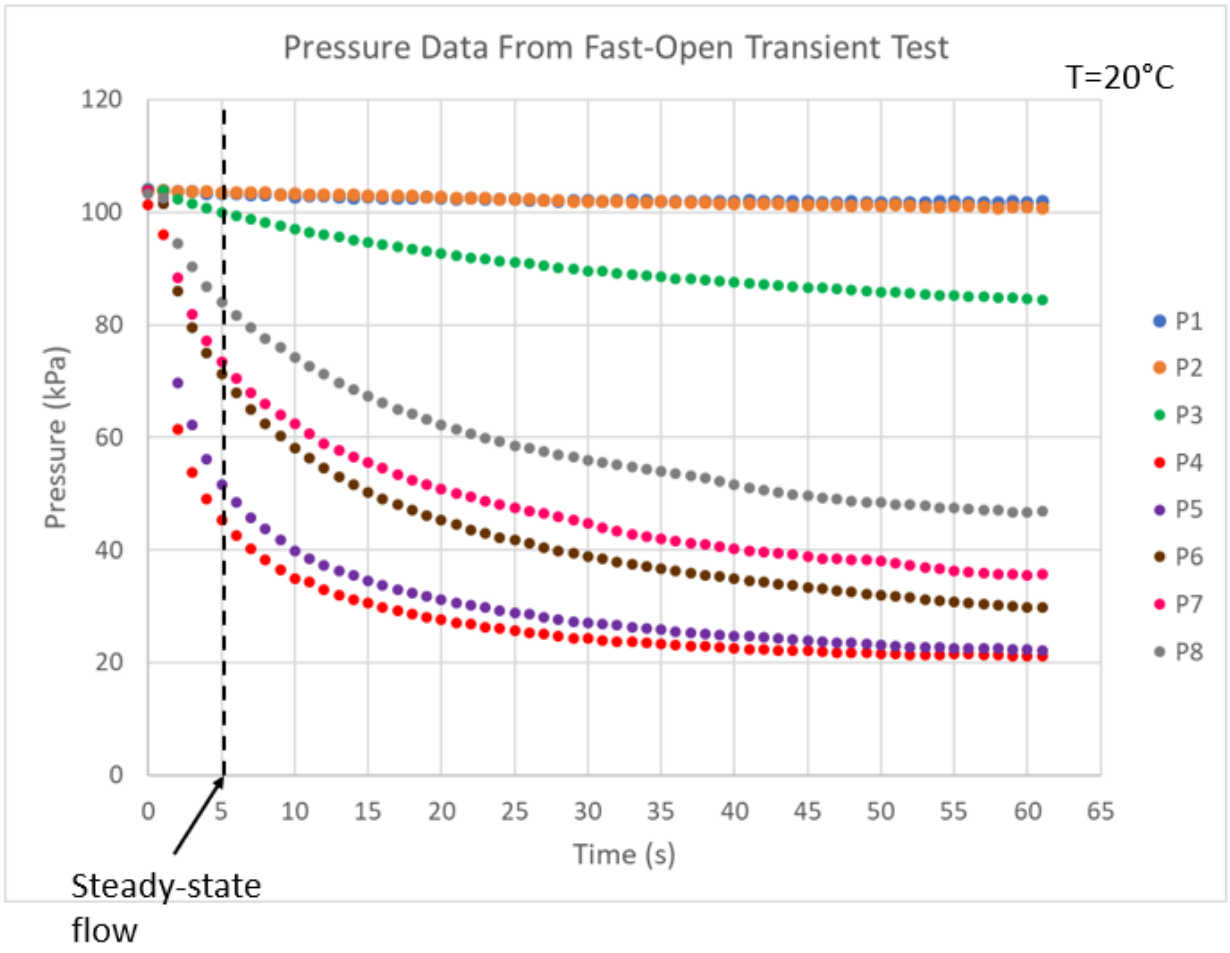

Figure 4.32: Raw pressure data from fast-open transient test

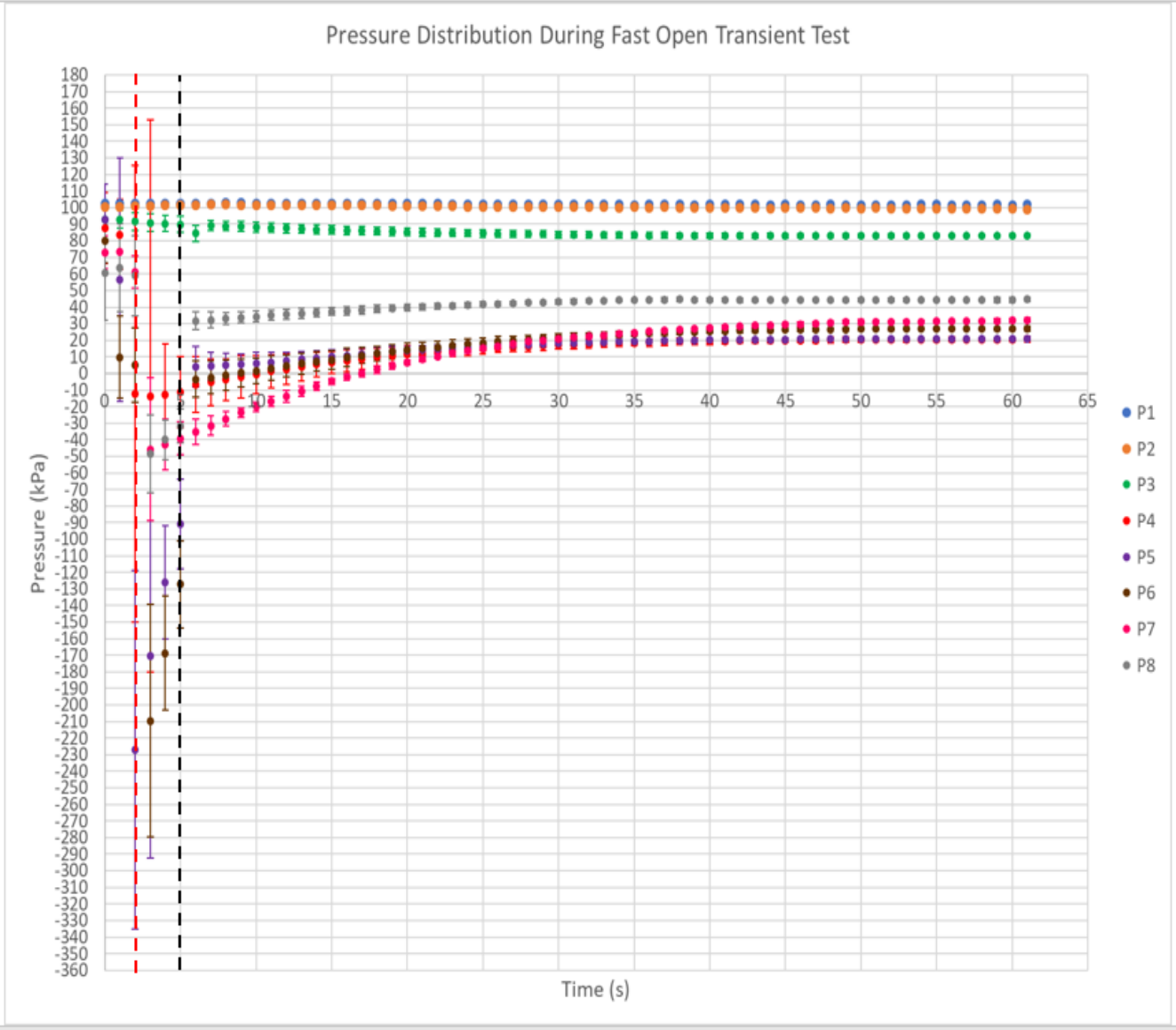

Figure 4.33: Corrected pressure results from the fast-open transient test

The slow open test reached a maximum flow rate of 24.76 mL/s and a steady state flow rate of 24.66 mL/s. The steady state flow was reached at 10 seconds into the test resulting in 5 more seconds of transient response. The flow rate response is shown in Figure 4.34. Cavitation initiated 4.026 seconds into the test and reached the full two-phase length at 5.346 seconds into the test (Figure 4.35). In the data correction, the single-phase time constant was used before the 4 second mark for all transducers. After the 4 second mark the two-phase time constant was used

for P4 and P5. Because the cavitation length is still developing until 5.346 seconds into the test, the two-phase time constant was used after the 6 second mark for P6, P7, and P8. The cavitation initiation and development are shown in the high-speed camera footage in Figure 4.35.

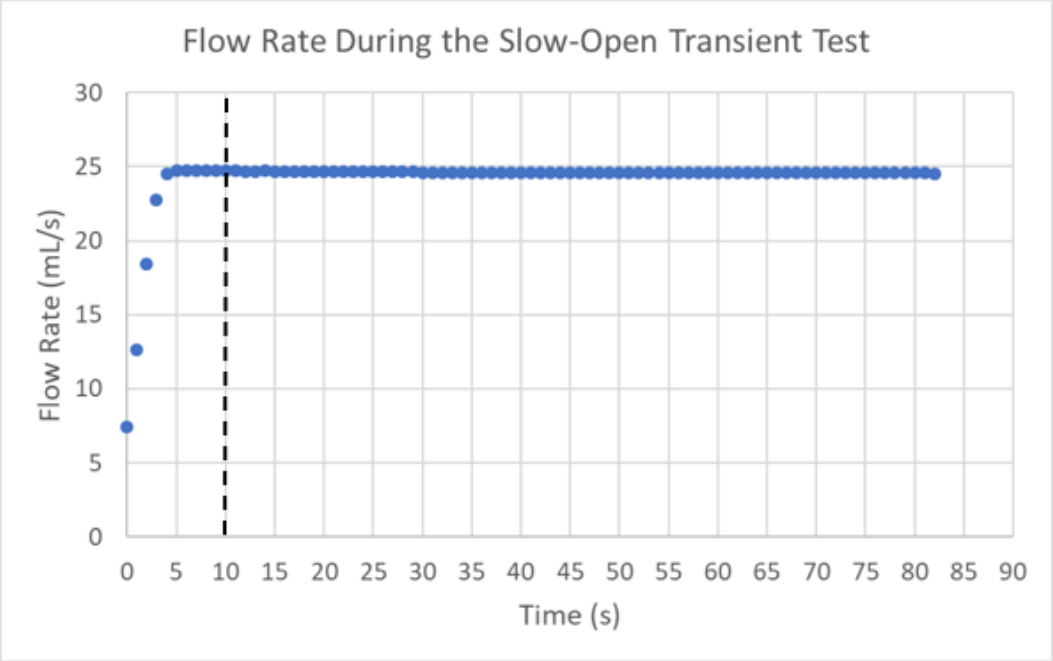

Figure 4.34: Flow rate response during slow-open transient test

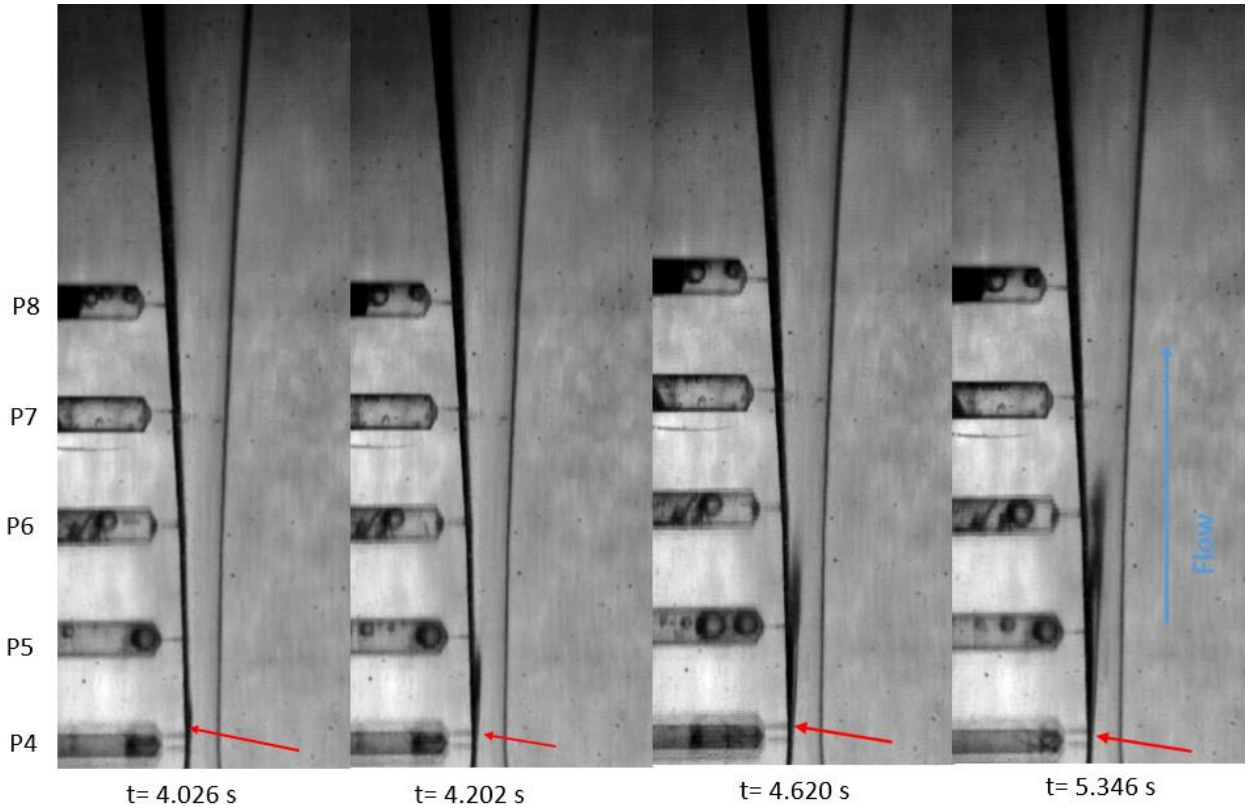

Figure 4.35: High-speed camera images (2000 frames per second) of slow-open transient test

The raw pressure data of the slow-open test did not reach steady state until 50 seconds for P4, and all other pressure transducers did not reach the corresponding steady state pressure during the test. The data correction resulted in negative absolute pressure at the throat and in the diverging section, P4 through P7 and P8 showed a dip in pressure below the steady state pressure. The pressure then slowly increased to the steady state pressure, which was achieved at 55 seconds. Figures 4.36 and 4.37 show the raw pressure data and the corrected data respectively. The black dashed line in the figures represents when the flow reached steady state and the red dashed line represents when the flow reached the maximum flow rate.

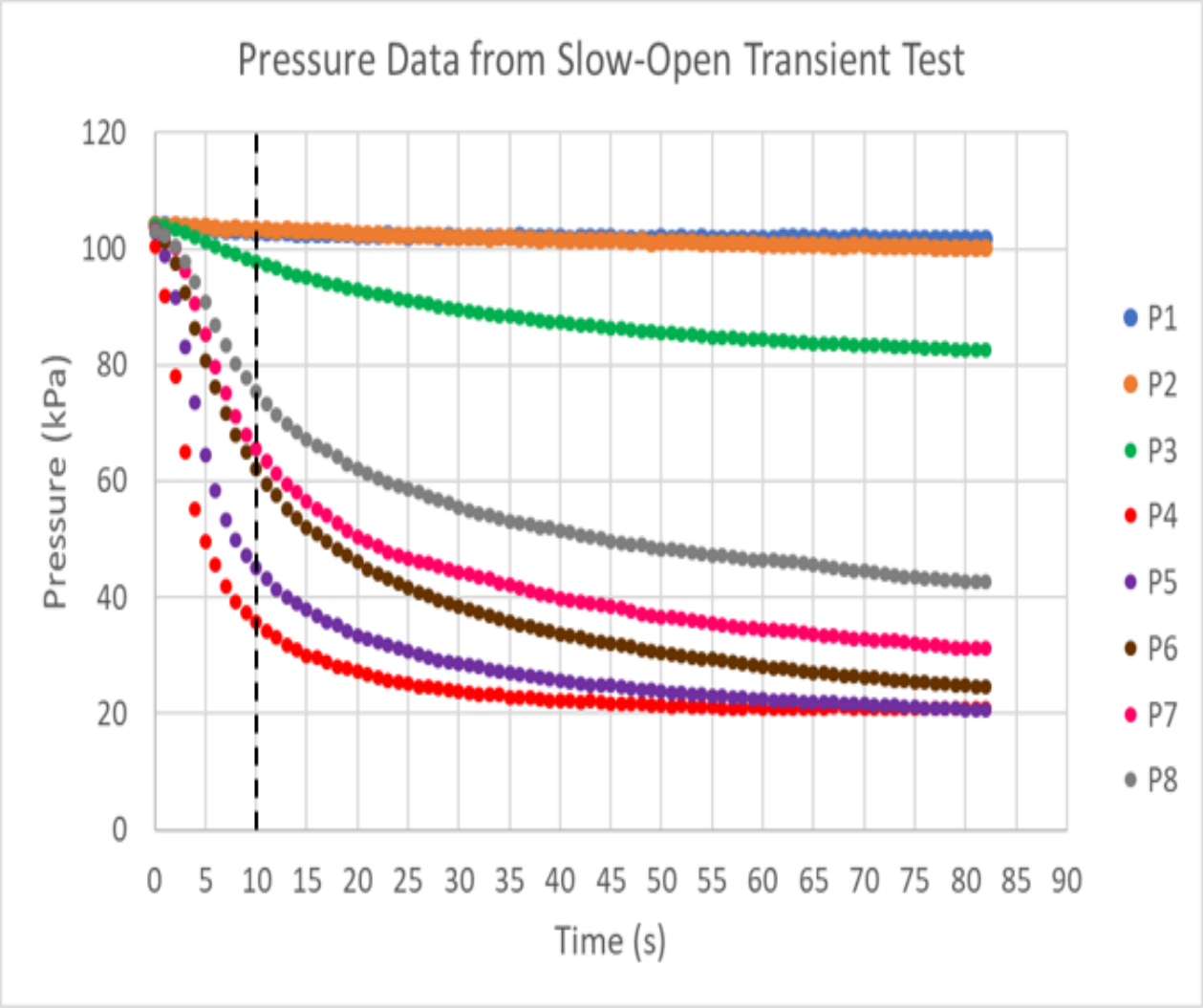

Figure 4.36: Raw pressure data from slow-open transient test

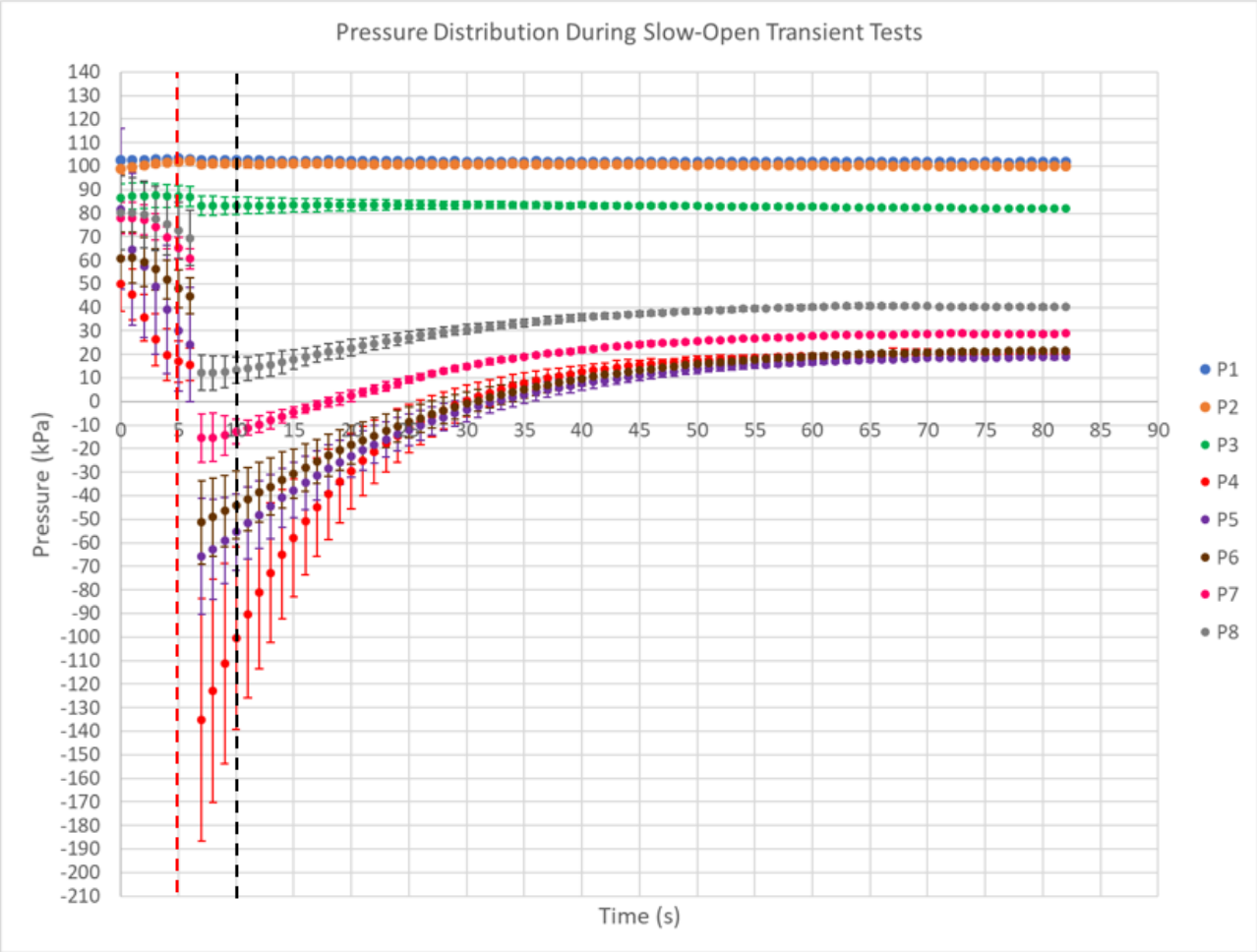

Figure 4.37: Pressure data corrected with linear model from slow-open transient test

To increase the flow rate in the nozzle, the upstream reservoir was elevated and thus the inlet pressure of the nozzle was increased by 7.0 kPa. This transient test was called the "increased upstream pressure test." The maximum flow rate in the increased upstream pressure test was 25.70 mL/s, and the steady state flow rate was 25.65 mL/s. This increased upstream pressure resulted in a 1.0 mL/s increase in maximum flow rate. The flow rate during the increased upstream pressure transient test is shown in Figure 4.38. The cavitation in the increased upstream pressure test initiated at 3.608 seconds. The two-phase region then covered P5 at 4.158 seconds, P6 at 4.708 seconds, and reached full length at 5.390 seconds. This led to

the corresponding two-phase time constant being used in the data correction after 4 seconds for P4, after 5 seconds for P5, and after 6 seconds for P6, P7 and P8. The cavitation initiation and growth in the nozzle is shown in Figure 4.39.

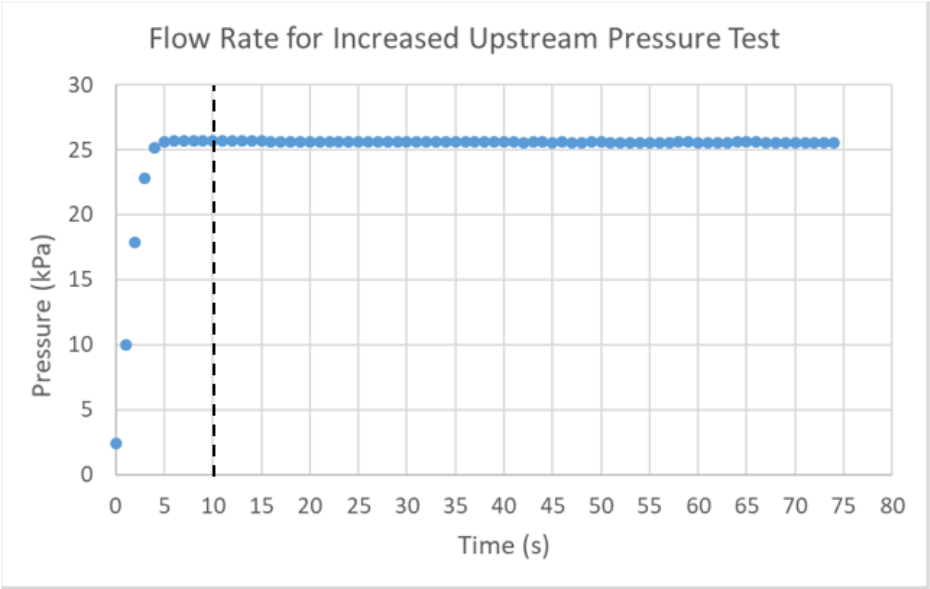

Figure 4.38: Flow rate during the increased upstream pressure test

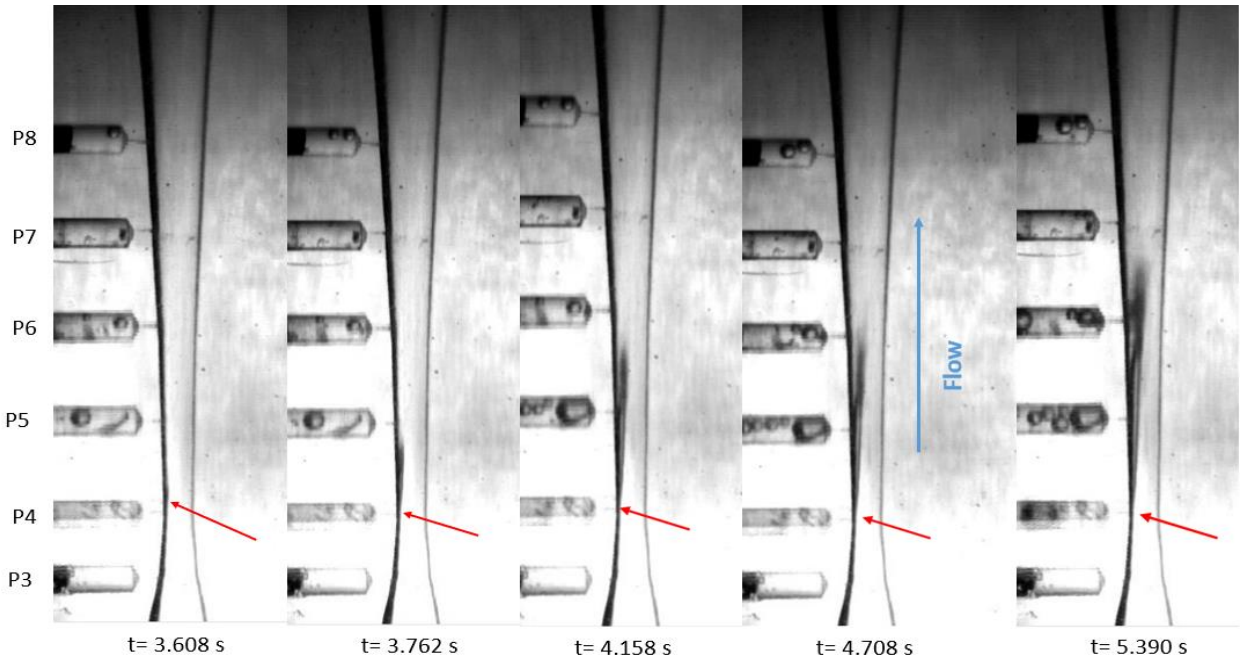

Figure 4.39: High-speed camera images of cavitation during increased upstream pressure test

The pressure data from the increased upstream pressure test was subjected to the same corrections as the fast- and slow-open tests. The raw pressure data featured a slow time delay and the pressure never reached a settled steady state pressure (Figure 4.40). The corrected data reached a steady state pressure after 10 seconds and featured negative absolute pressures in the transient section (Figure 4.41). This could indicate metastability in the flow, but this would be at odds with the flow response, which showed no overshoot.

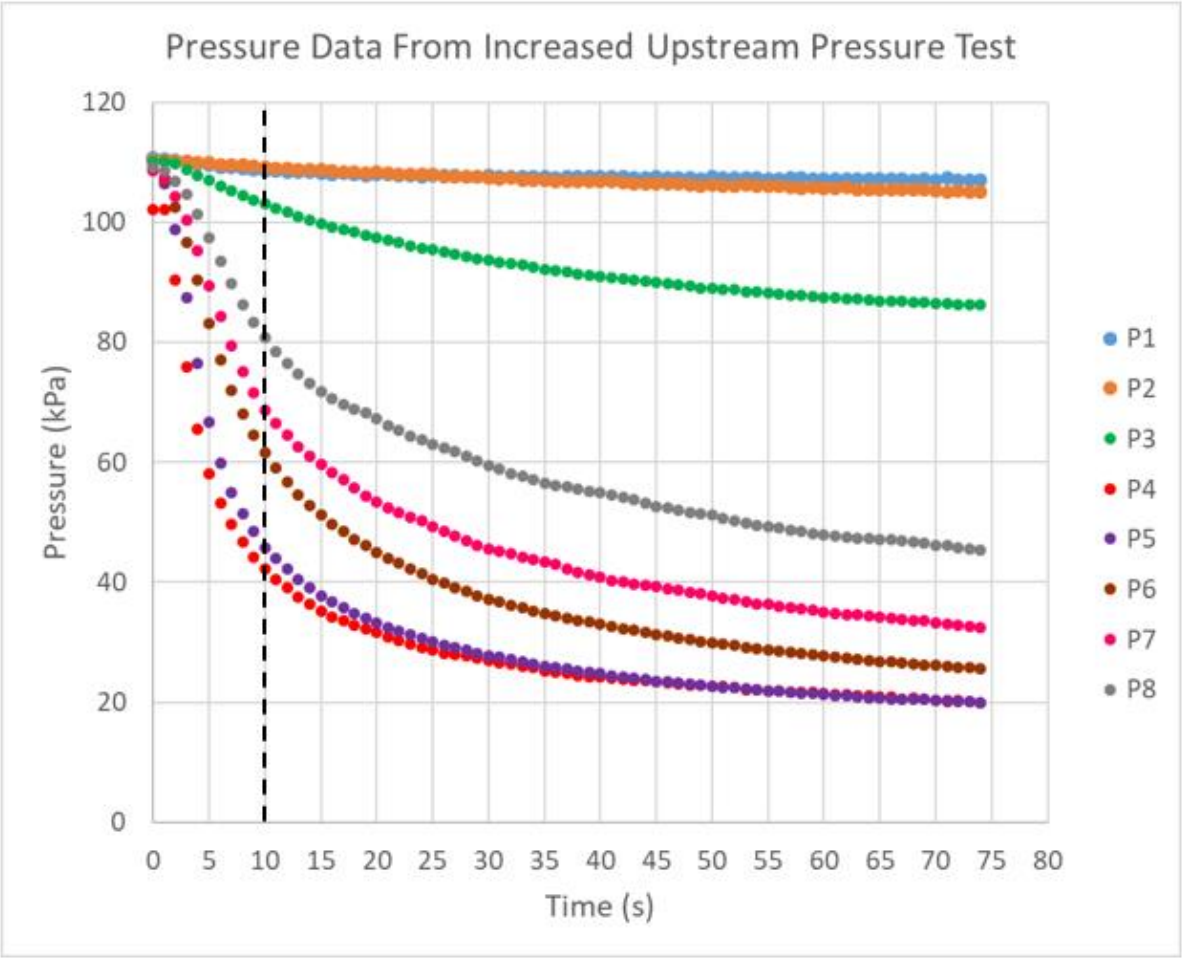

Figure 4.40: Raw pressure data from the increased upstream pressure test

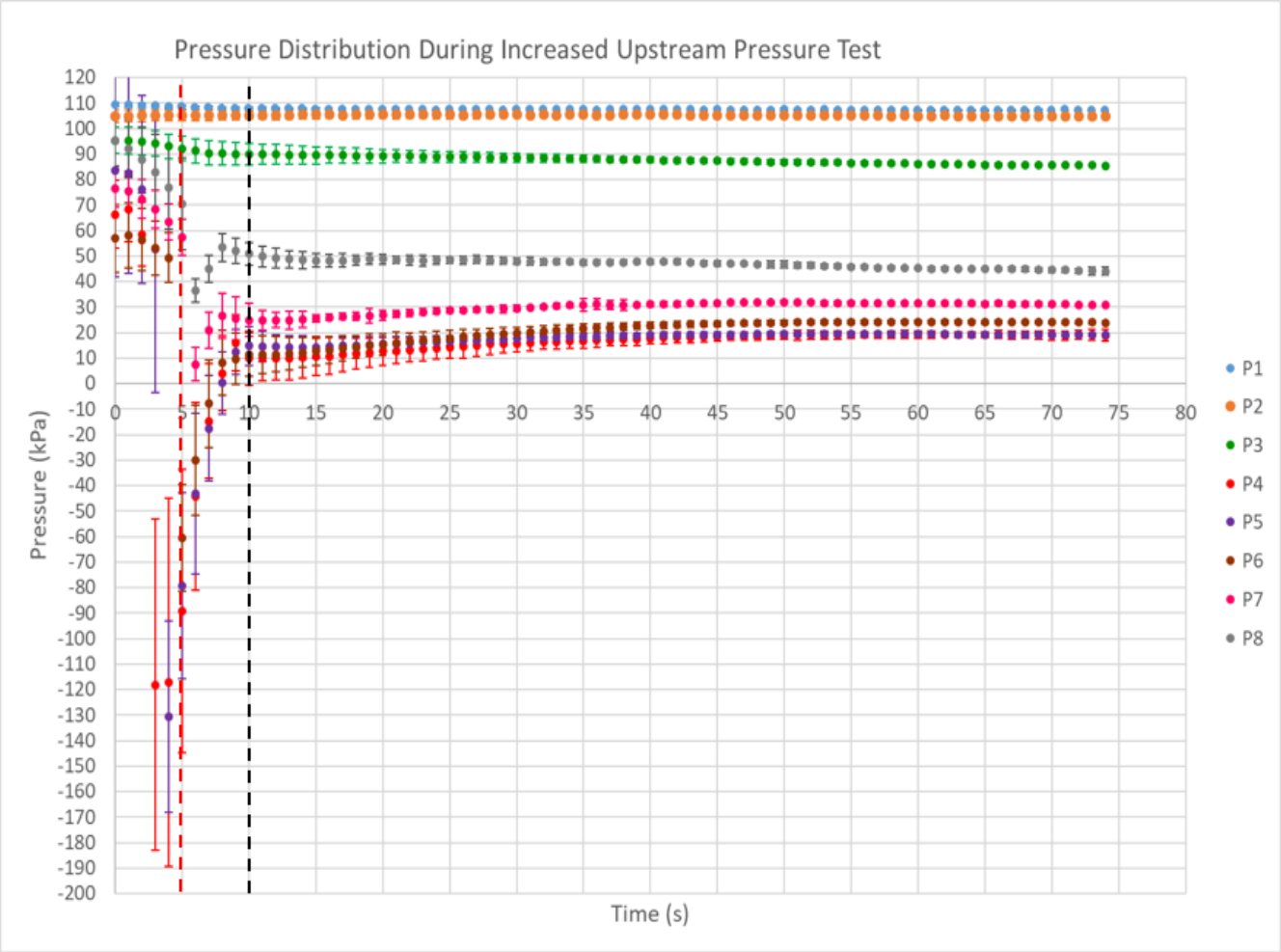

Figure 4.41: Corrected pressure data from the increased upstream pressure test

The cavitation initiated at the throat pressure tap for each transient test. This indicated a nucleation site at the throat, which lead to earlier cavitation. Earlier cavitation resulted in less metastability in the clear plastic nozzle as seen in the flow rates during the transient tests. The largest difference between maximum and steady state flow rates was found to be 0.1 mL/s in the slow-open transient test. This difference is an order of magnitude less than the difference seen in the glass nozzle, which was 7.0 mL/s. The raw pressure data appears to show no metastable behavior in the pressure response, as the pressure did not dip below the saturation pressure of 2.3 kPa. The pressure at each point in the nozzle decreased with increase in flow rate until reaching

steady state at the same time as the flow. This type of pressure response was expected for a transient with no metastability. A large overshoot in flow rate, as seen in the glass nozzle, would correspond to a dip in pressure before the steady state condition was achieved. The small peak in flow rate seen in the clear plastic nozzle would result in little to no dip in pressure before the steady state condition.

The corrected data resulted in an entirely different response where the pressure dipped to negative absolute pressures during cavitation initiation. This model of data correction would suggest that the pressure at the throat and in the diverging section had large metastability with negative absolute pressures as low as -227 kPa in the fast-open test, -135 kPa in the slow-open test, and -130 kPa in the increased upstream pressure test. With cavitation initiating at the pressure tap at the throat in every test, these low pressures indicate a local depression in flow pressure at the pressure taps. This small area of low pressure would act as a nucleation site for cavitation, which is seen in the high-speed camera images. Cavitation occurred only along the side of the nozzle with the pressure taps, and this would be a result of a region of lower pressure near the pressure taps. The negative pressures predicted by this data correction model do not agree with pressures predicted from the flow rate through the nozzle or pressures predicted by later data correction models

The uncertainty in the corrected data was found to be large as shown in Figures 4.33, 4.37, and 4.41. This large uncertainty limits the validity of any conclusions drawn from the corrected data. The uncertainty calculations are described in Appendix C. The large uncertainty was due to the uncertainty in the measured time constant and the uncertainty in the slope calculation. The slope in the transient section of each test was large in magnitude and due to the small number of data points in the transient portion the uncertainty in the slope calculation was

large. To increase the accuracy of the slope calculation and check the validity of the uncertainty calculations the throat pressure during the increased upstream pressure test was further analyzed. A third order polynomial curve fit was fitting to the transient portion of the data. This curve fit was used to generate artificial data points every 0.1 seconds by interpolation. This increased the density of data points in the transient section and the slope was then calculated using 20 total points instead of 5. Also, the slope was calculated over a smaller time interval. This new calculation resulted in a smaller uncertainty in the slope calculation but a larger magnitude of slope. The new slope and uncertainty where then used in Equation 4.7 and C.3. Figure 4.42 shows the data from the previous correction and from the new correction that uses the artificial data points. The new correction shows a lower negative absolute pressure in the transient region and the initial transient points were corrected to the settled steady state pressure. The uncertainty is of the same magnitude as the previous uncertainty and is only much larger for the 3 data points near when the maximum flow rate is achieved. This shows the previous uncertainty calculations are valid but that the data correction algorithm is likely over correcting the data during the transient portion of the tests.

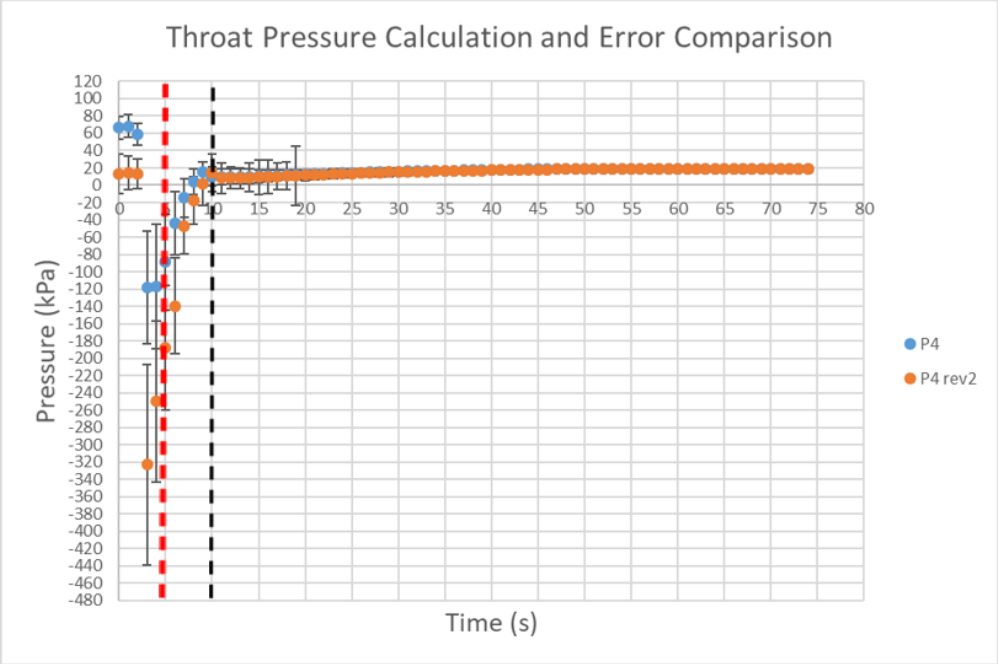

Figure 4.42: Throat pressure results comparison from the increased upstream pressure test

Pressure data correction with nonlinear model

The linear first order model used to correct the data was derived with the assumptions that inertial effects in the capillary tubes that connect the transducers to the nozzle are small and that the first order model is linear. The model focused on understanding the effect of gasses or water vapor being present in the pressure measurement system. The derivation shown in Appendix B for the first order model gives the time constant, τ, as a function of dynamic viscosity μ, length of the connecting tube L, volume of gas in the system V, diameter of the connecting tube d, and the average pressure in the system during the test $\bar{P}$ (Equation 4.8).

$$\boldsymbol{\tau = \frac{128\mu LV}{\pi^2 d^4 \bar{P}}} \qquad \textbf{(4.8)}$$

In Equation 4.8, all parameters are assumed to be constant. This assumption was inconsistent with experiments, when a different time constant was found for single- and two-phase flows.

Another consideration is that the first order model assumes linearity. The derivation in Appendix B shows that this is not actually the case. When the linearity assumption is relaxed, τ is no longer constant and can be written as Equation 4.9 where m is the mass of air, R is the gas constant of air, P is the pressure response of the pressure transducer and T_0 is the temperature of the air.

$$\tau = \frac{128mRT_0\mu L}{\pi^2 d^4 P^2} \quad (4.9)$$

The nonlinear first order model was applied to the data to improve the data correction. Figures 4.43 through 4.45 show the resulting data for each transient test with the nonlinear model used for data correction. The nonlinear model data corrections can be compared to the linear model data corrections shown in Figures 4.33, 4.37, and 4.41. The results show no negative absolute pressure which is closer to the expected pressure response in the nozzle. The uncertainty in the results from the nonlinear model is still large because the mass of air in the system is estimated using the time constant τ from the linear first order model.

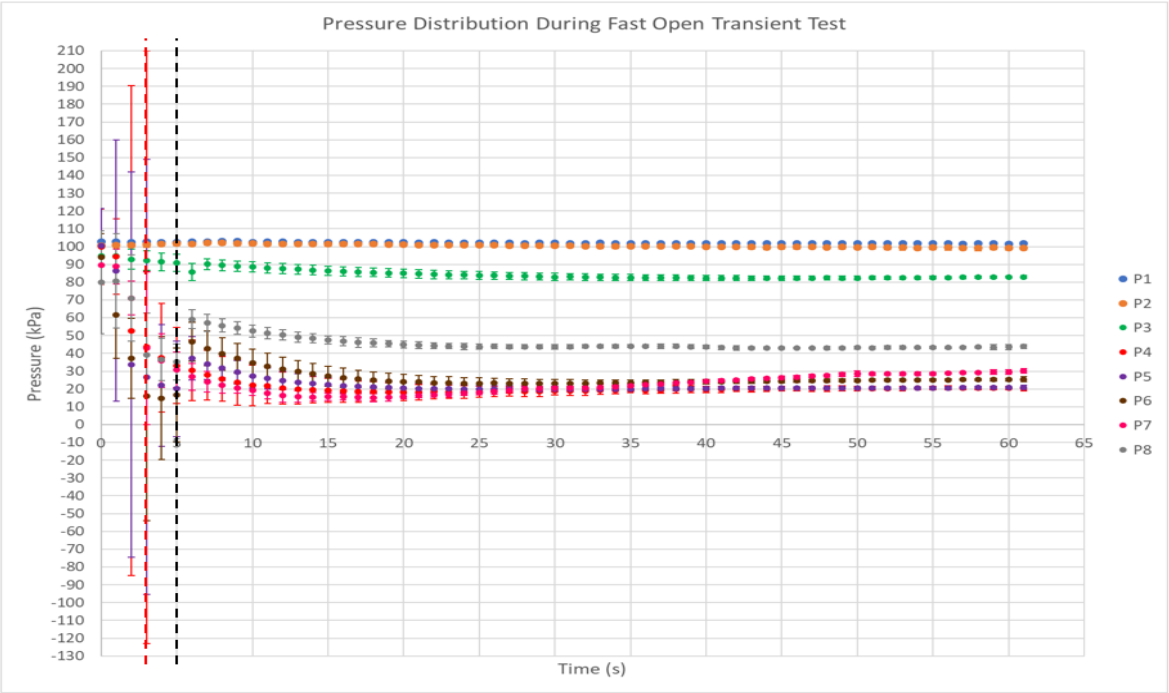

Figure 4.43: Fast open transient test results with nonlinear data correction model

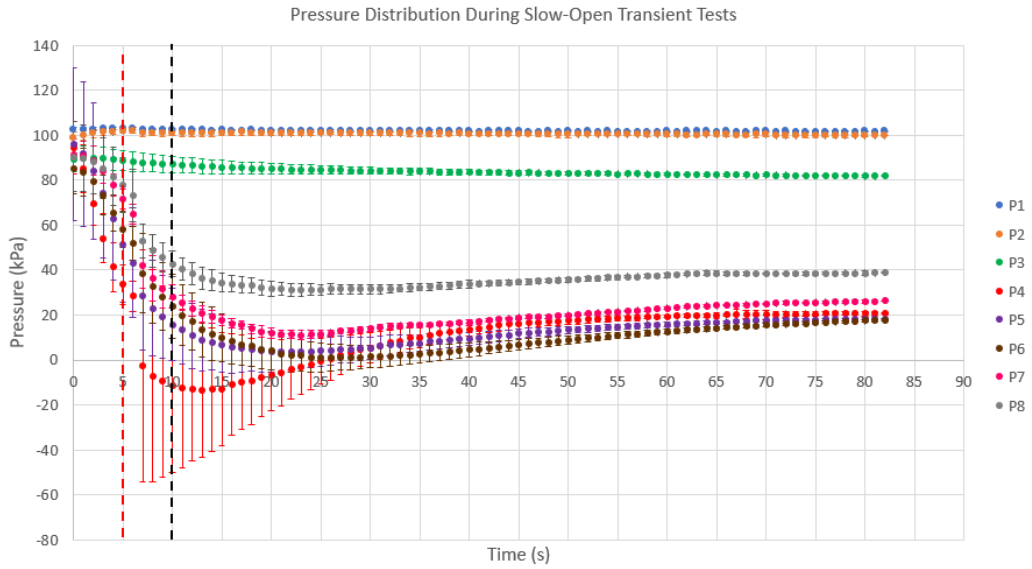

Figure 4.44: Slow open transient test results with nonlinear data correction model

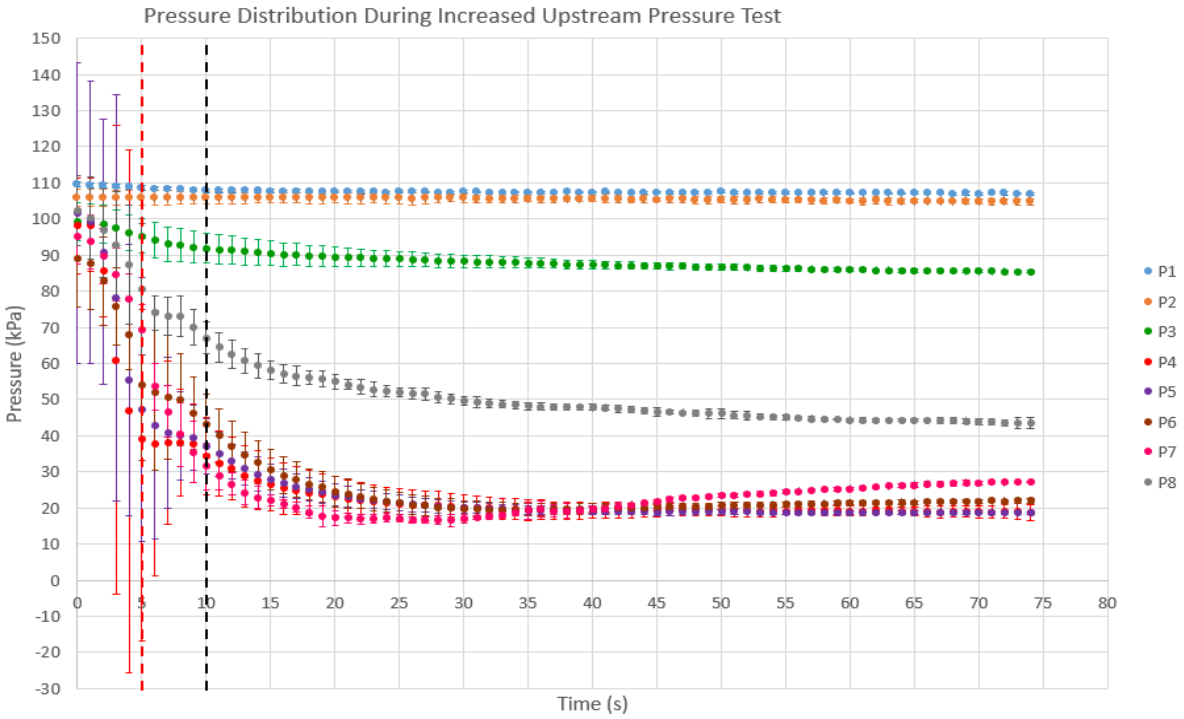

Figure 4.45: Increased upstream pressure transient results with nonlinear data correction model

The fast-open transient and increased upstream pressure results showed a decrease in pressure until the steady state pressure is achieved (Figure 4.43 and 4.45). No metastability was observed during this test. The slow-open transient test results showed a dip in pressure as the steady state flow rate was achieved (Figure 4.44). This dip in pressure indicated possible metastable behavior in the nozzle. Large uncertainty in the results limits the conclusions drawn on metastability but the data indicated that in each transient test there is a possibility of metastability. The steady state flow rate is represented on each pressure plot as a dotted black line and the dotted red line represents maximum flow in the system.

Clear Plastic Nozzle Conclusions

The clear plastic nozzle was used to gather steady state and transient flow and pressure measurements with flow visualization. The steady state single-phase measurements and theory calculations showed the roughness parameter in the nozzle was on the same order as the pressure taps. This meant the pressure taps potentially had a large contribution to the surface roughness effects. The steady state two-phase measurements showed the tendency of the nozzle to produce the Vena-contracta effect and when that happened the pressure downstream of the throat was lower than the pressure at the throat. This resulted in lower cavitation numbers in the diverging section of the nozzle. The visualization of the steady state tests showed that the length of the two-phase region depended on absolute back pressure and that the cavitation region always began at the throat pressure tap. A time delay was found in the attempt to measure the steady state pressure and was accounted for by collecting data after the pressure measurement system reached a steady-state output. The transient tests showed the importance of accounting for the delayed response of the pressure measurement system. A time constant was found for the pressure response in single-phase and two-phase flow. This time constant was then used in a data

correction method to interpret the pressure response during a transient test. The data correction method suggested the pressure may have exhibited metastable behavior and reach low negative absolute pressures during the transient and slow recovery to the steady state pressure. Large uncertainty in the data correction results limit the validity of conclusions drawn from the data. A nonlinear model was then used to get a better representation of the physical response in the pressure data. The predicted pressure in the nozzle did not show a dip below the saturation pressure and the data corrected with the nonlinear model better matched that prediction. The flow response in the transient test exhibited a smaller maximum flow and an order of magnitude less metastability when compared to the glass nozzle. The visualization showed cavitation initiated at the throat pressure tap in each transient test and then remain attached to the wall of the nozzle with the pressure taps.

Chapter 5 - Summary, Conclusions, and Future Recommendations

Summary and Conclusions

The work presented in this thesis included experimental results from three types of converging-diverging nozzles. The glass nozzles were used to analyze the low friction flow rates through the blow down system and as a benchmark for flow metastability at the onset of cavitation. An opaque plastic nozzle was design and built with 3D printing. It allowed for pressure measurements in the nozzle to accompany the flow measurements. This nozzle was used to understand limitations in plastic nozzles and pressure measurements. A clear 3D printed nozzle with a smooth surface finish was designed and manufactured to allow for direct pressure measurements and flow visualization. These measurements allowed a comparison of high-speed camera footage to pressure measurements.

The flow rates through several glass nozzles were compared. The geometry of the nozzles was the only factor affecting flow rate through the nozzle and was shown to have a significant effect on the maximum achieved flow rate. Because of this the geometry of the plastic nozzles was matched to the glass nozzle used in previous experiments by Ahmed (2017). Flow rate through the glass nozzle during a transient test showed significant metastable behavior due to the flow rate overshooting the choked flow rate by 7 mL/s before cavitation. This high metastability in flow through the glass nozzle was due to the smooth surface and lack of nucleation sites in the glass nozzles.

Steady state and transient flow results were gathered using the opaque plastic nozzle. In the steady state results the choked flow condition was reached at a flow rate of 17.34 mL/s, indicating that cavitation occurred at much lower flow rates in this nozzle. The minimum pressure in the nozzle was measured at the throat to be 6.00 ±0.8 kPa, which is above the

saturation pressure. However, the cavitation number at the throat was calculated to be 0.0762 ±0.017 which is much smaller than 1.04, which was measured as a threshold for cavitation. Pressure taps in the opaque nozzle were made with 0.75 mm diameter holes, and the 3D printed plastic had a rough surface finish. These surface defects acted as nucleation sites for cavitation, which allowed for cavitation at pressures above saturation pressure. In the transient results, the flow through the opaque plastic nozzle displayed no metastable behavior. The pressure measurements showed a slight dip in the pressure just beyond the throat before the flow reached the steady state condition. This slight dip was indicative of metastable behavior, but no negative absolute pressures were measured.

The clear plastic nozzle was used to capture flow visualization during steady state and transient tests. Single-phase steady state measurements were compared to pressure distribution calculations from a 1D mechanical energy balance. This comparison resulted in a roughness parameter in the nozzle of 0.10 mm which is on the same order as the pressure tap bore holes of diameter 0.1524 mm. The maximum single-phase flow was 20.9 mL/s and at faster flow rates cavitation occurred. The two-phase steady state results showed a choked-flow rate of 24.48 mL/s, which was smaller than the choked-flow in the glass nozzle. Pressure distributions during two-phase steady state tests showed that the minimum pressure occurred 4.0 mm downstream of the throat. This occurrence was likely due to the Vena-contracta effect. The flow visualization captured the cavitation beginning at the throat pressure tap and allowed for the measurement of the length of the two-phase region. The pressure measurement system displayed a delayed response in the pressure output. In the steady state measurements this was accounted for by collecting data after the pressure output reached the settle steady state pressure. In the transient test the time delay response was characterized with a first order model and a time constant. The

time constant was shown to depend on the phase of the fluid in the nozzle and thus the volume of gas in the pressure measurement system. The first order model was used in a data correction method that resulted in negative absolute pressures that occurred in the transient portion of the tests. This suggested large metastable behavior and the likelihood of a low-pressure region near the pressure taps. However, the first-order model is less accurate during fast pressure changes and the uncertainty in the results was large. High-speed camera footage of the transient tests suggested a nucleation site at the throat of the nozzle because cavitation appears to always initiated at the throat pressure tap. The cavitation region then stayed attached to the wall of the nozzle with the pressure taps. The data gathered from the clear plastic nozzle suggests a possibility of negative absolute pressures in a converging-diverging nozzle and that flow visualization was critical for the interpretation of pressure data.

Future Work Recommendations

The clear plastic nozzle allowed for direct pressure measurements to be paired with flow visualization. However, the surface roughness of the nozzle resulted in earlier cavitation and lower flow rates when compared to the smooth glass nozzles. New rapid prototyping or other manufacturing processes should be investigated to achieve a clear smooth nozzle that allows for direct pressure measurement. A smoother surface finish would allow for larger flow rates through the nozzle and thus lower pressures at the throat. This would result in larger metastability and the possible presence of negative absolute pressures that could be measured directly.

The experimental results should be used to verify a theoretical model that can predict the pressure distribution, cavitation initiation, and the length of the two-phase region. The theoretical model could then be used to optimize nozzle geometry to achieve maximum lengths of the two-

phase region. This would allow for a greater cooling potential and could improve the viability of a non-vapor compression refrigeration process. The optimized nozzles could then be manufactured using the clear rapid prototyping technique and tested to verify the optimization process. These tests could be done with a variety of fluids and refrigerants to generate a broader range of data. Currently only water has been used in the clear plastic nozzle because the interest of this work was the fluid mechanics of cavitation. Other fluids should be investigated so that the cavitation fluid mechanics can be paired with measured temperature drops.

During the pressure measurements, bubble generation was observed in the connecting pressure lines. This could be due to phase change in the connecting lines as well as fluid being pulled into the nozzle. The suction of flow into the nozzle could be a factor in premature cavitation. This should be investigated further to analyze the effects this has on cavitation. Also, the connecting lines could be connected to a vacuum reservoir in an attempt to control the separation in the diverging section of the nozzle by suction. This investigation could result in the control in the cavitation front and the length of the two-phase region and should be tested experimentally.

References

Alkotami, A., Beck, T., Sorensen, C. M., Hosni, M. H., Eckels, S. J., & Tomasi, D. (2015). A Thermodynamic Analysis of the Temperature Drop and Potential Cooling Effect of Cavitation. Proceedings of IMECE 2015.

Ahmed, Z. (2017). Quantitative flow measurement and visualization of cavitation initiation and cavitating flows in a converging-diverging nozzle. M.S. Thesis, Mechanical and Nuclear Engineering Kansas State University

Owen, I., Abdul-Ghani, A., & Amini, A. (1992). Diffusing a homogenized two-phase flow. International Journal of Multiphase Flow, 18(4), 531-540. doi:10.1016/0301-9322(92)90050-q

Brennen, Christopher E. Cavitation and Bubble Dynamics. Cambridge University Press, 2013.

Cengel, Yunus A., and Michael A. Boles. "Thermodynamics: an engineering approach." Sea 1000 (2002): 8862.

Charamko, Serguei, Kristian Debus, and Tom Gielda. "Cooling system utilizing a reciprocating piston." U.S. Patent Application No. 13/087,062

Collier, J.G., and Thome, J.R. (1994). *Convective Boiling and Condensation*. Oxford: Clarendon Press

Davis, M., & Dunn, Patrick F. (2008). Experimental Investigation of the Cavitation of Aviation Fuel in a Converging -diverging Nozzle, ProQuest Dissertations and Theses.

Doebelin, E.O. (1990). *Measurement Systems: Application and Design.* Ohio: McGraw-Hill

Fowler, R.L. (1963). An Experimental Study of the Effects of Liquid Inertia and Viscosity on the Dynamic Response of Pressure Transducer-Tubing Systems. The Ohio State Univeristy.

Goetzler, W., Zogg, R., Young, J., & Johnson, C. (2014). Alternatives to vapor-compression HVAC technology. ASHRAE Journal, 56(10), 12-14,16,18,20-23.

Imre, A., Martinás, K., & Rebelo, L. (1998). Thermodynamics of Negative Pressures in Liquids. Journal of Non-Equilibrium Thermodynamics, 23(4), 351-375.

Mann, Madamadakala, & Eckels. (2016). Heat transfer characteristics of R-134a in a converging-Diverging nozzle. International Journal of Heat and Fluid Flow, 62(PB), 464-473

Petkovšek, & Dular. (2013). IR measurements of the thermodynamic effects in cavitating flow. International Journal of Heat and Fluid Flow, 44(C), 756-763.

Schmidt, Aaron (2016). Quantitative Measurement and Flow Visualization of Water Cavitation in a Converging-Diverging Nozzle. M.S. Thesis, Mechanical and Nuclear Engineering Kansas State University

Simões-Moreira, & Bullard. (2003). Pressure drop and flashing mechanisms in refrigerant expansion devices. International Journal of Refrigeration, 26(7), 840-848.

Trevena, D. H. (1987). Cavitation and tension in liquids. Bristol: Adam Hilger.

Wilms, J. (2016). Flow visualization of cavitation (Doctoral dissertation, Kansas State University).

Appendix A - Instrumentation and Nozzle Geometry

The nozzle geometry was generated with a fifth order polynomial fit to the glass nozzle used by Ahmed, 2017. The instrumentation for the blow-down system included instrumentation for pressure measurements, flow measurements, and high-speed flow visualization.

Nozzle Geometry

The fifth order polynomial used to generate the clear 3D printed nozzle was split into a converging section and diverging section. The fifth order polynomial fit was fitted to data from a refractive index matching method with the glass nozzle (Ahmed, 2017). The model was derived using the radius of curvatures and that the slope of the nozzle at the throat is zero. Figure A.1 shows the curve of the nozzle with L_C being the length of the converging section, L_D being the length of the diverging section, R_t being the radius at the throat, R_i being the radius of the inlet of the nozzle, r_{c1} is the radius of curvature at the inlet, r_{c2} is the radius of curvature at the throat, and r_{d1} is radius of curvature at the outlet.

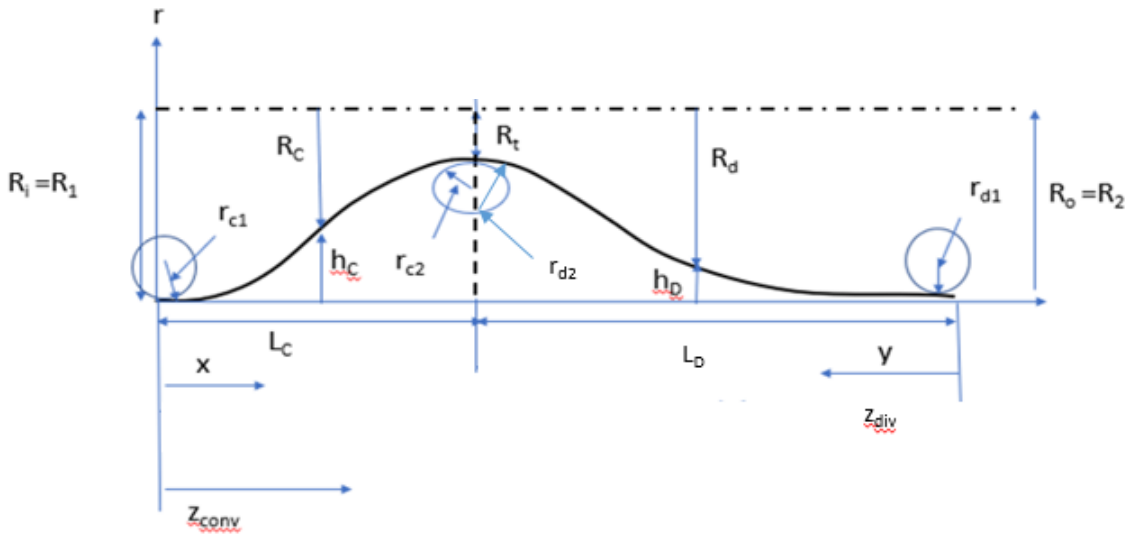

Figure A.1: Schematic of nozzle geometry curve

The coefficients of the 5th order fit were found with the following equations that were derived using the radius of curvature. The general polynomial form of the converging section is shown in Equation A.1. Equations A.2 and A.3 show the system of equations used to solve for the constants in the converging section.

$$\boldsymbol{h_c\,(x) = C_0 + C_1 x + C_2 x^2 + C_3 x^3 + C_4 x^4 + C_5 x^5} \qquad \textbf{(A.1)}$$

$$\begin{bmatrix} \boldsymbol{L_C^3} & \boldsymbol{L_C^4} & \boldsymbol{L_C^5} \\ \boldsymbol{3L_C^2} & \boldsymbol{4L_C^3} & \boldsymbol{5L_C^4} \\ \boldsymbol{6L_C} & \boldsymbol{12L_C^2} & \boldsymbol{20L_C^3} \end{bmatrix} \begin{bmatrix} \boldsymbol{C_3} \\ \boldsymbol{C_4} \\ \boldsymbol{C_5} \end{bmatrix} = \begin{bmatrix} \boldsymbol{(R_1 - R_t) - (\frac{L_C^2}{2r_{c1}})} \\ \boldsymbol{-(\frac{L_C}{rc_1})} \\ \boldsymbol{(\frac{1}{r_{c2}} - \frac{1}{rc_1})} \end{bmatrix} \qquad \textbf{(A.2)}$$

$$\boldsymbol{C_0 = 0;\ C_1 = 1;\ C_2 = \frac{1}{2rc_1}} \qquad \textbf{(A.3)}$$

The general polynomial form of the diverging section is shown in Equation A.4. Equations A.5 and A.6 show the system of equations used to solve for the constants in the diverging section.

$$\boldsymbol{h_d(y) = D_0 + D_1 y + D_2 y^2 + D_3 y^3 + D_4 y^4 + D_5 y^5} \qquad \textbf{(A.4)}$$

$$\begin{bmatrix} L_D^3 & L_D^4 & L_D^5 \\ 3L_D^2 & 4L_D^3 & 5L_D^4 \\ 6L_D & 12L_D^2 & 20L_D^3 \end{bmatrix} \begin{bmatrix} D_3 \\ D_4 \\ D_5 \end{bmatrix} = \begin{bmatrix} (R_O - R_t) - (\frac{L_D^2}{2rd_2}) \\ -(\frac{L_D}{r_{d2}}) \\ (\frac{1}{r_{d1}} - \frac{1}{r_{d2}}) \end{bmatrix} \quad \textbf{(A.5)}$$

$$D_0 = 0; D_1 = 0;\ D_2 = \frac{1}{2r_{d2}} \quad \textbf{(A.6)}$$

The geometry parameters that were measured are the lengths, throat radius, and radius of curvatures. The parameters are as follows: R_1 = 4.665 mm, L_c = 22.88mm, R_t = 0.855mm, r_{c1} = 150 mm, r_{c2} = 30 mm, L_D = 67 mm, r_{d1} = 172mm, r_{d2}=50mm, and R_2=4.665mm. These parameters were used to solve for the constants in Equations A.1 and A.4. Equations A.1 and A.4 were then substituted into Equations A.7 and A.8 to get the radius as a function of length along the nozzle with z_{conv} = x and z_{div} = y.

$$R_{conv}(z_{conv}) = R_1 - h_c(z_{conv}) \quad \textbf{(A.7)}$$

$$R_{div}(z_{div}) = R_2 - h_D(z_{div}) \quad \textbf{(A.8)}$$

The resulting equations for the polynomial fits are shown in Equations A.9, the converging section, and A.10, the diverging section.

$$R_{conv} = 4.665 - 3.333 * 10^{-3} * z_{conv}^2 + 0.0023068 * z_{conv}^3 - 0.000151234 * z_{conv}^4 + 2.53263 * 10^{-6} * z_{conv}^5 \quad \textbf{(A.9)}$$

$$R_{div} = 4.665 - (2.90698 * 10^{-3} * z_{div}^2 - 6.59636 * 10^{-5} * z_{div}^3 + 9.71687 * 10^{-7} * z_{div}^4 - 6.65167 * 10^{-9} * z_{div}^5) \quad \textbf{(A.10)}$$

Pressure Measurements

The pressure measurements were made using 0-30 psia transducers, 0-150 psia transducers, 0-15 psia transducers, and a 0-25 psid transducer. The differential pressure transducer was used at the throat of the clear plastic nozzle to measure negative absolute pressures. The high side of the pressure transducer was exposed to atmospheric pressure and the low side was connected to the nozzle pressure tap. The pressure at the tap is then the atmospheric pressure minus the pressure difference measured by the differential transducer. The pressure in

the downstream reservoir was measured by a dial gage. The model and uncertainty for each type of transducer is listed below.

- 0-30 psia transducers:

  Viatran 245 absolute pressure transducer

  Uncertainty: ±0.1% Full scale accuracy

- 0-150 psia transducers

  Omegadyne PX409 absolute pressure transducer

  Uncertainty: ±0.08% Best Straight Line (BSL) accuracy

- 0-15 psia transducers

  Omega PX309 absolute pressure transducer

  Uncertainty: ±0.25% Best Straight Line (BSL) accuracy

- 0-25 psid transducer

  Setra Model 230 differential pressure transducer

  Uncertainty: ±0.25% Full scale accuracy

The pressure transducers were calibrated for the bias offset using a mercury barometer. An example of this calibration is shown in Table A.1 where the barometer reading was 14.42 psi. This example calibration was done for the clear plastic nozzle.

Table A.1: Offset calibration example for the clear plastic nozzle

Pressure Transducer	P1	P2	P3	P4	P5	P6	P7	P8
Atmospheric Output (psi)	14.42594	13.62733	14.13079	0.132505	14.50478	14.20266	14.35093	14.48934
Offset (psi)	-0.00594	0.792666	0.28209	-0.13251	-0.08478	0.217342	0.069068	-0.06934

Flow Measurements

Flow measurements were made with a rotameter and a Coriolis mass flowmeter. The specifications for these instruments are listed below.

- Rotameter

  Fischer & Porter rotameter

  Range: 0-0.81 gpm or 0-51 mL/s

  Uncertainty: ±2% Full scale accuracy

- Coriolis mass flowmeter

  Micro Motion CMF025 sensor

  Micro Motion Model 2700 transmitter

  Range: 5 g/cm^3 to 5000 kg/m^3

  Uncertainty: ±0.10% reading accuracy

Flow Visualization

The high-speed flow visualization was capture with the Photron FASTCAM SA5 high speed camera. The camera was paired with the Photron software to save video files to the computer. The camera had an internal memory of 8 GB and a maximum resolution. Figure from the Photron website shows the camera specifications.

Specifications: Partial Frame Rate / Recording Duration Table

FRAME RATE (fps)	MAXIMUM RESOLUTION Horizontal	Vertical	MAXIMUM SHUTTER SPEED	RECORD DURATION (12-BIT) TIME (Sec.) 8GB	16GB	32GB	64GB	FRAMES 8GB	16GB	32GB	64GB
1,000	1,024	1,024	1 µs 1/1,000,000 sec	5.46	10.92	21.84	43.68	5,457	10,918	21,841	43,686
2,000	1,024	1,024		2.73	5.46	10.92	21.84	5,457	10,918	21,841	43,686
4,000	1,024	1,024		1.36	2.73	5.46	10.92	5,457	10,918	21,841	43,686
5,000	1,024	1,024		1.09	2.18	4.37	8.73	5,457	10,918	21,841	43,686
7,000	1,024	1,024		0.78	1.56	3.12	6.24	5,457	10,918	21,841	43,686
7,500	1,024	1,000		0.75	1.49	2.98	5.96	5,588	11,180	22,365	44,735
9,300	1,024	800		0.75	1.50	3.01	6.01	6,985	13,975	27,956	55,918
10,000	1,024	744		0.75	1.50	3.01	6.01	7,511	15,027	30,061	60,127
15,000	960	528		0.75	1.51	3.01	6.02	11,289	22,587	45,182	90,374
20,000	832	448		0.77	1.54	3.07	6.14	15,352	30,716	61,443	122,898
30,000	768	320		0.78	1.55	3.11	6.21	23,284	46,586	93,189	186,396
50,000	512	272		0.82	1.64	3.29	6.57	41,090	82,211	164,452	328,934
75,000	320	264		0.90	1.81	3.61	7.22	67,737	135,523	271,097	542,244
100,000	320	192		0.93	1.86	3.73	7.45	93,138	186,345	372,758	745,585
150,000	256	144		1.03	2.07	4.14	8.28	155,230	310,575	621,264	1,242,642
300,000	256	64		1.16	2.33	4.66	9.31	349,269	698,794	1,397,845	2,795,946
420,000	128	64		1.66	3.33	6.66	13.31	698,538	1,397,589	2,795,690	5,591,893
525,000	128	48		1.77	3.55	7.10	14.20	931,384	1,863,452	3,727,587	7,455,857
775,000	128	24		2.40	4.81	9.62	19.24	1,862,769	3,726,904	7,455,175	14,911,715
930,000	128	16	369 ns 1/2,712,000 sec	3.00	6.01	12.02	24.05	2,794,154	5,590,357	11,182,762	22,367,573
1,000,000	64	16		5.59	11.18	22.37	44.73	5,588,309	11,180,714	22,365,525	44,735,146

OPTION SUBJECT TO EXPORT LICENSE CONTROL RESTRICTIONS WHERE APPLICABLE

Sensor	12-bit ADC (Bayer system color, single sensor) with 20µm pixel
Shutter	Global electronic shutter from 16.7ms to 1µs independent of frame rate
Lens Mount	Interchangeable F-mount and C-mount using supplied adapters
Extended Dynamic Range	Selectable in twenty steps (0 to 95% in 5% increments) to prevent pixel over-exposure
Memory	8GB (standard: 5,457 frames @ maximum resolution) 16GB (option: 10,913 frames @ maximum resolution) 32GB (option: 21,841 frames @ maximum resolution) 64GB (option: 43,686 frames @ maximum resolution)
Video Output 1	NTSC/PAL composite VBS (BNC). Ability to zoom, pan and tilt within image via keypad. Live video during recording
Video Output 2	HD-SDI: HD-SDI 2 channel (BNC) digital output
Camera Control	Through optional keypad with integrated viewfinder and Gigabit Ethernet or RS-422
User Preset Switches	Four user selectable camera function controls mounted on the camera's rear panel
Low Light Mode	Low light mode drops the frame rate and shutter time to their maximum values, while maintaining other set parameters, to enable users to position and focus the camera
Triggering	Selectable positive or negative TTL 5Vp-p or switch closure
Trigger Delay	Programmable delay on selected input and output triggers, 100ns resolution
Timing	Internal clock or external source
Phase Lock	Enables cameras to be synchronized precisely together to a master camera or external source, such as IRIG/GPS time codes
Event Markers	Ten user entered event markers mark specific events within the image sequence in real time. Immediately accessible through software
Dual Speed Recording	Enables the recording speed to be changed up or down by a factor of 2, 4 or 8 during a recording
Trigger Modes	Start, End, Center, Manual, Random, Random Reset, Random Center, Random Manual and Duals Speed Recording
Saved Image Formats	JPEG, AVI, TIFF, BMP, RAW, PNG, MOV and FTIF. Images can be saved with or without image or comment data
Data Display	Frame Rate, Shutter Speed, Trigger Mode, Date or Time, Status (Playback/Record), Real Time, Frame Count and Resolution
Partitioning	Up to 64 memory segments for multiple recording in memory
Data Acquisition	Supports Photron MCDL and DAQ
Cooling	Actively cooled
Operating Temperature	0 - 40 degrees C (32 - 104 degree F)
Mounting	1 x 1/4 - 20 UNC, 1 x 3/8 - 16 UNC, 6 x M6
Dimensions	165mm (6.50")H×153mm (6.02")W×242.5mm (9.55")D *excluding protrusions
Weight	6.2 kg (13.67 lbs)
Power Requirements	100V-240V AC ~ 1.5A, 50-60Hz DC operation 18-36 V DC, 100VA

Figure A.2:High-speed camera specifications

Appendix B - Data Correction Model

The first order data correction model was derived by applying the conservation of mass to the liquid volume in the pressure measurement system and a force balance on the fluid in the connecting tube. It was assumed that no phase-change occurred in the pressure measurement system. Figure B.1 shows the schematic of the pressure measurement system.

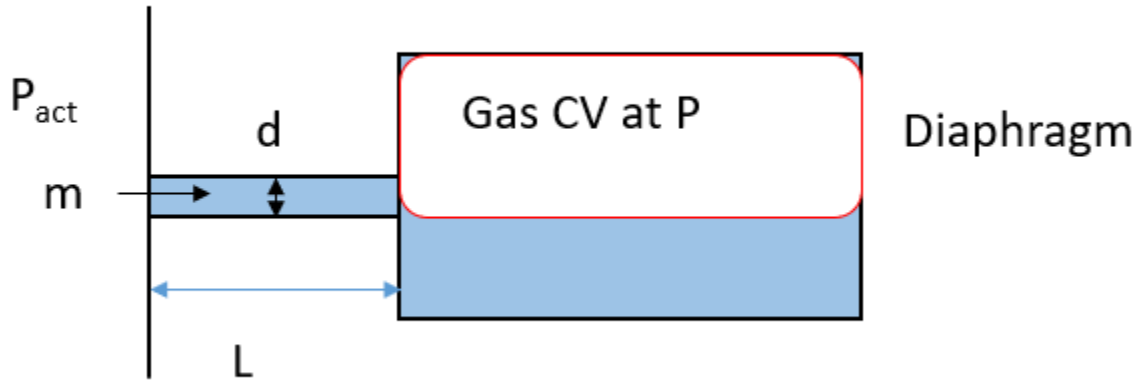

Figure B.1: Diagram of pressure measurement system

The conservation of mass is applied to a control volume that consists of the entire pressure measurement system. The results are then equated to the volume of trapped gas by equating the change in volume liquid to the change in volume of gas. This resulted in Equation B.1.

$$\frac{dV_{liq}}{dt} = \bar{u}A_c$$

$$\frac{dV_{liq}}{dt} = -\frac{dV_{gas}}{dt}$$

$$\boldsymbol{\frac{dV_{gas}}{dt} = -\bar{u}A_c} \qquad \textbf{(B.1)}$$

The ideal gas law was then used to relate the volume to the pressure in the system. The derivative of the volume with respect to time could then be rewritten in terms of the derivative of pressure with respect to time resulting in Equation B.2.

$$\frac{mRT_o}{P^2}\frac{dP}{dt} = \bar{u}A_c \qquad \textbf{(B.2)}$$

A force balance was then done on the connecting tube that ignores inertial effects. The flow in the connecting tube was assumed to be laminar.

$$(P_{act} - P)A_c = \frac{64}{Re}\frac{L}{d}\frac{1}{2}\rho\bar{u}^2 \qquad \textbf{(B.3)}$$

Solving the force balance, Equation B.3, for the average velocity and substituting that velocity into Equation B.2 results in Equation B.4.

$$\frac{128mRT_0\mu L}{\pi^2 d^4 P^2}\frac{dP}{dt} + P = P_{act} \qquad \textbf{(B.4)}$$

Substituting in an average pressure allows Equation B.4 to be written in term of the gas volume and gives Equation B.5, which is the final form of the first order model. This model assumes linearity by using an average

$$\frac{128V_{gas}\mu L}{\pi^2 d^4 \bar{P}}\frac{dP}{dt} + P = P_{act} \qquad \textbf{(B.5)}$$

The derivation of the second order model uses the same process except the force balance includes the inertial effects of the fluid in the capillary tubes. This gives equation B.5.

$$(P_{act} - P)A_c - \frac{64}{Re}\frac{L}{d}\frac{1}{2}\rho\bar{u}^2 = \rho L A_c\frac{d\bar{u}}{dt} \qquad \textbf{(B.6)}$$

Equation B.2 is then solve for the average velocity and the derivative of the average velocity, Equations B.7 and B.8.

$$\bar{u} = \frac{mRT_o}{A_c P^2}\frac{dP}{dt} \qquad \textbf{(B.7)}$$

$$\frac{d\bar{u}}{dt} = \frac{mRT_0}{A_c}\left(\frac{1}{P^2}\frac{d^2P}{dt^2} - \frac{2}{P^3}\left(\frac{dP}{dt}\right)\right) \qquad \textbf{(B.8)}$$

Substituting the above Equations B.7 and B.8 into Equation B.6, and including the average pressure allows for the equation to be written in terms of the gas volume. The equation is then rearranged to be the second order model and is labelled Equation B.9.

$$P_{act} = \frac{4\rho L V_{gas}}{\pi d^2 \bar{P}} \frac{d^2P}{dt^2} - \frac{8\rho L V_{gas}}{\bar{P}^2}\left(\frac{dP}{dt}\right)^2 + \frac{512\mu L V_{gas}}{\pi^2 d^6 \bar{P}} \frac{dP}{dt} + P \qquad \textbf{(B.9)}$$

The first order model derived in this thesis, the second order model described by Fowler (1963) and the nonlinear first order model derived in this thesis were all compared in order to see which model best captured the behavior of the pressure transducer response. This is shown in Figures B.2 through B.9. The nonlinear response most accurate captured the initial pressure response but error in the time constant and mass estimate caused an increase in error near the steady state pressure. The first order model fit the data well in the converging section and the last two taps in the diverging section. These pressure transducers did not see as extreme of a pressure change and this is likely why the model fit these pressure responses best. The second order model did not fit the data well as the delay in the exponential response generate inaccuracies. An Euler method was used to generate the nonlinear model and so the effects of the time step were investigated. Three different time steps were investigated, 1.0 s, 0.1 s, and 0.01 s. Each time step generated the same response showing good stability of the model and that the model is unaffected by the time step.

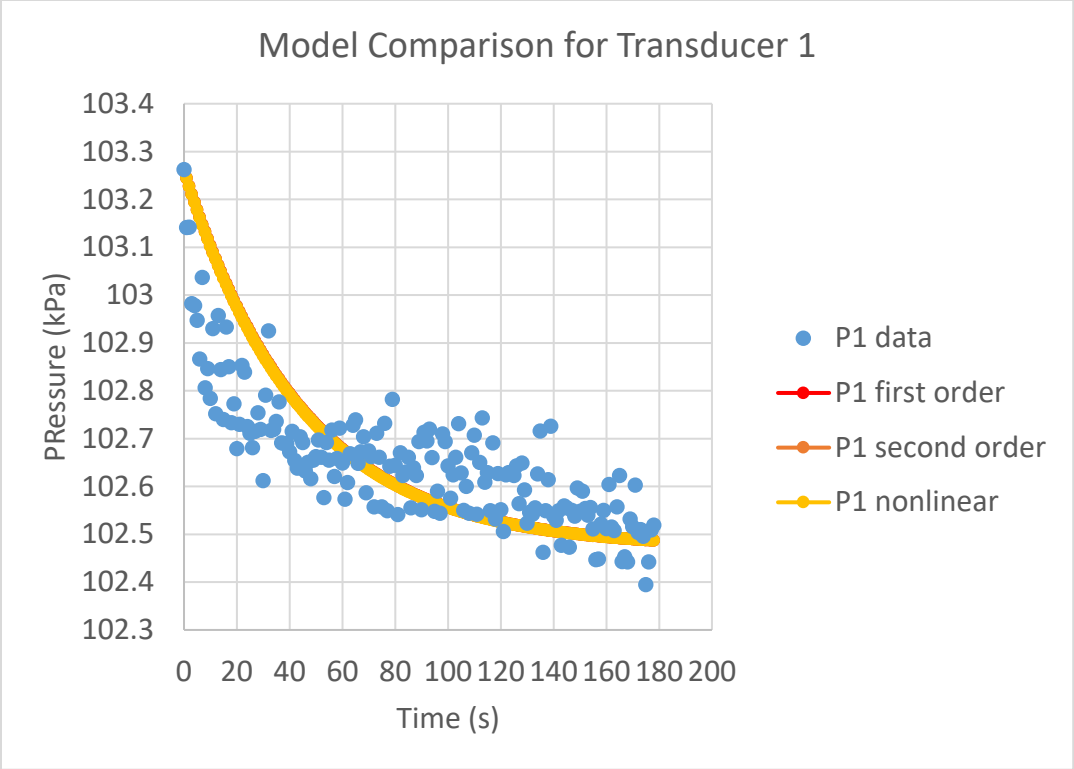

Figure B.3: Model Comparison for Pressure Transducer 1

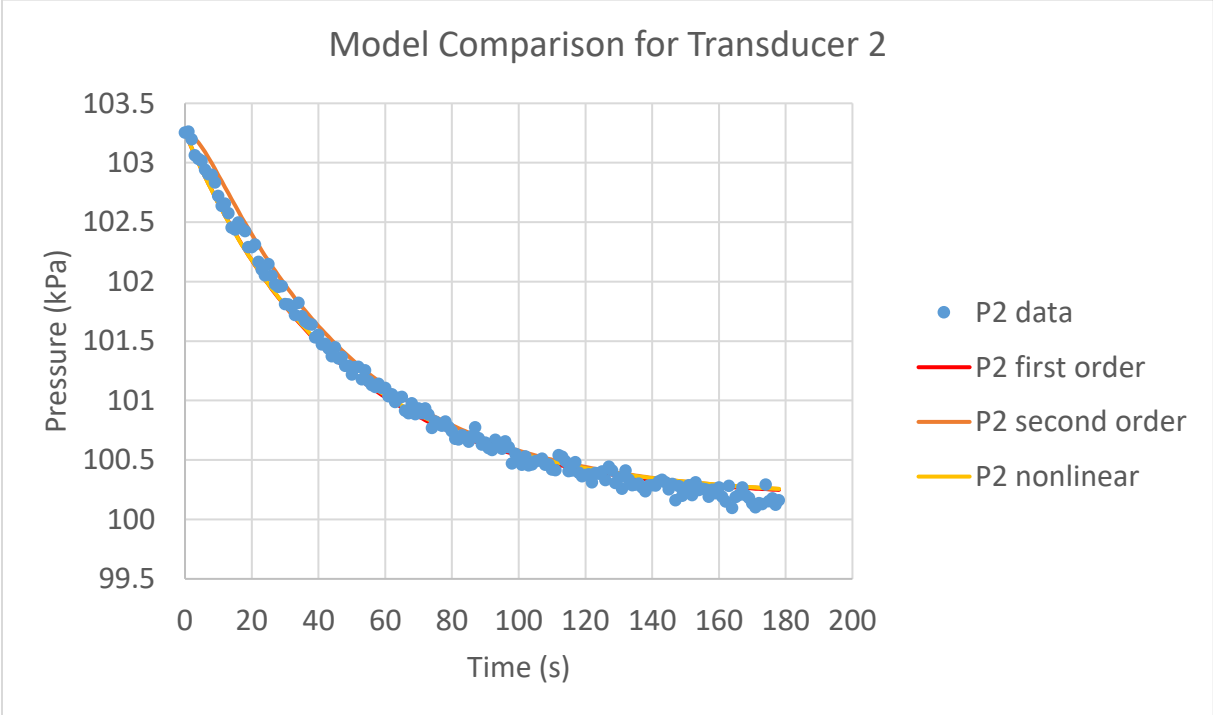

Figure B.4: Model Comparison for Pressure Transducer 2

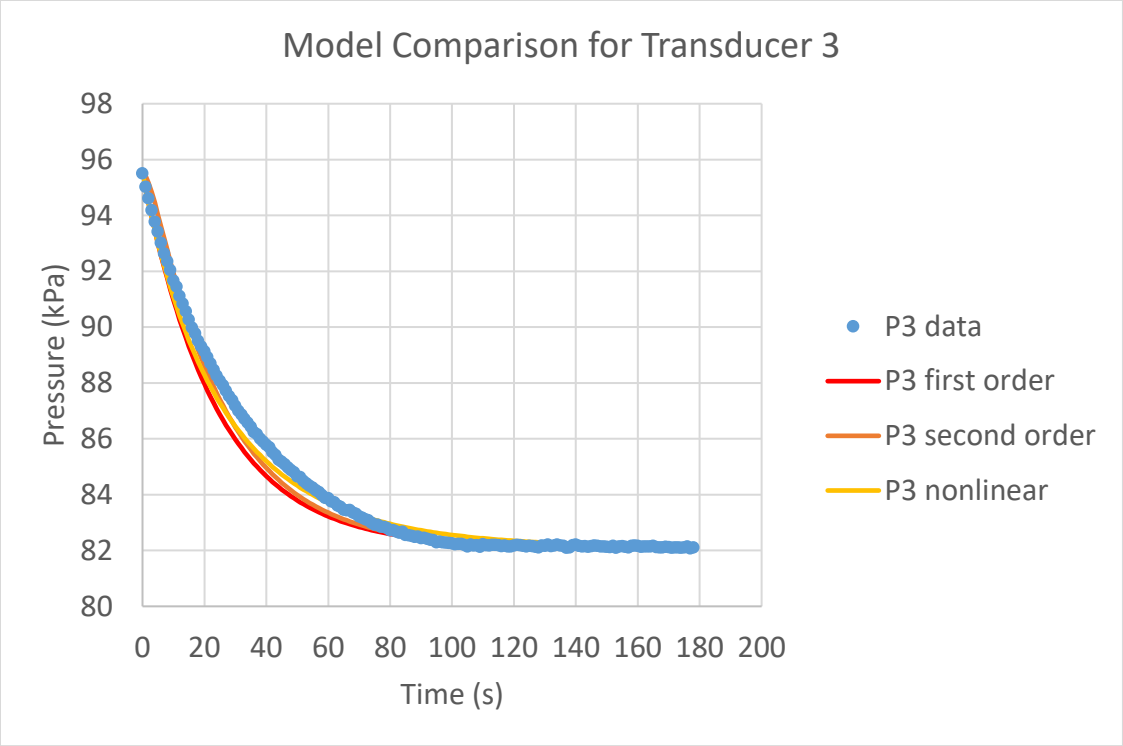

Figure B.5: Model Comparison for Pressure Transducer 3

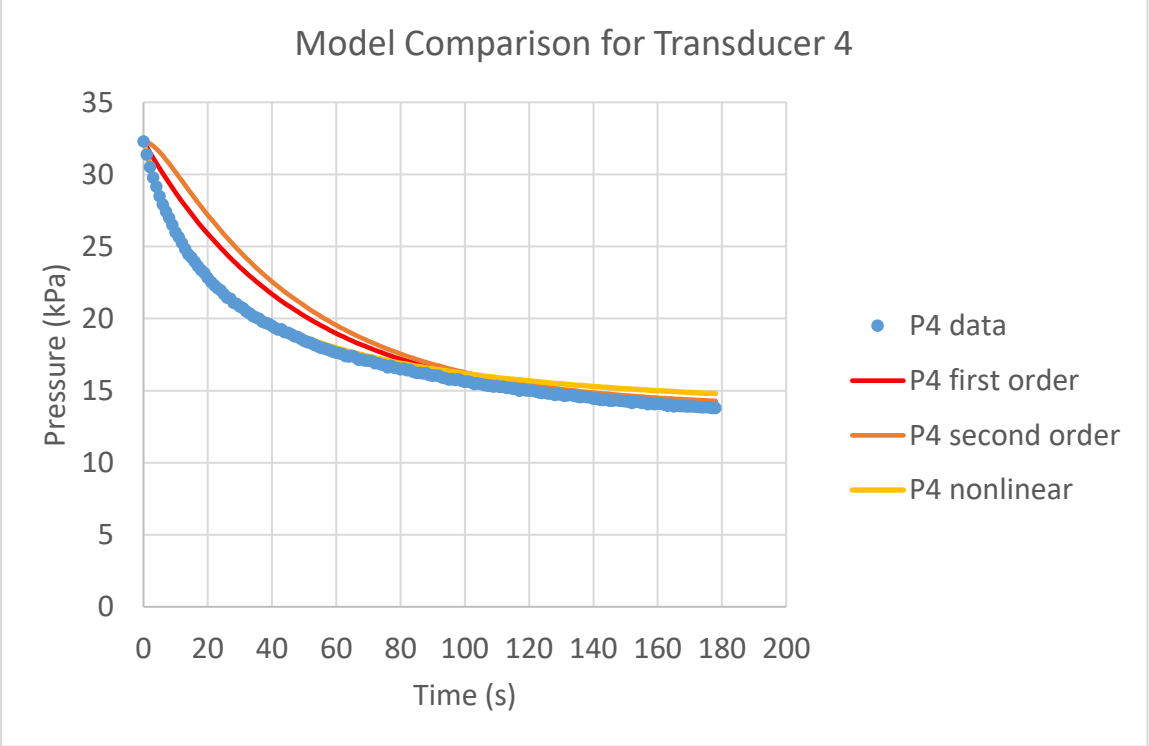

Figure B.6: Model Comparison for Pressure Transducer 4

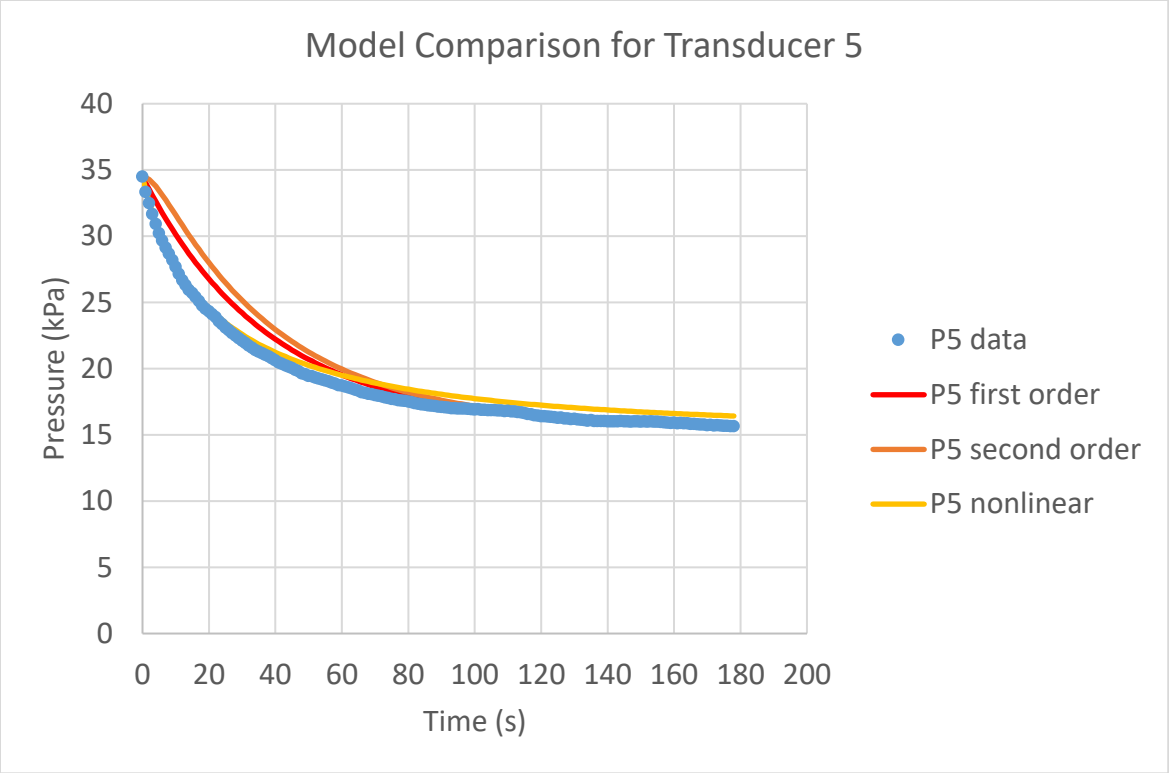

Figure B.7: Model Comparison for Pressure Transducer 5

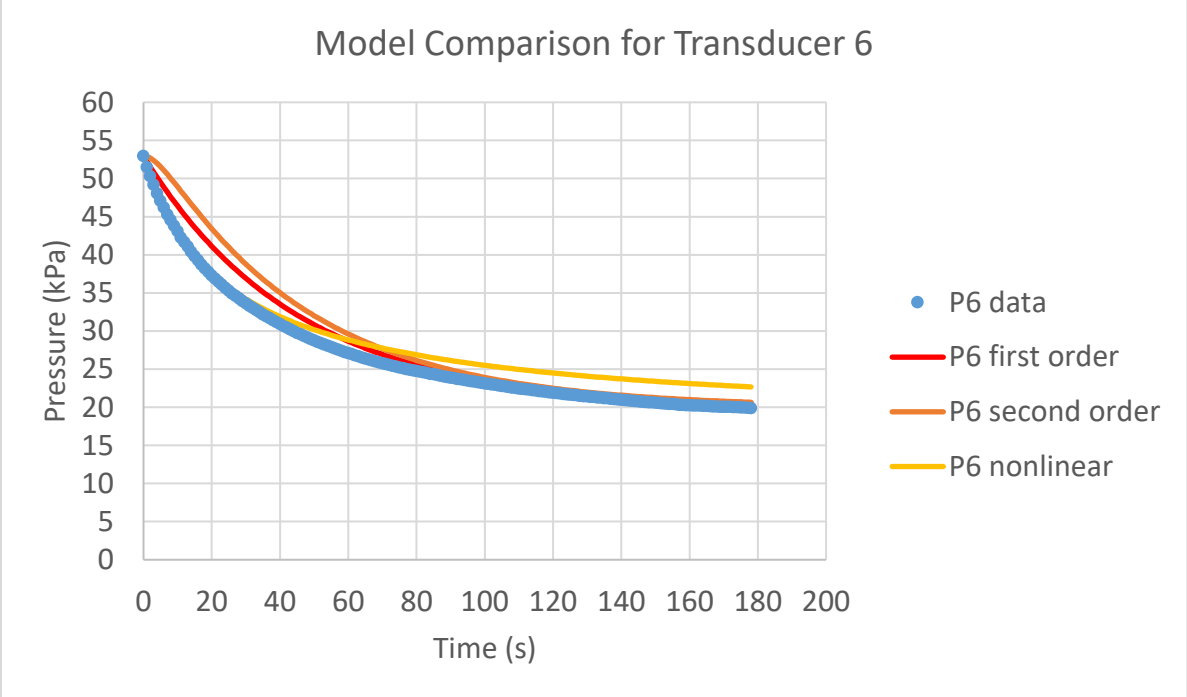

Figure B.8: Model Comparison for Pressure Transducer 6

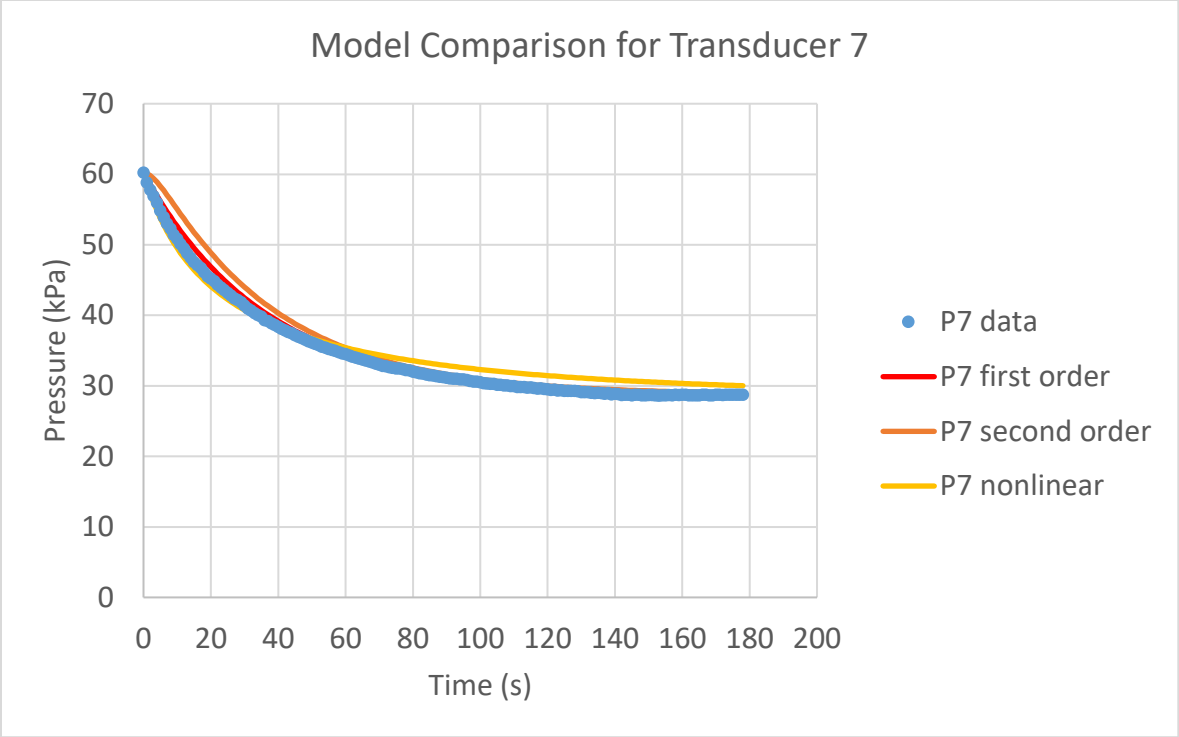

Figure B.9: Model Comparison for Pressure Transducer 7

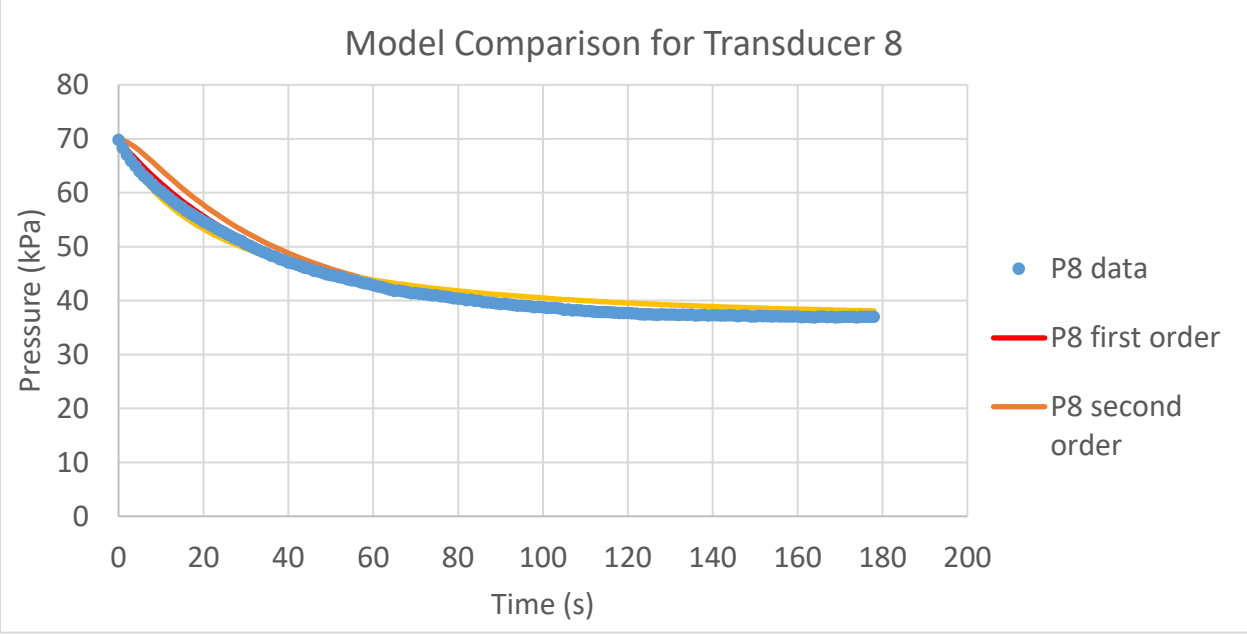

Figure B.10: Model Comparisons for Pressure Transducer 8

Because each derived model depended on the diameter of the connecting tube, larger tubing was connected to the pressure transducers to experimentally analyze the effects of diameter. The larger tubing had an inner diameter of 0.0625 inches, which is approximately ten times bigger than the 0.006-inch inner diameter tubing used in the majority of this thesis. The larger tubing resulted in a faster settling time in the pressure response for each transducer except for transducer 1. Pressure transducer 1 sees such a small change in pressure that it is difficult to accurately characterize the response. The response of each pressure transducer is plotted on a semi-log plot and fitted with a linear regression. A steeper regression results in a smaller time constant and thus a faster response. Figures B.10 through B.17 display the pressure transducer response for the big tubing and small tubing.

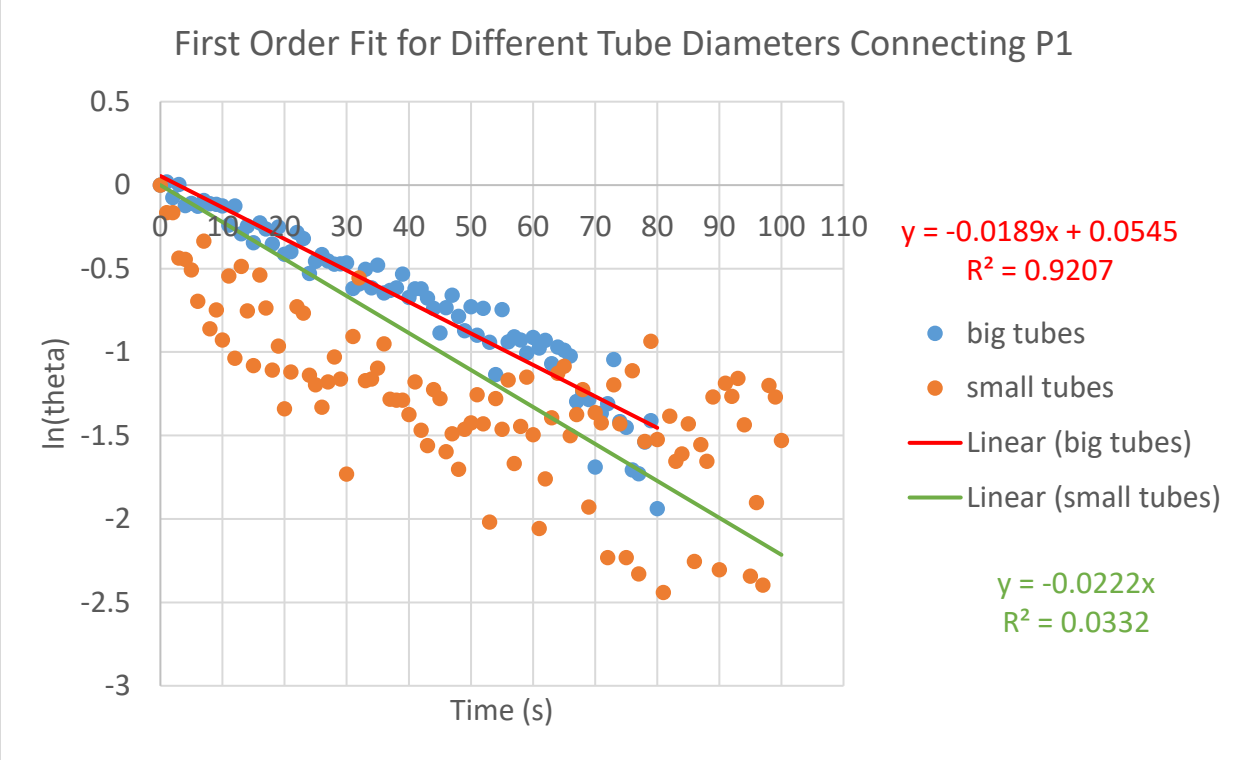

Figure B.11: Pressure response for different tube diameters for P1

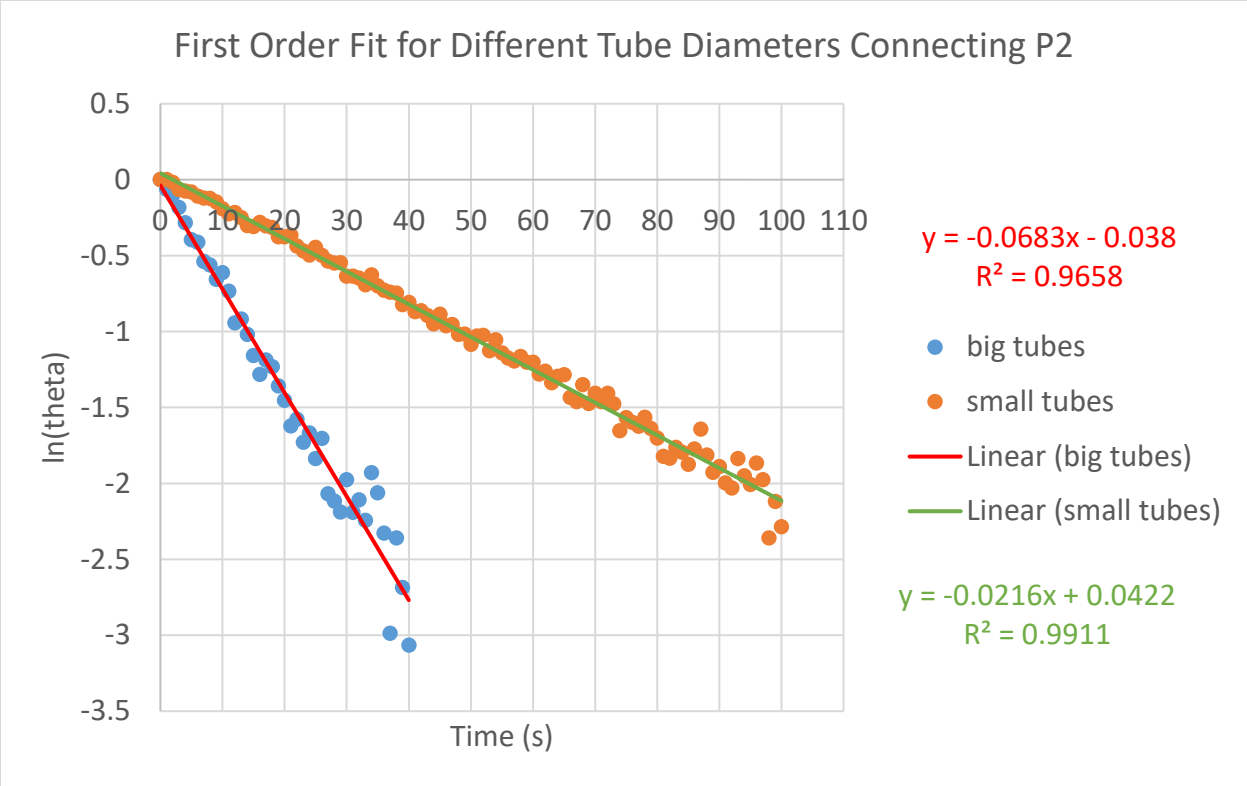

Figure B.12: Pressure response for different tube diameters for P2

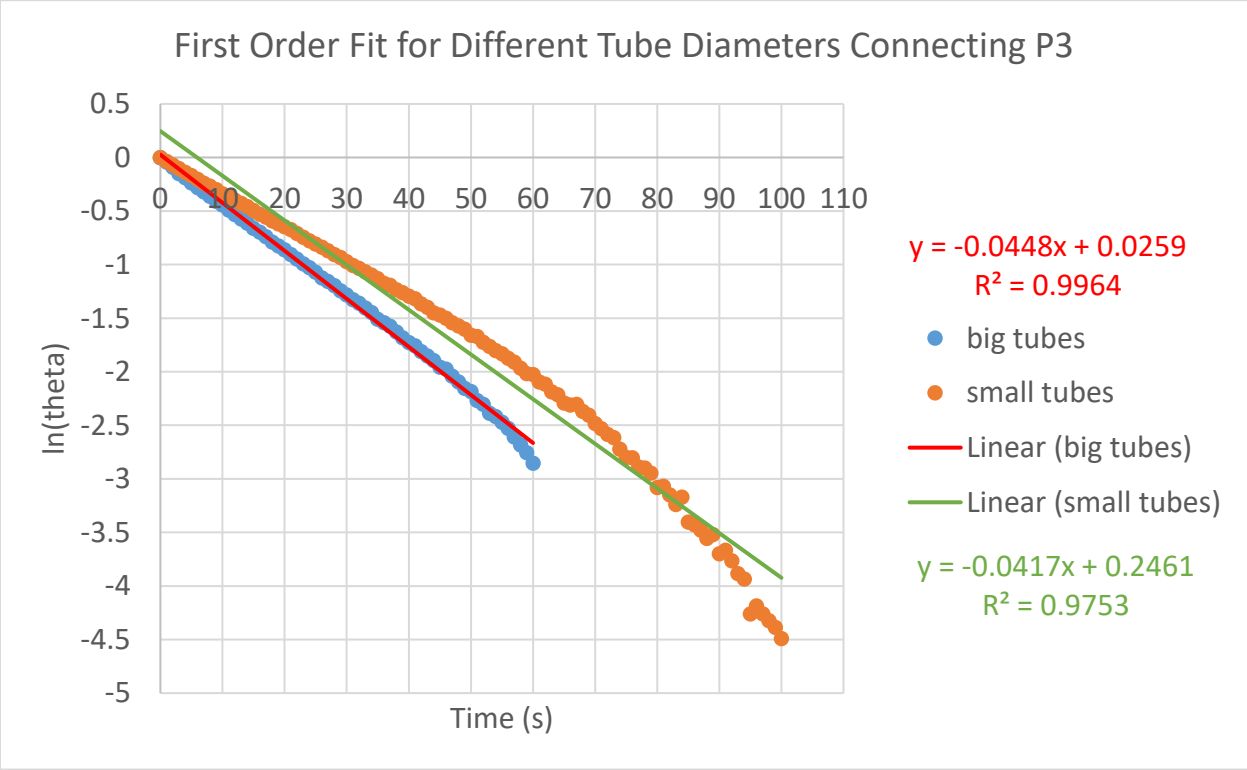

Figure B.13: Pressure response for different tube diameters for P3

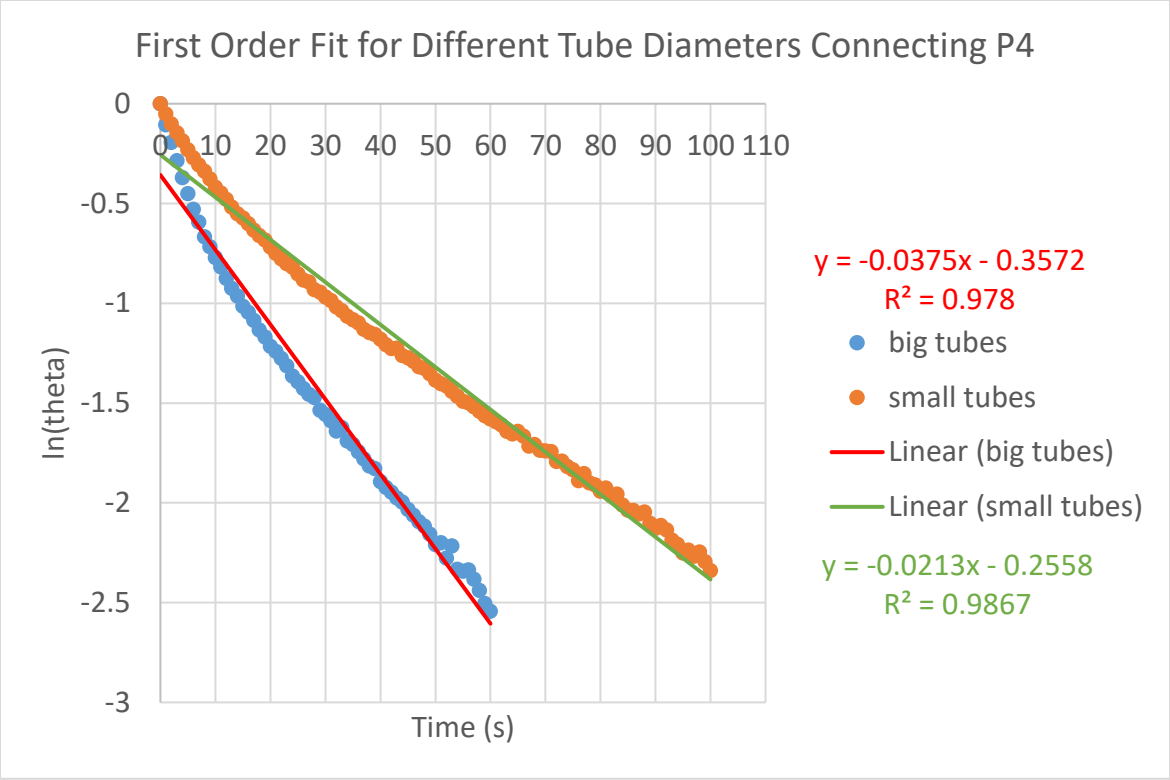

Figure B.14: Pressure response for different tube diameters for P4

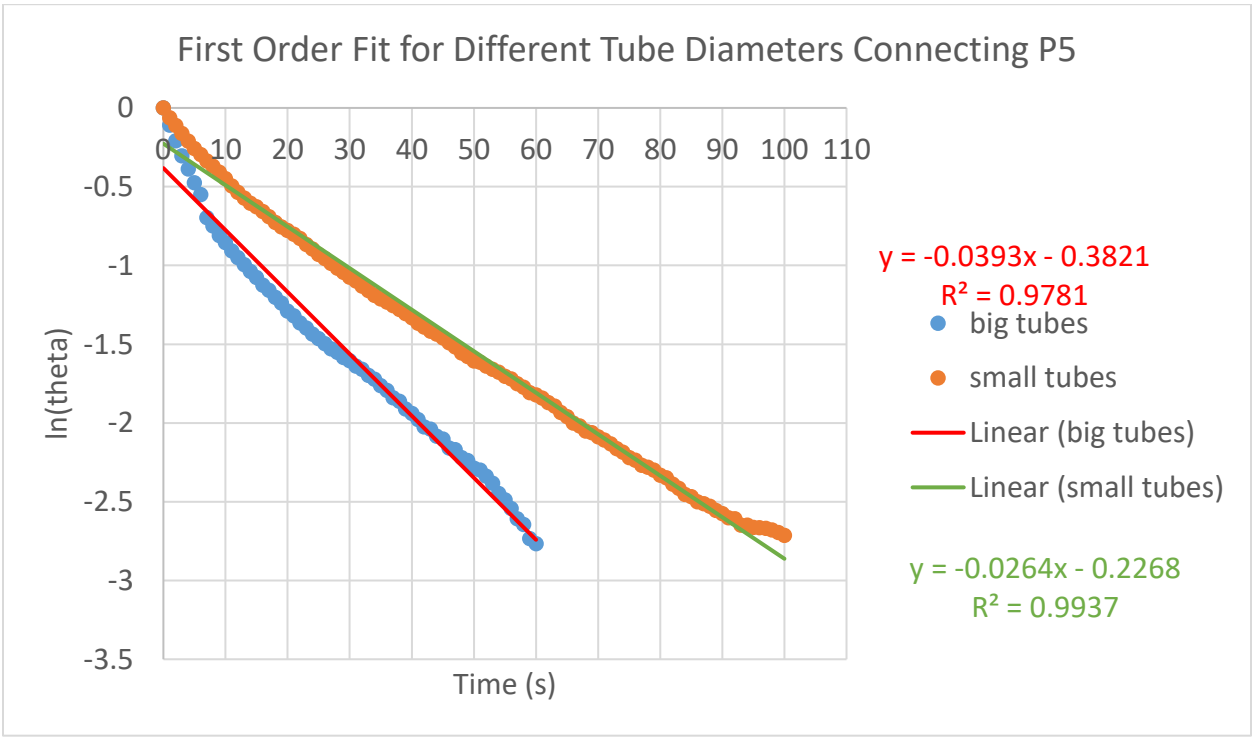

Figure B.15: Pressure response for different tube diameters for P5

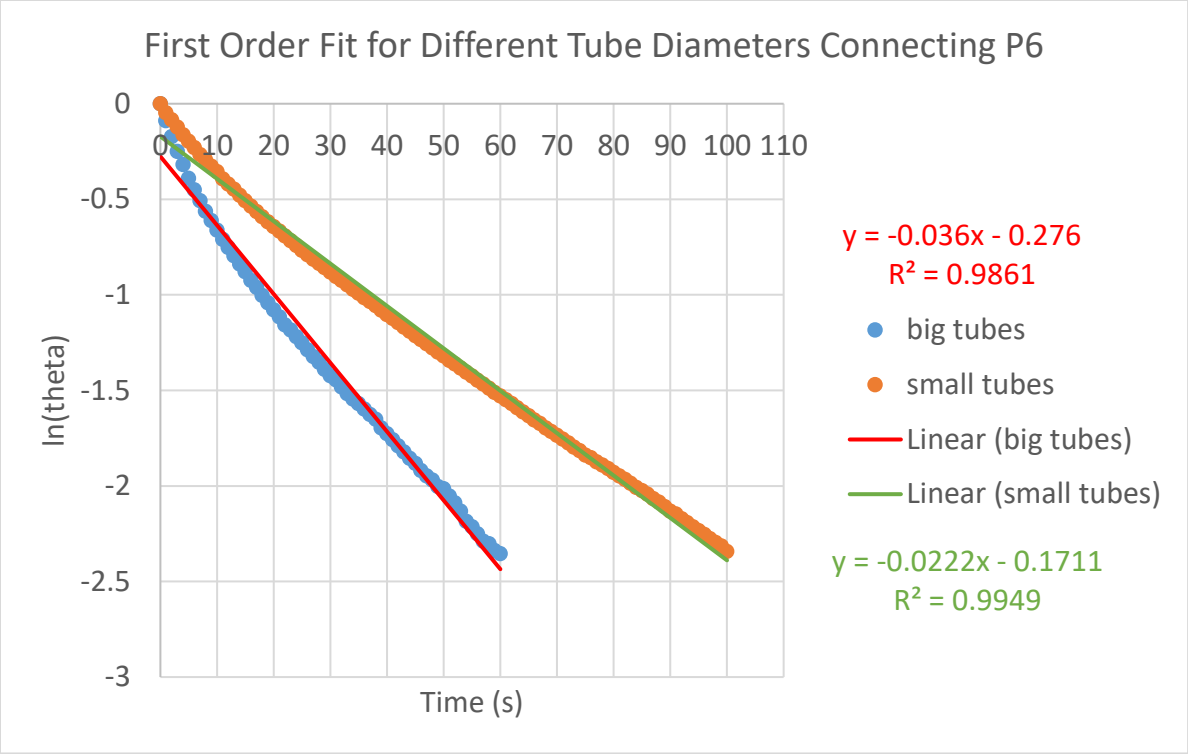

Figure B.16: Pressure response for different tube diameters for P6

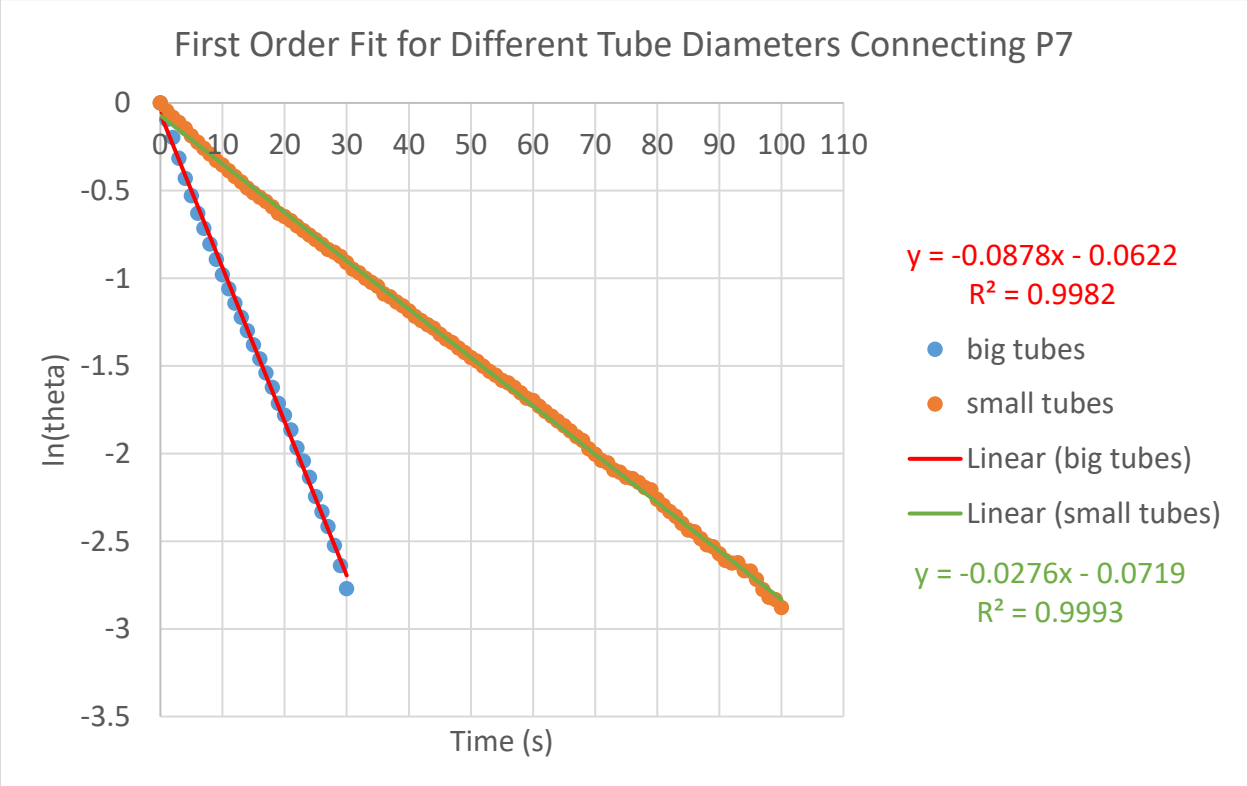

Figure B.17: Pressure response for different tube diameters for P7

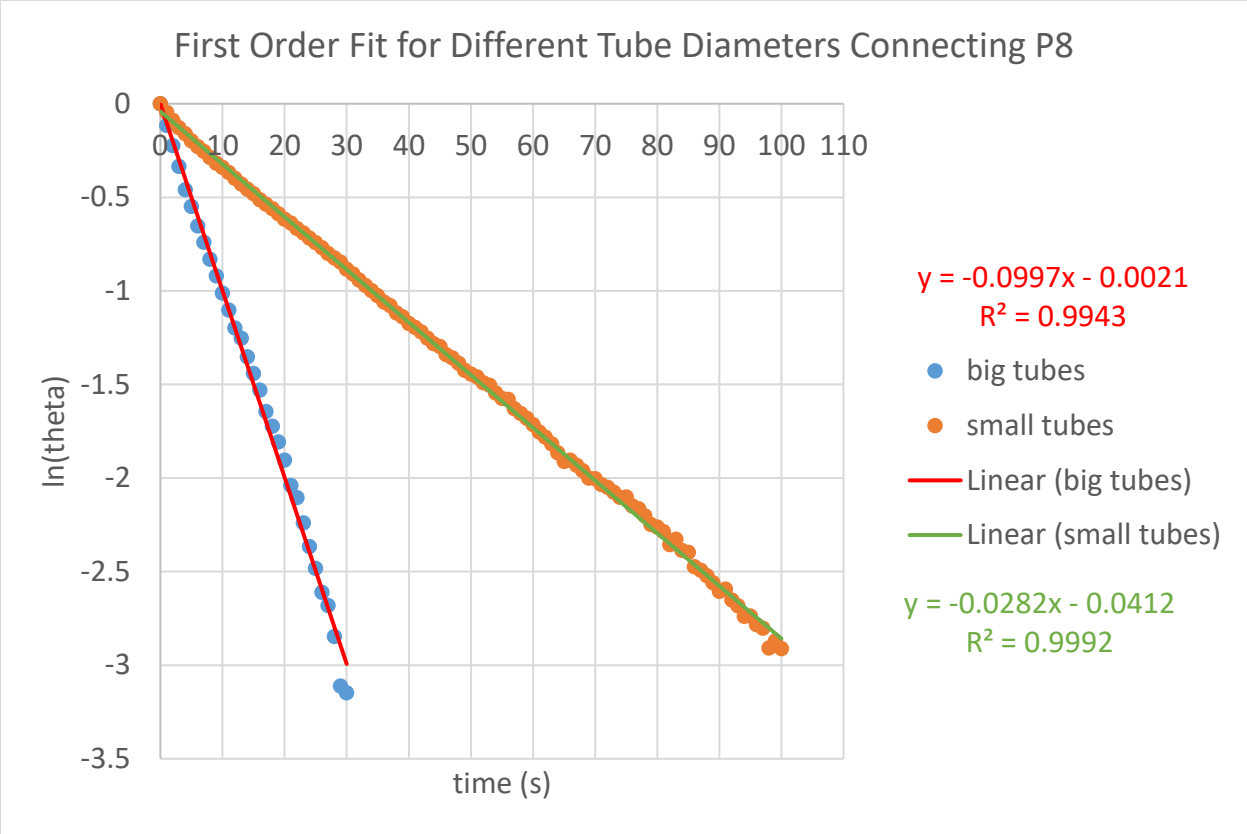

Figure B.18: Pressure response for different tube diameters for P8

Table B.1: Time constant comparison for different tube sizes

Pressure Transducer	Large Tube Time Constant	Small Tube Time Constant
P1	53	45
P2	15	46
P3	22	24
P4	27	47
P5	25	38
P6	28	45
P7	11	36
P8	10	35

Appendix C - Uncertainty Calculations

The uncertainty in the transient results was calculated by first finding the uncertainty in θ and ln(θ). The absolute uncertainty in θ was given the symbol u_θ and is a function of pressure transducer uncertainty, u_p. The pressure transducer uncertainties are given in Appendix A. Equations C.1 and C.2 give the functional forms of the uncertainty in θ and ln(θ), with the uncertainty in ln (θ) given as u_f.

$$\boldsymbol{u_\theta = \sqrt{\left(\frac{-1}{P_f - P_i}\right)^2 u_p^2 + \left(\frac{P - P_i}{(P_f - P_i)^2}\right)^2 u_p^2 + \left(\frac{P_f - P}{(P_f - P_i)^2}\right)^2 u_p^2}} \quad \textbf{(C.1)}$$

$$\boldsymbol{u_f = \frac{u_\theta}{\theta}} \quad \textbf{(C.2)}$$

The time constant τ was found from the linear regression of the ln(θ) plotted with respect to time. To find the uncertainty in τ the deviation of the ln(θ) data from the linear regression was calculated and then add to the uncertainty u_f. This gave the maximum and minimum bounds of the linear regression. From these bounds the maximum and minimum slope were calculated and the difference between τ and these slopes represented the uncertainty u_τ. This graphical approach to finding the uncertainty gives the most conservative estimate of the uncertainty in the time constant.

The overall uncertainty in the corrected pressure measurement was found using equation C.3. This equation includes the uncertainty in the pressure transducer output u_p, the slope of the pressure transducer output m_p or $\boldsymbol{\frac{dP}{dt}}$, the uncertainty in the time constant u_τ, and the time constant τ.

$$\boldsymbol{u_{act} = \sqrt{u_p^2 + m_p^2 u_\tau^2 + u_m^2 \tau^2}} \quad \textbf{(C.3)}$$

The uncertainty in the slope of the pressure transducer output was calculated in excel using the LINEST function over 5 points. This created a center scheme with which to find the uncertainty in slope. The LINEST function outputs a linear regression with the slope, standard deviation of the slope, y-intercept, and the standard deviation of the y-intercept. The standard deviation of the slope was then multiplied by two to fit within a 95% confidence interval. The slope was calculated from higher order curve fits and so finding the uncertainty in the manner described gives a conservative estimate of the uncertainty in the slope calculations.

Sample Uncertainty Calculations for Transducer P8

A sample of the calculations done using Equations C.1, C.2, and C.3. These calculations are for the uncertainty in transducer 8 in the fast-open transient test.

$$u_\theta = \sqrt{\left(\frac{-1}{\mathbf{36.96 - 69.78}}\right)^2 \mathbf{0.0558^2} + \left(\frac{69.78 - \mathbf{69.78}}{\mathbf{(36.96 - 69.78)^2}}\right)^2 \mathbf{0.0558^2} + \left(\frac{\mathbf{36.96} - 69.78}{\mathbf{(36.96 - 69.78)^2}}\right)^2 \mathbf{0.0558^2}} = \pm \mathbf{0.0024}$$

$$u_f = \frac{u_\theta}{\theta} = \frac{\pm 0.0024}{1} = \pm 0.0024$$

$$\boldsymbol{u_{act}} = \sqrt{\mathbf{0.0827^2} + (\mathbf{-5.11})^2 * 5.575^2 + \mathbf{0.55^2 5.58^2}} = \pm \mathbf{28.9\ kPa}$$

Appendix D - Pressure Measurement System Construction

The pressure measurement system was connected to the nozzle in a specific step by step manner to ensure the pressure tap bore holes and small capillary tubes were not clogged during construction. The construction procedure for each connection is as follows:

1. Ensure all bore holes are clear by submerging nozzle in water and blowing air through the nozzle with one end capped. Bubbles should emerge from the bore holes
2. Cut a length of tubing to the desired length
3. Use piano wire to ensure the tubing is not clogged by passing the wire through the tubing
4. With the wire in the tubing press one end of the tube into the outer bore hole of the nozzle
5. Use the digital microscope to check for any debris that could clog the smaller bore hole
6. If there is no debris apply epoxy to the joint of the tubing and the nozzle to carefully create a seal around the tube
7. Once the epoxy is dry remove the piano wire from the tubing
8. Repeat steps 1 through 7 until all pressure taps have tubing attached